# UNIVERSITÀ DEL SALENTO

## FACOLTÀ DI SCIENZE MM. FF. NN.

Dott. Giovanni Francesco Tassielli

PhD Thesis

# A gas tracking device based on
# Cluster Counting
# for future colliders

Tutori:
Dott. Francesco GRANCAGNOLO
Dott.sa Stefania SPAGNOLO

Coordinatore:
Chiar.mo Prof. Gilberto LEGGIERI

Dottorato di ricerca in Fisica XIX ciclo
settore scientifico FIS/04

# Contents

# Introduction

Hopefully, some open questions related to weaknesses of the Standard Model of elementary particles and to the physics of the TeV scale will find an answer when the first LHC data will be available. Most likely, some of them will not provide clear evidence of the whole framework of the underlying physics and, therefore, the construction of new colliders must be envisaged. Two projects are particularly promising: the "International Linear Collider" (*ILC*) and the "Super B factory" (*SuperB*). The physics programme of these new machines can be considered complementary to that of the LHC, and some overlap in time of LHC operation with such colliders is highly desirable, in order to increase the discovery potential of each single facility. The performance required by the experiments at future colliders are so challenging that a very intensive phase of detectors R&D is needed.

This thesis describes part of the R&D project for a central tracker system, specifically designed to operate at future colliders. The studies presented here concentrate on the feasibility of a Drift Chamber with extreme performace, such that it can operate both at the ILC and at the Super B. The Drift Chamber proposed is based on the successful KLOE central tracker, which has a full stereo geometry that guarantees an efficient three-dimensional track reconstruction. The Helium based gas mixture, the Aluminium wires and the carbon fiber walls guarantee high transparency, minimal multiple scattering

effect and the possibility to improve particle identification capability with the cluster counting technique. Here a specific proposal for such tracking device will be developed, starting from the basic parameters (mechanical and geometrical structure, gas, etc.) which determine the spatial resolution of a single measurement and concluding with an assessment of the physics potential of this detector in a full simulation of some benchmarks channels at ILC based on a supposed spatial resolution scenario. In the attempt to fully exploit the potentiality of a drift chamber as precision tracker, the benefit of the cluster counting technique in terms of spatial resolution will be investigated. This work will describe a detailed simulation of the response of a drift tube and some preliminary cluster counting measurements in a dedicated experimental setup. The dissertation will develop through five sections. The first one summarizes the Standard Model theory and the Spontaneous Electroweak Symmetry Breaking; an introduction to Supersymmetric theories is given along with to the problem of the CP violation. A brief description of possible physics results at LHC, ILC and SuperB is given. A short review of systems for tracking and particle identification and a discussion of the physics processes involved in charged particle detection will be given in section two in order to introduce the cluster counting technique. The third section contains Monte Carlo studies of the properties of an elementary drift cell. Moreover a model for the propagation of the signal along the drift tube is discussed, and algorithm to count electrons in the signal and one to reconstruct the impact parameter from cluster distribution information are proposed. Section four describes the simple experimental setup built in our laboratories. With it we can test the reproducibility of our MC and the efficiency of our cluster counting algorithm on real data. Furtermore the layout of the frontend electronic chip is reported. Finally section five presents a specific proposal for a

drift chamber in full details; the proposed construction parameters are fed to a Geant (v. 3) simulation of a detector for ILC which will be used to study the resolution on the SM Higgs achievable with the recoil mass method.

# Chapter 1

# Physics research at present and future colliders

## 1.1 The Standard Model and the current knowledge of particle physics

The nature of elementary particles and their interactions are well described by the Standard Model (SM) [1] as demonstrated by many experimental measurements in the last 30 years. The SM summarizes two disjoint theories: Quantum Cromo–Dynamics (QCD) that describes the strong interactions between quarks and gluons [2], and the Glashow–Salam–Weinberg electroweak theory [3, 4]. It is a renormalizable theory based on the gauge [5] symmetry group $G = SU(3)_C \otimes SU(2)_L^{weak} \otimes U(1)_Y^{weak}$, where $SU(3)_C$ is related to the color quantum number, $SU(2)_L^{weak}$ is generated by the weak isospin operators $\overrightarrow{T}$ and $U(1)_Y^{weak}$ is generated by the weak hypercharge operator $Y$.

The components of matter are fermions and can be divided into leptons and quarks (Fig. 1.1). For both categories, three different flavours (or families)
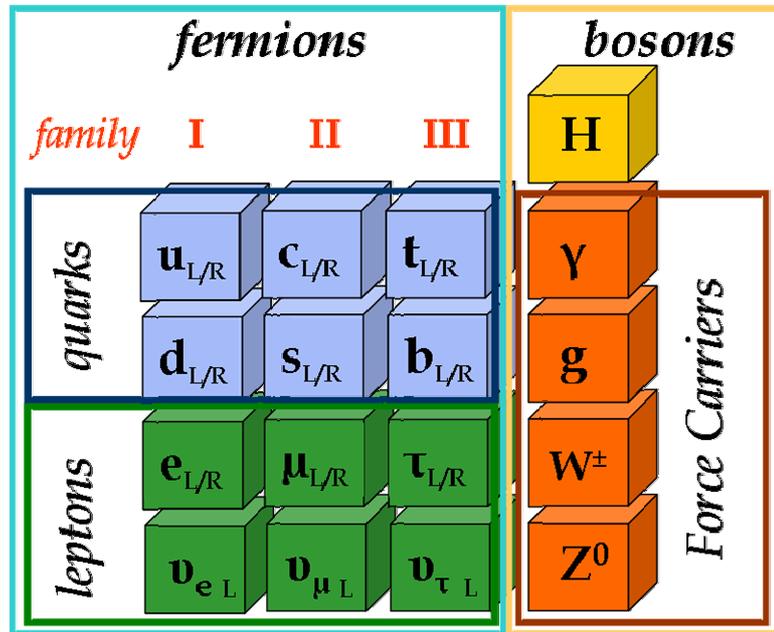
Figure 1.1: *Standard Model particles.*

exist. In each family there is a weak isospin doublet with *Left* helicity, two weak isospin singlet with *Right* helicity for the quarks and one weak isospin singlet with *Right* helicity for the leptons, in the assumption of massless neutrinos. Finally, quarks exist in three different colors (strong charge) for each flavour family. The mediators of the electroweak and strong forces are vector bosons: an interaction between two fermions can be described by the exchange of one of these bosons.

In particular, the gluons are eight massless vector bosons that couple to quarks of different color but same family according to the symmetry structure of $SU(3)_C$ (defined by the Gell–Mann matrices, generators of the group) with strength $g_s$, the strong coupling constant. The non-abelian gauge structure of $SU(3)_C$ implies that three and four point self–interactions among gluons are allowed and actually observed experimentally.

The electroweak theory is based on the gauge group $SU(2)_L \times U(1)_Y$. Here the four physical vector bosons, $\gamma, Z^0, W^\pm$, correspond to linear combinations of the fields ($W^i$ and $B$) associated with the gauge generators, the Pauli matrices for $SU(2)_L$ and the identity for $U(1)_Y$. The strength of the coupling of each fermion doublet or singlet to the bosons depends on $g$, the gauge coupling, constant and $\theta_W$ the weak angle, in addition to the gauge quantum number, isospin and hypercharge[1].

The Higgs particle is a scalar boson necessary in the theory in order to introduce mass terms for the other particles without spoiling the invariance and renormalizability of the theory. A more detailed explanation for the Higgs mechanism is given in the next paragraph.

### 1.1.1 Electroweak symmetry breaking and Higgs field

Gauge invariance and renormalization do not allow mass terms in the Lagrangian for the gauge bosons or for chiral fermions. On the other hand, massless gauge bosons are not acceptable for the weak interactions which are known to be short–ranged. The higgs mechanism consists in introducing a pair of complex scalar fields $\varphi = \begin{pmatrix} \varphi^+ \\ \varphi^0 \end{pmatrix}$ with hypercharge $Y_\varphi = +\frac{1}{2}$ which transform as a doublet under $SU(2)_L$. The corresponding term in the SM Lagrangian is:

$$\mathcal{L}_\varphi = (D^\mu \varphi)^\dagger D_\mu \varphi - V(\varphi) \tag{1.1}$$

where $D_\mu$ is the covariant derivative for $SU(2)$ doublets:

$$D_\mu = \left( \partial_\mu + ig\frac{\tau_i}{2}W^i_\mu + ig'\frac{Y}{2}B_\mu \right). \tag{1.2}$$

---

[1]The third component of weak isospin ($T_3$) and hypercharge ($Y$) are related to the electric charge operator by the relation $Q = T_3 + \frac{Y}{2}$

Invariance under $SU(2)_L \times U(1)_Y$ and renormalizability restricts the potential $V$ to the form

$$V(\varphi) = \mu^2 \varphi^\dagger \varphi + \lambda \left(\varphi^\dagger \varphi\right)^2 \tag{1.3}$$

In particular, the vacuum stability requires $\lambda > 0$, while a $\mu^2 < 0$ is needed for spontaneous symmetry breaking. In this scenario, effective masses, for bosons and matter particles, are generated under the assumption that the vacuum (i.e. the lowest energy state) does not respect the Lagrangian symmetry. If we rewrite the Higgs doublet in terms of four real fields:

$$\varphi = \begin{pmatrix} \varphi^+ \\ \varphi^0 \end{pmatrix} = \begin{pmatrix} \frac{1}{\sqrt{2}}(\varphi_1 - i\varphi_2) \\ \frac{1}{\sqrt{2}}(\varphi_3 - i\varphi_4) \end{pmatrix}$$

the potential (1.3) becomes:

$$V(\varphi) = \frac{1}{2}\mu^2 \sum_{i=1}^4 \varphi_i{}^2 + \frac{1}{4}\lambda \left(\sum_{i=1}^4 \varphi_i{}^2\right)^2 \tag{1.4}$$

which has its minimum at $|\varphi| = \sqrt{-\frac{\mu^2}{2\lambda}}$.

This manifold of points that are minimizing $V(\varphi)$ are invariant under $SU(2)$ transformations. Any choice of a particular value of $\varphi$ ($\varphi_0$) breaks the symmetry and generates a mass term in the Lagrangian for the corresponding gauge boson. However, if the vacuum $\varphi_0$ is still left invariant by some subgroup of gauge transformations, then the gauge boson associated with this subgroup will remain massless.

The appropriate choice to generate the observed boson masses ($\sim 100 \text{ GeV/c}^2$ for $Z^0, W^\pm$ and 0 for the photon) is:

$$< 0|\varphi_i|0 >= 0 \quad \text{for } i = 1, 2, 4 \quad \text{and} \quad < 0|\varphi_3|0 >= v$$

this vacuum value is not invariant under $T_1$, $T_2$ and $T_3 - \frac{Y}{2}$, but it is invariant under $T_3 + \frac{Y}{2} = Q$ (the electric charge). As a consequence, by expanding the

fourth field around this vacuum value, i.e. replaiing $\varphi$ by $\varphi = \begin{pmatrix} \varphi^+ \\ \varphi^0 \end{pmatrix} = \frac{1}{\sqrt{2}} \begin{pmatrix} 0 \\ v + h(x) \end{pmatrix}$ the Eq. (1.1) gives masses ($M_W$ and $M_Z$) for the $W^\pm$ and the $Z$ fields defined as follows:

$$W^\pm = \frac{1}{\sqrt{2}} \left( W^1 \mp iW^2 \right)$$

$$Z = -\sin\theta_W B + \cos\theta_W W^3$$

$$M_W = \frac{vg}{2} \quad , \quad M_Z = \sqrt{g^2 + g'^2}\frac{v}{2}$$

while the photon field:

$$A \;=\; \cos\theta_W B + \sin\theta_W W^3$$

remains massless.

Analogously, the same mechanism applied to a Lagrangian term describing Yukawa couplings of the Higgs field doublet to the fermion fields gives masses to the leptons and quarks. As a consequence of such a mechanism a single neutral scalar field $h$ survives in the Lagrangian with mass unpredicted and with couplings to fermions and vector bosons proportional to their masses.

## 1.1.2   Minimal Supersymmetric S.M. extension

In spite of the excellent agreement of the SM with many precision strong and electroweak measurements and although it is a mathematically consistent renormalizable field theory, there are some questions that haven't found a satisfactory answer. Therefore the SM is not believed to be an exhaustive theory of elementary particles but, rather, an effective low energy approximation of some more general theory. The main shortcomings of the SM are:

- in the *fermion* sector there is no explanation of the existence of several fermion families. Furthermore, there is no explanation or prediction of the fermion masses, which vary over at least five orders of magnitude, or of the CKM mixing (Sec. 1.1.3);

- the *gauge* symmetry is a direct product of three subgroups with separate gauge couplings: there is no explanation for why only the electroweak part is chiral (parity violating) and no reason for the fact that all particles have charges which are multiples of $e/3$;

- 'ad-hoc' Higgs fields are introduced, by hand, to generate masses for the $W$, $Z$ and fermions; moreover to have a consistent theory the Higgs mass should not be too different from the $W$ mass. If $M_H$ is larger than $M_W$ by many orders of magnitude there would be a hierarchy problem, and the Higgs self–interactions would be excessively strong.

Possible answers for these problems are usually found in the alternative theories like SUperSYmmetric Models, Grand Unified Theory, Extra–Dimensions and String Theories, which embed the SM as a low–energy limit. A brief description of the SUperSYmmetry theory and the Minimal Super-Symmetric Standard Model extension will be given here, since most likely, LHC and future collider experiments might confirm or invalidate such a theory for most of its possible realizations [2].
The SUSY theory is based on a group of global transformations relating half-integer and integer spin particles, in particular each particle has a copy having the same quantum numbers but spin different by $\hbar/2$. In this theory

---

[2]The phenomenology of the MSSM depends on the value of a few unpredicted parameters. Most of the free parameter space, however, imply observable SUSY effects at LHC.

| Particles | | SUSY partner | | |
|---|---|---|---|---|
| Particle | Spin | Particle | Spin | |
| quark $(q)$ | $\frac{1}{2}$ | squark $(\tilde{q})$ | 0 | |
| lepton $(l)$ | $\frac{1}{2}$ | slepton $(\tilde{l})$ | 0 | |
| gluon $(G)$ | 1 | gluino $(\tilde{G})$ | $\frac{1}{2}$ | |
| $W^{\pm}$, $Z^0$, $\gamma$ | 1 | chargino $(\tilde{\chi}_i^{\pm}$   $i=1,2)$ | $\frac{1}{2}$ | |
| Higgs boson $(h,\ H,\ A,\ H^{\pm})$ | 0 | neutralino $(\tilde{\chi}_i^0$   $i=1,2,3,4)$ | $\frac{1}{2}$ | |

Table 1.1: *MSSM Particles.*

the hierarchy problem is simply solved because an equal number of bosons and fermions contribute with equal but opposite sign terms in radiative corrections to the Higgs mass, thus cancelling any quadratic divergence. A new multiplicative quantum number, $R$-parity, is introduced in the theory:

$$R = (-1)^{3B+L+2S}$$

where $B$ and $L$ are the baryon and lepton numbers and $S$ is the spin of the particle.

The MSSM is obtained by extending the Higgs sector and introducing a supersymmetric partner for each SM particle, called sparticle, with a spin different by $\hbar/2$ and by enforcing $R$-parity conservation, Tab. 1.1. For quarks and leptons, complex scalar fields, squarks $(\tilde{q})$ and sleptons $(\tilde{l})$, are introduced, superpartners of the gauge bosons are spin –1/2 gauge fermions generically indicated with the term "gauginos". In more detail, they are gluinos $(\tilde{g})$ associated to the SM gluons, wino and a bino $(\tilde{W}^{\pm},\ \tilde{B})$ corresponding to the electroweak gauge fields. As for the Higgs sector, the SUSY models contain at least two Higgs doublet fields. They are required separately to generate the mass terms for up–type quarks, and for down–type quarks and charged leptons. The new Higgs doublets lead to additional massive scalar bosons.

After electroweak symmetry breaking three of the eight degree of freedom
introduced by the two Higgs doublets are removed and five physical ones
remain: two neutral scalar boson H, $h$, a neutral pseudo scalar boson A and
two charged scalar bosons H$^{\pm}$. The supersymmetric partners of these five
bosons (Higgsinos), mix with the winos and binos to form a charged and
neutral set of mass eigenstates. The two charginos ($\tilde{\chi}_i^{\pm}$   $i = 1, 2$) result
from charged Higgsinos and charged wino mixing, and the four uncharged
neutralinos ($\tilde{\chi}_i^0$   $i = 1, 2, 3, 4$) result from the two neutral Higgsino, neutral
wino and bino mixing.

It is important to bear in mind that in the MSSM Lagrangian there are 105
new parameters with respect to the SM that are related to masses, phases
and mixing angles. Most of these new parameters involve flavor mixing or
CP violating processes that are forbidden in the SM.

It is interesting to note that this large number of new free parameters is
reduced only to five in the minimal supergravity model (mSUGRA).

### 1.1.3   Flavour physics and CP violation

In the SM the couplings of the quarks to the Higgs field are not diagonal for
any weak basis, in order to diagonalize the Yukawa couplings, the so-called
Cabbibo-Kobayashi-Maskawa unitary matrix $\hat{V}_{CKM}$ is introduced [6, 7]. The
CKM matrix connects the electroweak eigenstates ($d', s', b'$) of the down-type
quarks with their mass eigenstates ($d, s, b$) through the following unitary
transformation:

$$\begin{pmatrix} d' \\ s' \\ b' \end{pmatrix} = \hat{V}_{CKM} \begin{pmatrix} d \\ s \\ b \end{pmatrix}, \ \hat{V}_{CKM} = \begin{pmatrix} V_{ud} & V_{us} & V_{ub} \\ V_{cd} & V_{cs} & V_{cb} \\ V_{td} & V_{ts} & V_{tb} \end{pmatrix} \tag{1.5}$$
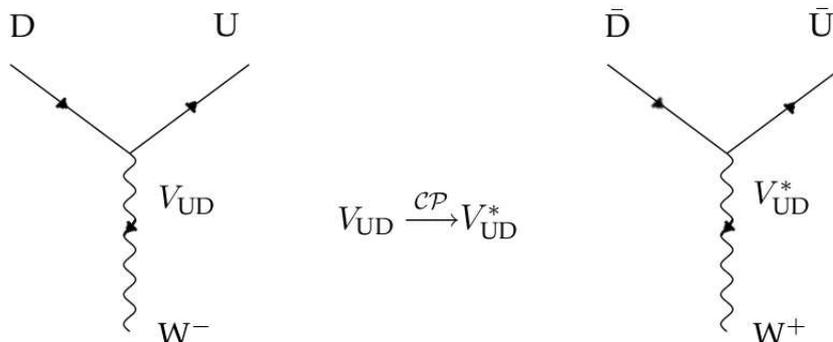
Figure 1.2: *Charged Current quarks interaction and its CP-conjugated.*

In this new basis the charged current (CC) interactions mediated by the $W^\pm$ bosons, see Fig. 1.2 (D$\rightarrow$U $W^-$ where U $\in \{u, c, t\}$, D $\in \{d, s, b\}$), are still purely left-handed and the Lagrangian for them is:

$$\mathcal{L}_{int}^{CC} = -\frac{g}{\sqrt{2}} \left( \begin{array}{ccc} \overline{u}_L & \overline{c}_L & \overline{t}_L \end{array} \right) \gamma^\mu \hat{V}_{CKM} \left( \begin{array}{c} d_L \\ s_L \\ b_L \end{array} \right) W_\mu^\dagger + h.c.$$

where the $\gamma^\mu$ are the Dirac matrices and the $W_\mu^\dagger$ field corresponds to the charged W bosons. It is important to note that the *unitarity* of $\hat{V}_{CKM}$ ensures the absence of flavor neutral changing current (FCNC) at the tree level order of approximation. It can be shown that the number of independent parameters for a $N \times N$ unitary matrix is given by:

$$N^2 - (2N - 1) = \underbrace{\frac{1}{2}N(N-1)}_{Euler\ angles} + \underbrace{\frac{1}{2}(N-1)(N-2)}_{complex\ phases} = (N-1)^2$$

as a consequence of the freedom of redefining the phases of the quark mass eigenstates. Therefore, in the case of the SM, where $N$=3, there are three Euler angles and one complex phase in the CKM matrix. The last term allows

a difference in the branching ratio for Charged Current quark interactions and for the process obtained by Charge and Parity conjugation, Fig. 1.2. This is the mechanism proposed by Kobayashu and Maskawa [7] to explain, under the SM framework, the observed CP violation in the decays of neutral kaons. However, in same conditions (quark mass degeneracy, for examples) an appropriate transformation allows to redefine $V_{CKM}$ in such a way to remove the complex phase. The following conditions:

$$(m_t^2 - m_c^2)(m_t^2 - m_u^2)(m_c^2 - m_u^2)(m_b^2 - m_s^2)(m_b^2 - m_d^2)(m_s^2 - m_d^2) \times J_{CP} \neq 0,$$
$$J_{CP} =\mid Im(V_{i\alpha}V_{j\beta}V_{i\beta}^*V_{j\alpha}^*) \mid \quad (i \neq j, \ \alpha \neq \beta).$$

are necessary to ensure that the complex phase is physically meaningful. Hence, the Jarlskog parameter, $J_{CP}$, can be interpreted as a measure of the strength of the CP violation in the SM.

The CKM matrix has several parameterizations like:

- the '*standard*' one:

$$\hat{V}_{CKM} = \begin{pmatrix} c_{12}c_{13} & s_{12}c_{13} & s_{13}e^{-i\delta_{13}} \\ -s_{12}c_{23} - c_{12}s_{23}s_{13}e^{i\delta_{13}} & c_{12}c_{23} - s_{12}s_{23}s_{13}e^{i\delta_{13}} & s_{23}c_{13} \\ s_{12}s_{23} - c_{12}c_{23}s_{13}e^{i\delta_{13}} & -c_{12}s_{23} - s_{12}c_{23}s_{13}e^{i\delta_{13}} & c_{23}c_{13} \end{pmatrix}$$

    where $c_{ij} = \cos\theta_{ij}$ and $s_{ij} = \sin\theta_{ij}$, in this parameterization the generation labels $i, j$ =1,2,3 are introduced in such a manner that the mixing between two chosen generations vanishes if the corresponding mixing angle $\theta_{ij}$ is set to zero and so the $\hat{V}_{CKM}$ can be reduced to the Cabibbo matrix for two quarks families mixing;

- the Wolfenstein parameterization makes explicit the hierarchy pattern, with the diagonal elements being close to 1; in a recent accurate ex-

pansion, it is given by the following expression [8]:

$$\hat{V}_{CKM} = \begin{pmatrix} 1 - \frac{1}{2}\lambda^2 - \frac{1}{8}\lambda^4 & \lambda + \mathcal{O}(\lambda^7) & A\lambda^3(\rho - i\eta) \\ -\lambda + \frac{1}{2}A^2\lambda^5[1 - 2(\rho + i\eta)] & 1 - \frac{1}{2}\lambda^2 - \frac{1}{8}\lambda^4(1 + 4A^2) & A\lambda^2 + \mathcal{O}(\lambda^8) \\ A\lambda^3(1 - \bar{\rho} - i\bar{\eta}) & -A\lambda^2 + \frac{1}{2}A\lambda^4[1 - 2(\rho + i\eta)] & 1 - \frac{1}{2}A^2\lambda^4 \end{pmatrix}$$

where

$$\overline{\rho} \equiv \rho \left(1 - \frac{\lambda^2}{2}\right) \ , \quad \overline{\eta} \equiv \eta \left(1 - \frac{\lambda^2}{2}\right)$$

$\lambda \equiv s_{12}$ (the sine of Cabibbo angle), $A\lambda^2 \equiv s_{23}$ and $A\lambda^3(\rho - i\eta) \equiv s_{13}e^{-i\delta_{13}}$ ($\rho \approx 0.1, \eta \approx 0.4, A \approx 0.8$). This parameterization is widely used in the study of the CP violation in the $B$ and $K$ mesons systems.

The Wolfenstein parameterization allows to easily see that the CP violation is a small effect in the SM since the Jarlskog parameter can be written $J_{CP} \simeq \lambda^6 A^2 \eta \backsim 10^{-5}$.

The unitarity of the CKM matrix has another consequence that six of this kind equation must be satisfied:

$$V_{ud}V_{ub}^* + V_{cd}V_{ub}^* + V_{td}V_{tb}^* = 0. \tag{1.6}$$

This equation can be geometrically represented, in the complex plane, as a unitarity triangle, Fig. 1.3, with angles given by:

$$\alpha \equiv \varphi_2 \equiv arg\left(-\frac{V_{td}V_{tb}^*}{V_{ud}V_{ub}^*}\right)$$
$$\beta \equiv \varphi_1 \equiv arg\left(-\frac{V_{cd}V_{cb}^*}{V_{td}V_{tb}^*}\right)$$
$$\gamma \equiv \varphi_3 \equiv arg\left(-\frac{V_{ud}V_{ub}^*}{V_{cd}V_{cb}^*}\right)$$

and with area equal to $J_{CP}/2$.

The parameters of the unitarity triangle (UT) can be measured using observables of the $B$ and $K$ systems. In particular:

- semi-leptonic $b \to ul\overline{\nu}_l$, $cl\overline{\nu}_l$ decays and $B_q^0 - \overline{B}_q^0$ ($q = d, s$) mixing [9] allow to determine $\sqrt{\overline{\rho}^2 + \overline{\eta}^2} = \left|\frac{V_{ud}V_{ub}^*}{V_{cd}V_{cb}^*}\right|$ and $\sqrt{(1 - \overline{\rho})^2 + \overline{\eta}^2} = \left|\frac{V_{td}V_{tb}^*}{V_{cd}V_{cb}^*}\right|$, thus defining two circles in the $\overline{\rho} - \overline{\eta}$ plane, Fig. 1.4;
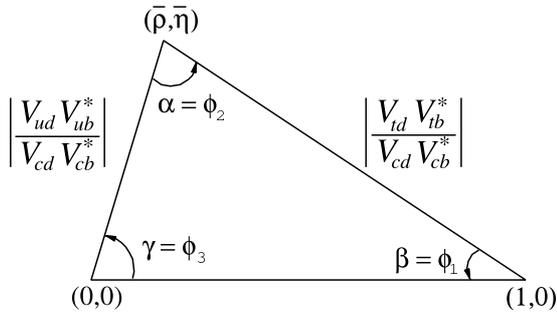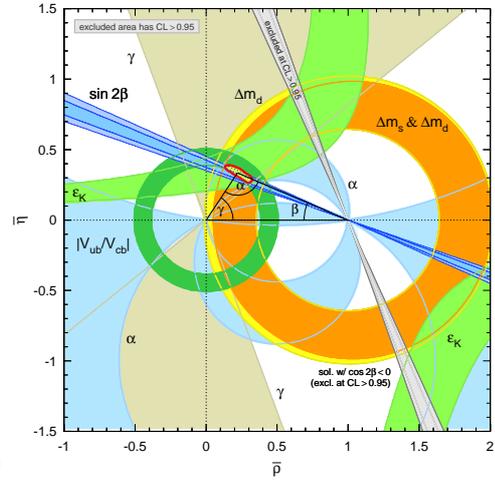
Figure 1.3: *One of the Unitarity Tri-angles.*

Figure 1.4: *Constraints to the UT obtained by the experimental results.*

- indirect CP violation in the neutral kaon system, is measured by the parameter $\varepsilon_K$ which constrains the upper vertex of the UT to a central region of the $\bar{\rho} - \bar{\eta}$ plane;

- the BR of the $B_d^o \to J/\psi K_S$ decay is used to determine $\sin 2\beta$ [10, 11].

CP violation is deeply bound to the fermion masses and to the multiplicity of fermion families, therefore it is a crucial point in the understanding of particle physics. Furthermore, the size and the origin of CP violating phenomena strongly depend on the scenario of new physics underlying the SM. For this reason, the possibility to study the $B$-system at the luminosity offered by LHC and at a future new super-$B$ factory would shed a new light on a complex and obscure sector of fundamental physics.

## 1.2 Potential discoveries and measurements at LHC

LHC has been built to discover the Higgs boson in a wide mass range, to detect new phenomena at the TeV scale and to cover a rich physics program on top and flavour physics.

The SM $H$ production processes, in p–p collisions, are represented in Fig. 1.5. Fig. 1.6 shows, for each production channel, the cross section as a function of the expected Higgs mass $m_H$ [12]. Gluon–gluon fusion (Fig. 1.5a), with a top



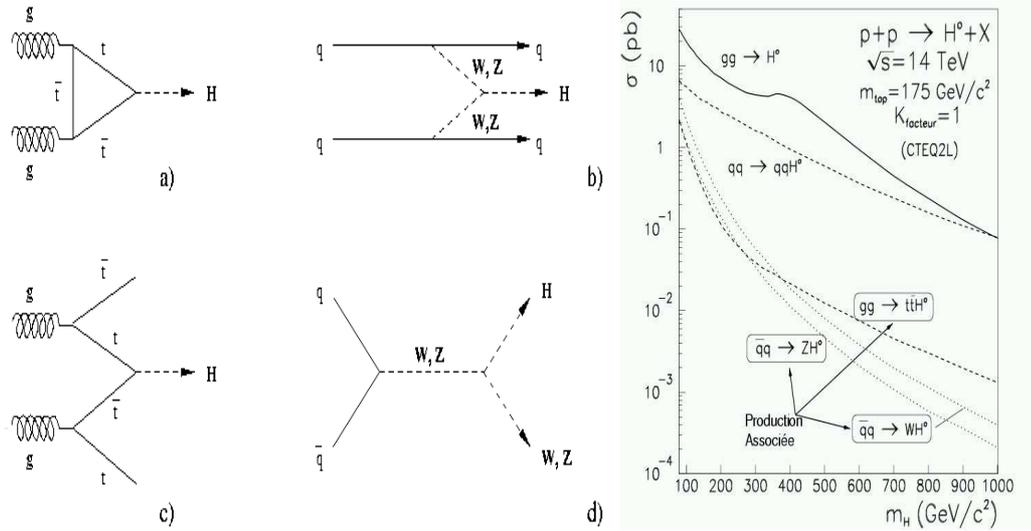Figure 1.5: *Feynman diagrams for the most relevant production processes of the Higgs boson at LHC.*

Figure 1.6: *Cross section of the different production processes of the Higgs boson at LHC.*

quark in the loop, is the most probable in the entire $m_H$ allowed range. Two boson, $W$ or $Z$, fusion (Fig. 1.5b) grows with increasing $m_H$ and becomes of the same order as gluon–gluon fusion at $m_H \simeq 1$ TeV/c$^2$. The associated

production of $H$ with $t\bar{t}$ or with $W$ or $Z$, although rare compared to the previously mentioned production channels, are experimentally intersting due to the distinctive signature of the final state.

The identification of the Higgs boson depends on the value of its mass which determines its decay branching fractions (Fig. 1.7). For this reason, different strategies must be used for the following four Higgs mass ranges:

1. $m_H \leq 130$ GeV/c$^2$;

2. 130 GeV/c$^2 \leq m_H \leq 2m_Z$;
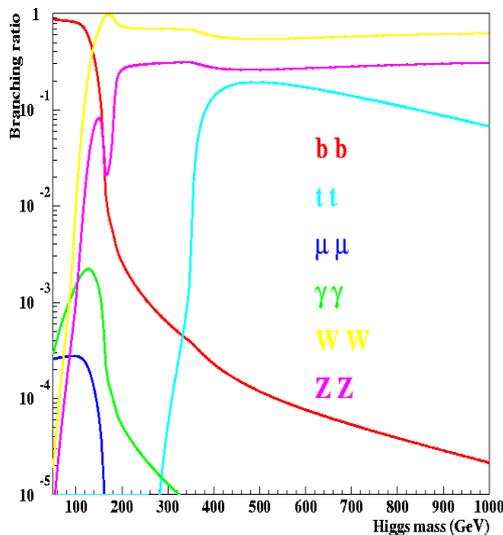
3. $m_H \geq 2m_Z$;

4. $m_H \geq 600$ GeV/c$^2$.



Figure 1.7:  *Higgs boson Branching Ratio for different channels in function of the $m_H$.*
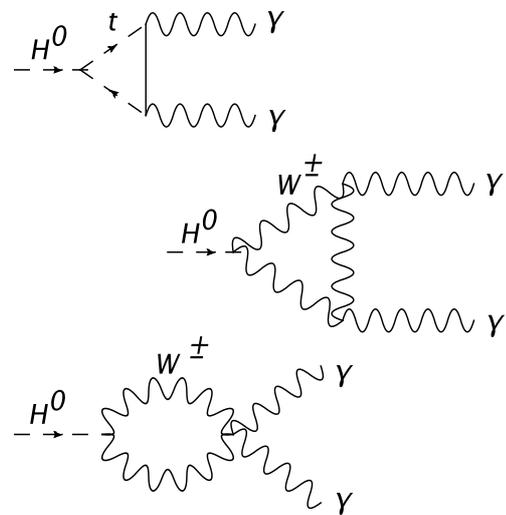
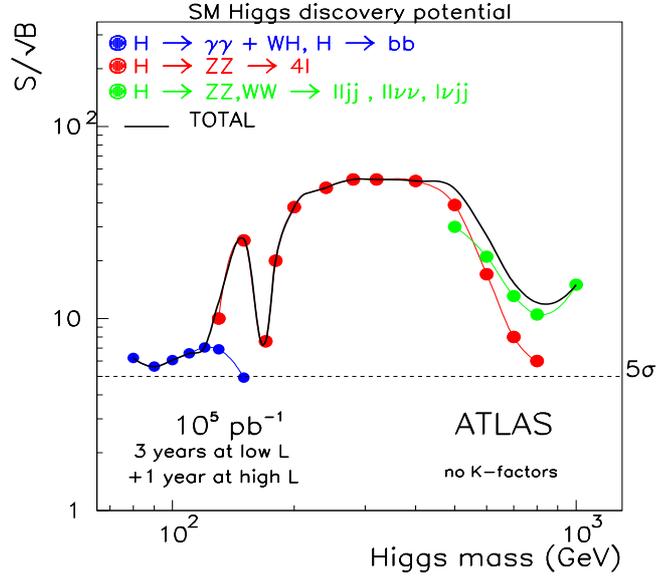Figure 1.8:  *Diagram of Higgs boson disintegration in two photons.*

Figure 1.9: *Higgs boson discovery potential, expressed as $\frac{S}{\sqrt{B}}$, at the ATLAS experiment in function of $m_H$ after an integrated luminosity of $\int Ldt = 10^5$ $pb^{-1}$.*

In the first Higgs mass range the $H$ boson decays to $b\bar{b}$ pair with a BR $\sim$ 100%. In order to isolate the signal from the continuous background of $b\bar{b}$, associated $H$ production processes have to be exploited. For example, the signal over background ratio can be enhanced by requiring an isolated lepton with high $p_T$ ($p_T > 6$ GeV/c for a muon, or $p_T > 30$ GeV/c for an electron) that comes from W, Z or $t\bar{t}$ decay. The $H$ signal will be observed as a peak in the invariant mass spectrum of the $b\bar{b}$ system.

In this $m_H$ range another important decay, despite its low BR (Fig. 1.7), is $H \rightarrow \gamma\gamma$ (Fig. 1.8). The high performance e.m. calorimeters of ATLAS and CMS as actually designed in order to allow the identification of a tiny $H$ signal in the $m_{\gamma\gamma}$ spectrum over the huge non reducible backgrounds from $q\bar{q}, gg \rightarrow \gamma\gamma$, *jet–jet* and *jet–$\gamma$*.

In the second and third mass range it is possible to detect the $H \rightarrow ZZ^* \rightarrow 4l^{\pm}$ decay where the real Z decays to two leptons with high $p_T$ and invariant mass equal to $m_Z$ and the virtual Z produces two leptons with high $p_T$. For $m_H > 2m_Z$ the $4l$ invariant mass exhibits a peak at $m_H$ on top of the relatively low continuum background from $ZZ^*$ and $Z\gamma^*$. At $m_H < 2m_Z$ large reducible backgrounds come from $t\bar{t} \rightarrow Wb + W\bar{b} \rightarrow l\nu + l\nu\bar{c} + l\nu + l\nu c$ and $gg \rightarrow Zb\bar{b} \rightarrow 4l^{\pm}$. However, they can be rejected by requiring that the leptons are isolated, come from the primary vertex and that a lepton pair comes from a $Z$.

In the last mass range the most promising channels are $H \rightarrow ZZ \rightarrow ll\nu\nu$ and H$\rightarrow WW \rightarrow l\nu jj$ because the high $Z \rightarrow \nu\nu$ and $W \rightarrow jj$ branching fractions compensating the lower production cross section. However, it is hard to reconstruct these events because there are some neutrinos and hadronic jets in the final states, therefore hermetic calorimetry and good hadronic jet resolution are fundamental.

In Fig. 1.9 the statistical significance $\mathbf{S}/\sqrt{\mathbf{B}}$ (Signal/$\sqrt{Background}$), for the different SM Higgs boson channels that will be searched at ATLAS, is drawn. It can be noticed that there is a minimum at $m_H \simeq 170$ GeV/c$^2$ corresponding to the minimum of BR for the golden channel $H \rightarrow ZZ$. From the plot is clear that the SM Higgs can be discovered at LHC if it has a mass in the range from 90 GeV/c$^2$ to 1 TeV/c$^2$.

Important results can be obtained on CP-violation by studying the $B$ meson system at LHC. The cross section for $b\bar{b}$ pair production is $\sim 0.5$ mb which implies a rate of $\sim 5 \times 10^{12}$ events/year at LHC in the low luminosity phase ($10^{33}$ cm$^{-2}$s$^{-1}$). The best channel to search for CP-violation is $B_d^0 \rightarrow J/\psi K_S^0$ because of the relatively easy signatures of $J/\psi$ and $K_S^0$. The $\beta$ angle of the UT can be measured from the asymmetry in the decay time

of the $B_d^0, \overline{B_d^0} \rightarrow J/\psi K_S^0$. The measure can be done by simultaneously:

- recognizing the flavour of the $B$ meson using the semileptonic decays of the other $B$ (*b tagging*);

- identifying the $K^0$ by looking for two $\pi$ with opposite charge, $M_{\pi^+\pi^-} \sim m_{K^0}$, and $p_T > 0.5$ GeV/c;

- identifying $J/\psi$ by requiring two muons, one with $p_T > 6$ GeV/c and the other with $p_T > 3$ GeV/c;

- requiring that the $J/\psi$ vertex is displaced from the interaction point by more than 250 $\mu m$.



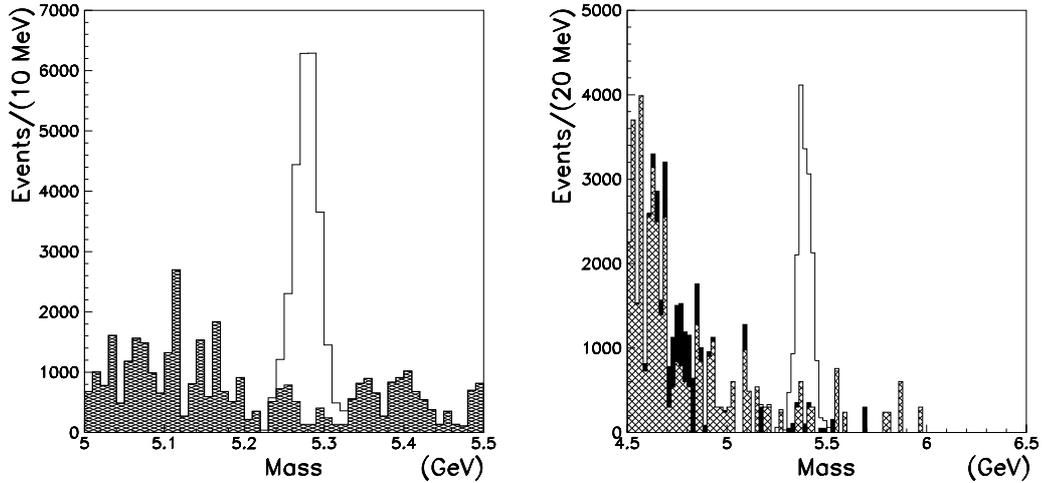Figure 1.10: *$J/\psi K_S^0$ invariant mass reconstruction* (a),*and of the $J/\psi\phi$* (b).

Taking into account branching ratio, detector, and event selection efficiencies the number of expected events for this channel is $\sim 22000$ in one year. The background is expected to be of $\sim 2600$ events and arises, mainly, from lepton production at low $p_T$, muons from decays in flight of light mesons

$(\pi^{\pm}, K^{\pm}, K^0)$.

Another channel that will be used to study CP-violation is $B_S^0 \rightarrow J/\psi\phi$ that can give a measure of the $\gamma$ angle of the UT. In the SM the expected asymmetry for this channel is equal to 0.03. If a different value will be measured it would represent a strong indication of New Physics. The strategy to select $B_S^0 \rightarrow J/\psi\phi$ is similar to that for $B_d^0 \rightarrow J/\psi K_S^0$ with the following differences:

- the $\phi$ is identified by looking for two particles with opposite charge and $p_T > 0.5$ GeV/c separated by an angle small as than $11.5^o$;

- the $\phi$ vertex must be displaced from the interaction point by more than $100~\mu$m.

For this channel $\sim 15000$ events with $\sim 2900$ background events are expected.

## 1.3 The future Linear Collider

LHC will offer great possibilities to investigate with high accuracy many aspects of elementary particles physics and to discover new physics beyond the SM. However, hadron collider suffers high irreducible background that can mask some interesting physics channels. New precision measurements at a lepton collider would be essential to consolidate LHC results and to scrutinize the nature of new particles or phenomena observed. Different proposals have been made for Linear Collider $e^+e^-$ machines, NLC [13], JLC [14] and TESLA [15] in past years. They have all converged into the International Linear Collider project. The machine proposed for ILC consists of two linear accelerators, located on a path of 35 kilometers (Fig. 1.11), that hurl bunches of $10^{10}$ electrons and positrons toward each other. Superconducting
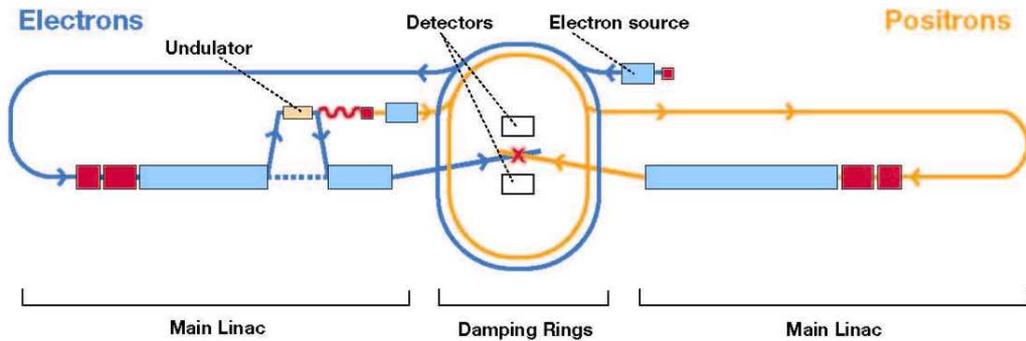
Figure 1.11:  *Scheme of the ILC machines.*

accelerator cavities operate at temperature of 1.8 K and the beams collide 14000 times every second. ILC is designed to have the following properties:

- Energy of the Center of the Mass adjustable from 200–500 GeV;

- energy stability and precision better than 0.1%;

- peak luminosity 2-6$\times 10^{34}$ cm$^{-2}$s$^{-1}$;

- an integrated luminosity of 500 fb$^{-1}$ after the first five years of ILC life;

- electron polarization of at least 80% (positron polarization, if possible);

- the entire project is such that an upgrade to the energy of 1 TeV is possible.

In addition to $e^+e^-$ collisions, linear colliders provide a possibility to study $\gamma\gamma$ and $\gamma e$ interactions at energies and luminosities comparable to those in $e^+e^-$ collisions [16]. High energy photons for $\gamma\gamma$, $\gamma e$ collisions can be obtained from Compton scattering of a laser light on high energy electrons like sketched in Fig. 1.12.
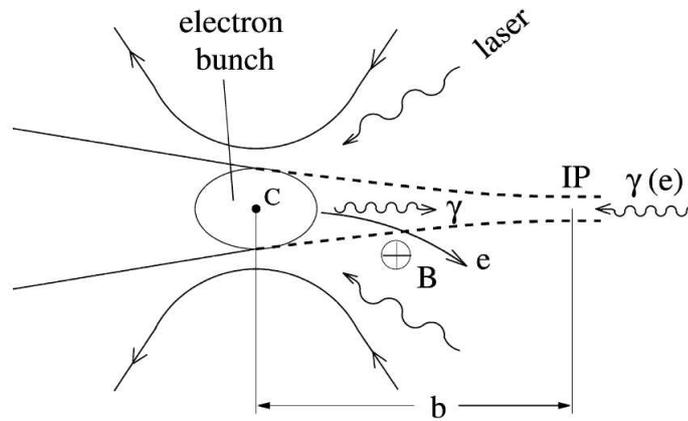
Figure 1.12: *Scheme of $\gamma\gamma$, $\gamma e$ collider.*

At ILC the well known $\sqrt{s}$ and the limited background ensure higher accuracy than at LHC; moreover, the possibility to polarize the beams allows to perform measures that are not allowed at LHC. Therefore, ILC and LHC are complementary in the Higgs investigation program because of the highly precise measurements possible at the ILC and the wide mass range coverage at the LHC. In case of the discovery of particles predicted by supersymmetric theories, LHC and ILC will be able to access different sectors of the spectrum of supersymmetric particles. If the two accelerators would run concurrently results from the ILC used as input for analysis at the LHC will significantly improve and extend the scope of the measurements carried out at the LHC. The information from both the LHC and ILC will be crucial in order to reliably determine the underlying structure of the supersymmetric theory, which should open the path to the ultimate unification of forces and give access to the structure of nature at scales far beyond the energy reach of any conceivable future accelerator.

It is important to bear in mind that ILC should work untriggered in order to

increase the potential to reveal new physics in a fully unbiased way, avoiding cuts imposed by a trigger. Also in this respect, ILC might be useful to tune the LHC triggers on unexpected new physics.

## 1.4   The Super B factory

Over the last seven years the two asymmetric B Factories, PEP-II [17] and KEKB [18], and their detectors, BABAR [19] and Belle [20], have measured some aspects of flavour physics producing a series of stringent tests that are passed by the SM. Therefore continued detailed studies, as we have seen before, of heavy quark and heavy lepton physics will be central to understanding the flavour sector of New Physics phenomena. So the construction of a very high luminosity asymmetric $e^+e^-$ Flavour Factory (SuperB), that would come into operation in the first half of the next decade, with a peak luminosity of $\sim 10^{36}$ cm$^{-2}$s$^{-1}$ at the $\Upsilon(4S)$ resonance is being proposed. The machine should be able to acquire 15 ab$^{-1}$ per year and the interaction energy will be 7 GeV + 4 GeV.

The flavour physics program that can be accomplished in a very clean environment of an $e^+e^-$ collider is complementary to that of an experiment such as LHCb [21], the experiment for $b$ physics at LHC. The capabilities of SuperB in measuring CP-violating asymmetries in very rare $b$ and $c$ quark decays, accessing branching fractions of heavy quark and heavy lepton decays in processes that are either extremely rare or forbidden in the Standard Model, and making detailed investigations of complex kinematic distributions will provide fundamental constraints to ascertain the type of supersymmetry breaking or the kind of new phenomena that is expected to be manifest at the LHC.

# 1.5 Experimental requirements at future colliders

The experiments that are under study for the ILC and SuperB factory are very challenging due to strict operational requirements. In particular, the ILC tracking system needs to achieve a major improvement in performance compared to all predecessors and at SuperB the detector will work in an unprecedented luminosity environment.

At ILC final states including jets in the forward region will be particularly important, due to multi-jet processes, where one or more happen to be directed forward, and to 2-jet processes where this region may be particularly sensitive to new physics. Hence it will be essential that the tracking system performs in the forward region as well as in the central one. Therefore a nearly 100% track finding efficiency is needed over the full solid angle with momentum resolution of $\sigma(p_T)/p_T^2 \leq 5 \times 10^{-5}$ $(\text{GeV/c})^{-1}$. The energy-flow resolution for hadronic event should be of $\sigma/E \sim 30\%/\sqrt{E}$ in order to separate hadronic $W$ and $Z$ decays. Finally, strong particle identification based on secondary vertex detection is required, since several channels from New Physics (e.g. SUSY) involve b-quarks or $\tau$-leptons.

The requirements for a detector at a SuperB factory are not different from than those driving the design of the BABAR and BELLE experiments. Particular care will be devoted to the optimization of the vertex subdetector in order to enhance the heavy flavour tagging capabilities. However a central tracker with the resolution achieved by the BABAR drift chamber, $\sigma(p_T)/p_T = (0.13 \pm 0.01)\% \times p_T + (0.45 \pm 0.03)\%$, would be marginal given the physics objectives of SuprerB and provided the granularity is optimized to cope with the higher luminosity environment and its consequent

increase in hit multiplicity.

# Chapter 2

# Detectors for Momentum measurement and Particle Identification at Colliders Experiments

## 2.1  Charged particle detection

A charged particle loses energy in matter resulting predominantly in, by electromagnetic interaction in free charges, electrons and ions liberated in the medium. These charges can follow an externally applied electromagnetic field and can be collected producing an electrical signal. In this chapter, before describing momentum measurement and particle identification, we will examine the formalism describing the motion of the free charges in an electromagnetic field traversing a gaseous medium.

### 2.1.1   Particle interactions with matter

Two types of interactions must be considered for charged particle detection, electromagnetic and nuclear interactions. In gaseous detectors, the electromagnetic interaction is more relevant in terms of energy loss and will therefore be described here. A fast charged particle traversing a medium interacts with the electromagnetic field generated by the atomic electrons and the nuclei located along its trajectory, producing several processes:

- inelastic collisions with atomic electrons resulting in both excitation and/or ionization of the atoms of the medium;

- bremsstrahlung, i.e emission of photons in the e.m. field of the nuclei and of the atomic electrons. The energy loss in this process depends on the ratio of the particle energy to its squared mass. Consequently, this process dominates the ionization loss for electrons at energies as low as 10 MeV. For muons and pions, this dominance occurs at several hundreds of GeV;

- elastic scattering on the nuclei and on the atomic electrons, leading to deviation of the original particle direction.

### 2.1.2   Energy loss due to electromagnetic interactions

Relativistic charged particles heavier than the electron lose energy by collisions with atomic electrons creating excited atoms or electron-ion pairs. The quantum expression of the mean energy loss per unit length of traveled material, normalized to the medium density, is given by the Bethe-Bloch equation [22]:

$$-\frac{dE}{dx} = kz^2 \frac{Z}{A} \frac{1}{\beta^2} \left[ \frac{1}{2} \ln \frac{2m_e c^2 \beta^2 \gamma^2 T_{max}}{I^2} - \beta^2 - \frac{\delta}{2} - \frac{C}{Z} \right] \qquad (2.1)$$

where A, Z, and I are respectively the atomic weight, the atomic number, and the mean excitation potential of the traversed material; $z$ is the particle charge, expressed in unit of the elementary charge $e$, and $\beta c$ is its velocity; the constant, $k \simeq 0.307$ MeV $g^{-1}\text{cm}^2$; $\delta$ and C are factors needed to take into account, respectively, the density and shell effects; $T_{max}$ represents the maximum kinetic energy which can be imparted to a free electron in a single collision, like a head-on or *knock-on* collision, it is given by:

$$T_{max} = \frac{2m_e c^2 \beta^2 \gamma^2}{1 + 2\gamma m_e/M + (m_e/M)^2}$$

where $M$ is the particle mass. In Fig. 2.1 is reported the Bethe-Bloch function for different particles in different materials. In Eq. 2.1 we notice that:

- the dependence on M introduced through $T_{max}$ is negligible and becomes sizeable only at high energy, i.e. about 100 GeV for pions. So, in a first approximation, we can consider that the differential energy loss depends only on the velocity of the incident particle and does not depend on its mass. The energy loss is only slightly dependent on the chemical composition of the material through the ratio $Z/A$, so the minimum energy loss in hydrogen is exceptionally large because its $Z/A=1$;

- at low energy, the ionization loss falls with the $\beta^{-2}$ term and reaches a broad minimum at $3 \leq \beta\gamma \leq 4$. For most materials, the energy loss per unit length is $\simeq 2$ MeV/$g$/cm$^2$ at this minimum. At relativistic velocities ($\gamma \gg 1$), the Bethe-Bloch equation is dominated by the logarithmic term due to two effects. Firstly the transverse component of the particle electric field acquires a factor when transformed into the laboratory frame, so that the field of the particle extends to greater

distances from the trajectory and more collisions can occur. Secondly the maximum transferable energy $T_{max}$ rises as $\gamma^2$;

- at ultra-relativistic velocities, the energy loss reaches the Fermi plateau. The cancellation of the relativistic rise results from the medium polarization by the incident particle electric field. This shielding limits the extension of the field and reduces the influence of collisions with a large impact parameter.

From figure 2.1 we have that slow particles undergo a huge ionization so they are called highly ionizing particles (HIP) and that the particles that lose an energy close to the minimum are called minimum ionizing particles (MIP). The total energy deposited by an ionizing particle in a thin gas volume results from a small number of interactions, each having a large range of possible energy transfers. Therefore the total energy fluctuates around the most probable value given by Eq. 2.1 presents an asymmetric distribution, called the Landau distribution [23], which can be approximated by:

$$f(\lambda) = \frac{1}{\sqrt{2\pi}} e^{-\frac{1}{2}(\lambda + e^{-\lambda})}$$

where $\lambda$ is a reduced variable representing the normalized deviation of the energy loss from the most probable energy loss, $\lambda = \frac{\Delta E - (\Delta E)_{m.p.}}{\xi}$, with $\xi = kz^2 \frac{Z}{A} \frac{1}{\beta^2} x\rho$ (where $x$ is the thickness of the absorber).

### 2.1.3   Drift and diffusion of electrons in gases

The motion of free charges in the matter under the influence of electric and magnetic fields, $\mathbf{E}$ and $\mathbf{B}$, may be understood in terms of an equation of motion with friction:

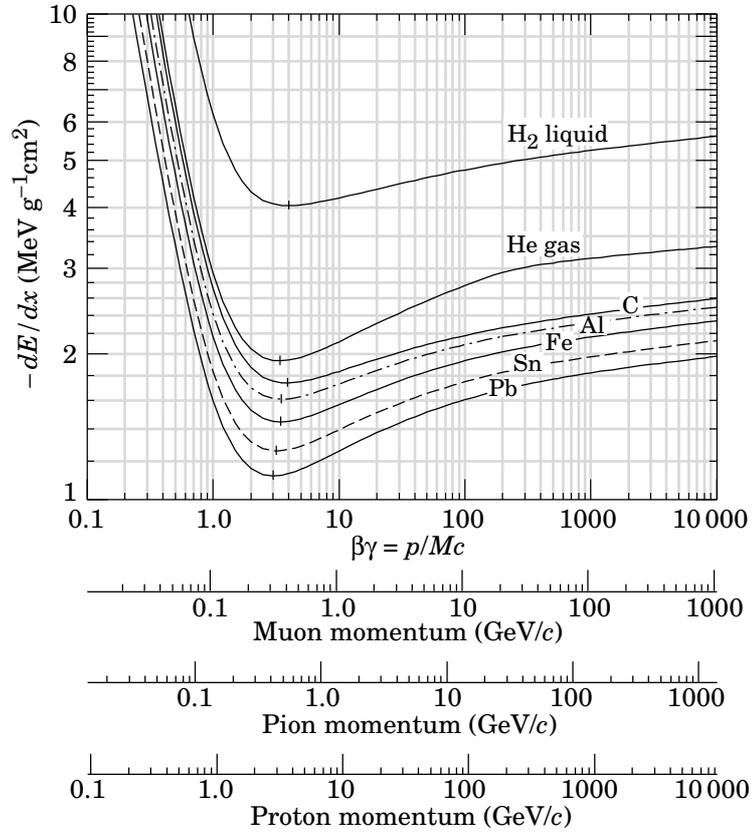$$m\frac{d\mathbf{u}}{dt} = q\mathbf{E} + q[\mathbf{u} \times \mathbf{B}] - K\mathbf{u} \tag{2.2}$$

Figure 2.1: *Mean energy loss rate in liquid hydrogen, gaseous helium, carbon, aluminum, iron, tin, and lead for different particles [22].*

where $m$ and $q$ are the mass and the charge of the particle, $\mathbf{u}$ is its velocity and $K\mathbf{u}$ is a frictional force caused by collisions of the particle with the gas molecules. For large $t$ ($t \gg m/k = \tau$, where $k$ depends on the gas) the increasing friction force compensates the accelerating electromagnetic force leading to a constant drift velocity, $v_d$, solution of the steady state equation $dv_d/dt=0$:

$$\frac{<\mathbf{u}>}{\tau} = \frac{q}{m}(\mathbf{E}+ <\mathbf{u}> \times\mathbf{B}).$$

In this equation, the right hand side corresponds to the average acceleration of the electrons between consecutive collisions, due to the electromagnetic force, and therefore $\tau$ can be considered as the average time between collisions. In the absence of a magnetic field, the above equation can be written:

$$v_d = \frac{q}{m}\mathbf{E}\tau = \mu_q\mathbf{E} \ , \quad \mu_q = \frac{q\tau}{m}$$

where $\mu_q$ is called charge mobility.

In absence of on electric field, the gas molecules undergo thermal agitation as described by the classic kinetic theory. The charges released by an ionizing particle behave in a similar way: the classic kinetic theory attributes to each particle, with three degrees of freedom, an average kinetic energy $\epsilon_T = \frac{3}{2}kT$ ($\simeq 0.04$ eV in the normal conditions of temperature and pressure), where $k$ is the Boltzmann's constant and $T$ the gas temperature. In absence of other forces, the charges locally distributed diffuse by multiple scattering following the Gauss law:

$$\frac{dN}{dx} = \frac{N_0}{\sqrt{4\pi Dt}}e^{-\frac{x^2}{4Dt}} \tag{2.3}$$

where $N_0$ is the total number of charges localized at $x=0$ at $t=0$, $D$ is the diffusion coefficient and $dN(x)$ represents the fraction of charges located in the element $dx$ at the distance $x$, at the time $t$. The standard deviation of the distribution in one dimension is given by $\sigma_x = \sqrt{2Dt}$. The diffusion coefficient is a parameter which can be calculated from the kinetic theory:

$$D = \frac{2}{3}\frac{\epsilon}{m}\tau \ , \quad \epsilon = \frac{3}{2}kT \tag{2.4}$$

where $\tau$ is the average time between collisions. Eq. 2.4 shows that, due to their smaller mass, the diffusion coefficient for electrons is much larger than the analogous coefficient for positive ions.

In the presence of an external force, like in an electric field, the electrons

and the ions are accelerated along the field lines towards the anode and the cathode, respectively, and the average kinetic energy becomes:

$$\epsilon = \frac{1}{2}mv^2 = \epsilon_E + \frac{3}{2}kT$$

where $\epsilon_E$ is the average energy acquired in the electric field. At values of drifting fields commonly used in gaseous detectors, a few hundred of V/cm, $\epsilon_E$ amounts to a few electron-volts. Therefore the contribution of the thermal energy can be neglected and the value of the diffusion coefficient is affected by the presence of an external field. It is been observed that the value of the electron diffusion in the direction of the electric field can be quite different from that in the transverse direction. Therefore two diffusion coefficients are introduced $D_L$ and $D_T$, respectively, for the longitudinal and the transverse direction with respect to the electric field.

## 2.2 Central tracking systems to measure the particle momentum

The goal of a central tracking system is to reconstruct the trajectory of charged particles with high efficiency and to measure their momentum and direction at the production vertex. The particle trajectory can be determined by measuring a set of points along the particle path. Since charged particles in a uniform magnetic field **B** describe a helical trajectory around the field axis, the momentum of the particles can be obtained in cylindrical coordinates $(\rho, \phi, \theta)$ from:

$$p = p_T \, \sin\theta \, , \quad p_T = 0.3 \, z \cdot \mathbf{B} \cdot \rho \tag{2.5}$$

where $p_T$ is the component of the particle momentum in a plane transverse to the magnetic field, $\theta$ is the polar angle between the particle direction and

the magnetic field axis and $\rho$ is the radius of curvature. Notice that using **B** expressed in Tesla and $\rho$ in meter, the value of $p$ is in GeV/c. Eq. 2.5 shows that the momentum resolution has contributions from the errors on the track curvature and on the polar angle. In addition, the momentum resolution suffers also from multiple Coulomb scattering in the material traversed by the particle. Consequently the momentum resolution can be written as follows:

$$\left(\frac{\sigma_p}{p}\right)^2 = \left(\frac{\sigma_{p_T}}{p_T}\right)^2 + \left(\frac{\sin\lambda}{\cos\lambda}\sigma_\lambda\right)^2 + \left(\frac{\sigma_p^{m.s.}}{p}\right)^2 \qquad (2.6)$$

where $\lambda = \pi/2 - \theta$ and $\sigma_p^{m.s.}$ is the contribution to the momentum resolution due to the multiple scattering which depends both on $\phi$ and on $\lambda$.

In the case of $N$ uniform spaced points measured along the track, the error on $p_T$ due to the spatial resolution of the detectors is given by[1] [22]:

$$\frac{\sigma_{p_T}}{p_T} = \frac{p_T}{0.3z\mathbf{B}}\frac{\sigma_{\rho\phi}}{l^2}\sqrt{\frac{720}{N+4}} \qquad (2.7)$$

where $\sigma_{\rho\phi}$ is the spatial resolution of the detector elements in the $\rho - \phi$ plane, $l = \rho_{max}$ is the radial size of the tracker. The above formula shows that the intrinsic momentum resolution degrades linearly with the transverse momentum but improves with the magnetic field and with the square of the radial size of the tracker. It is important to note that given the values of **B** and $l$ in Eq. 2.7, an equivalent value for the intrinsic momentum resolution can be obtained by measuring either few points ($N$) with high precision ($\sigma_{\rho\phi}$) or many points with lower precision. The error on the polar angle due to the measurements along the particle trajectory is given by:

$$\frac{\sin\lambda}{\cos\lambda}\sigma_\lambda = \sin\lambda\cos\lambda\sigma(\tan\lambda) \qquad (2.8)$$

---

[1]If a vertex constraint is applied at the origin of the track, the coefficient under the radical becomes 320.

where :

$$\sigma(tg\lambda) = \frac{\sqrt{12}\sigma_z}{l\sqrt{m}} \quad , \quad \sigma_z = \frac{\sigma_{\rho\phi}}{\sin\epsilon} \tag{2.9}$$

and $m$ is the number of stereo measures.

At low transverse momenta ($\sim$ GeV/c), the momentum resolution is limited by multiple scattering. The particle track deviation from its original direction due to the multiple scattering is well described by the Molière theory. In the range of small deviation it can be approximated by a Gaussian distribution with a width given by:

$$\Theta = \frac{13.6 MeV}{\beta c\, p} z \sqrt{\frac{x}{\boldsymbol{X}_0}} \left[ 1 + 0.038\, ln\left(\frac{x}{\boldsymbol{X}_0}\right) \right] \tag{2.10}$$

where $p$ is the momentum of the particle, $x$ is the thickness of the medium, with radiation length $\boldsymbol{X}_0$, crossed by the particle. The irreducible multiple scattering contribution to the transverse momentum resolution and to the track angle resolution can be calculated by:

$$\frac{\sigma_{p_T}^{m.s.}}{p_T} = \frac{0.054}{\beta\, L \cos\lambda} \sqrt{\frac{L}{\boldsymbol{X}_0}} \tag{2.11}$$

$$\sigma_\lambda^{m.s.} = \frac{0.0083}{\beta p} \sqrt{\frac{L}{\boldsymbol{X}_0}} \tag{2.12}$$

where $L$ is the length of the particle path. Consequently, the intrinsic momentum resolution is the dominant error for particles of high transverse momentum while at low transverse momentum the tracker performance is spoiled by the multiple scattering.

In the following paragraphs we give a brief description of the principle technical solutions adopted for a central tracker system.

## 2.3   Silicon tracking chambers

A silicon detector, either pixel or microstrip, guarantees great precisions, spatially of the order of a few microns, and a short response time, $\sim$ 5 ns.
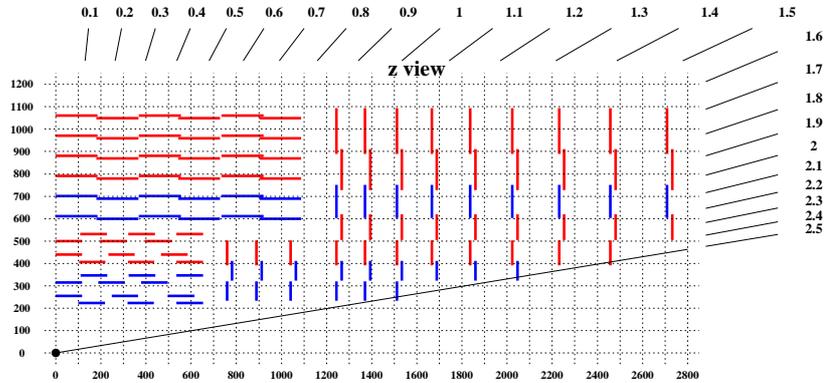
Figure 2.2: *Schematic $(z, r)$ view of the CMS tracker.*

Such detectors are mainly used to build high performance tracking systems. The basic idea is to create a few ($\sim 10$) cylindrical shells around the $z$-axis and circular wheels perpendicular to $z$, at fixed distances from the collision point, that are uniformly covered with many elementary detectors. The most complete and innovative example of such a central tracking system is that of the CMS experiment at LHC. In Fig. 2.2 a schematic view of the CMS central tracker with 10 cylindrical shells and 13 orthogonal wheels is shown. In Fig. 2.3 the expected resolution for single muons of transverse momenta of 1, 10 and 100 GeV/c as a function of pseudo-rapidity ($\eta$) is shown [24]. For high momentum tracks (100 GeV/c) the transverse momentum resolution is around 1-2% up to $|\eta| \approx 1.6$, beyond which it degrades since the number of measurements drastically reduces. At 100 GeV/c, multiple scattering in the tracker material accounts for 20 to 30% of the transverse momentum resolution while at lower momenta ($\lesssim 30$ GeV/c) multiple scattering dominates. Figure 2.4 shows the expected track reconstruction efficiency of the CMS
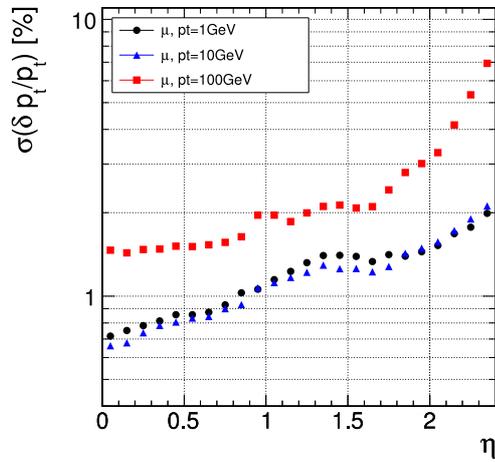
Figure 2.3: *CMS tracker. Expected transverse momentum resolution for single muons as a function of η.*
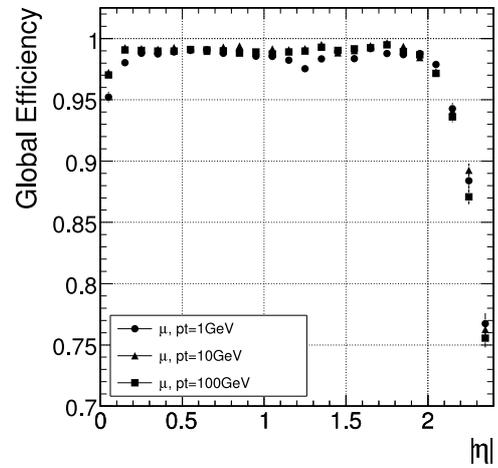
Figure 2.4: *CMS tracker. Expected track reconstruction efficiency for muons.*
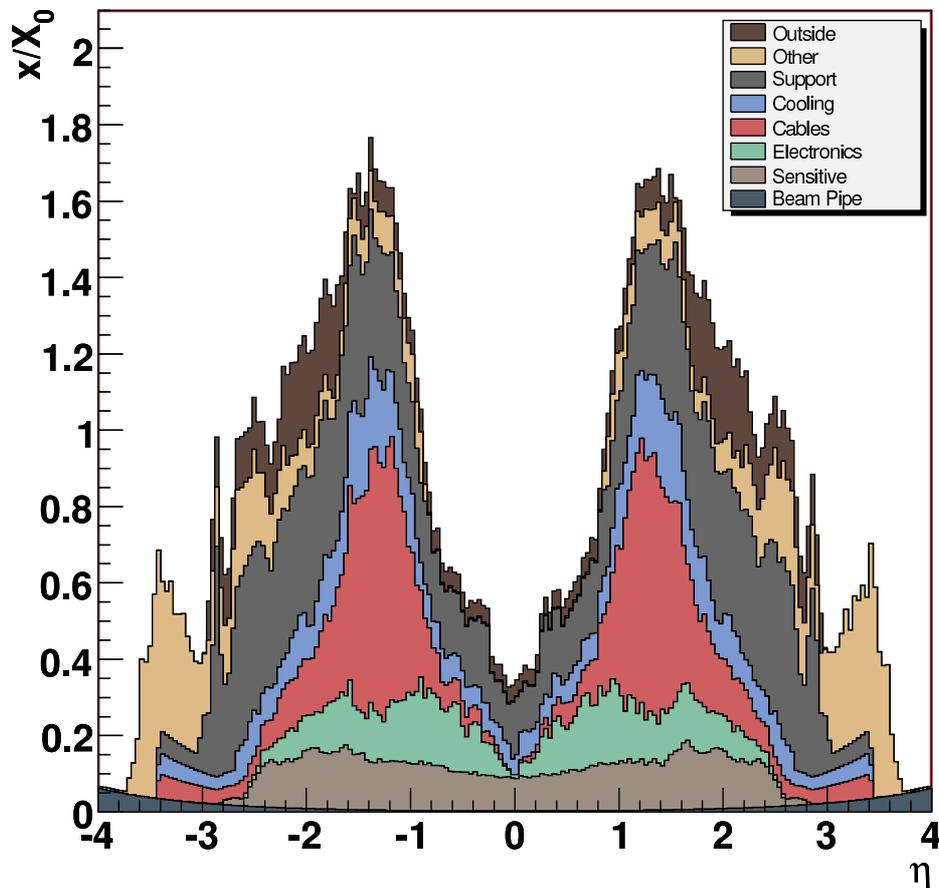


Figure 2.5: *Material budget in units of radiation length as a function of pseudo-rapidity η for the whole CMS tracking system, central plus inner.*

tracker for single muons as a function of pseudo-rapidity, which is about 99% over most of the acceptance. For pions and hadrons in general, the efficiency is lower because of their interactions with the tracker material. The amount of material, in units of radiation length, of the CMS central and inner tracker is reported in Fig. 2.5. In this kind of systems, the silicon is not the only material present but there is also a large amount of material due to mechanical supports, to electronics read-out, to cables and to cooling systems. The cooling system is essential for a silicon systems that needs to survive and to work in a high radiation environment. Further drawbacks for a silicon tracking system are the large number of elementary detectors and read-out channels ($\sim 3 \times 10^4$ and $\sim 10^7$, respectively for CMS) their relative alignment and their considerable cost.

## 2.4 Time Projection Chambers

The TPC is a gaseous tracking system based on the drifting of the electrons and ions. It has a cylindrical volume, filled with gas, with its axis along the beam direction and along the direction of the solenoidal B field surrounding it, Fig. 2.6. A negative high voltage (HV) electrode is located perpendicular to its axis dividing the gas volume in two symmetric drift regions. In both drift regions, between the negative HV electrode and end plates, a highly uniform electrostatic field is created. A crossing charged particle ionizes the gas along its path and the free electrons move with a constant velocity to either of the two end plates. The end plates are equipped with special devices, like Multi Wire Proportional Chamber[25], GEM[26] or MICROMEGAS[27], to amplify and detect the signal generated by the arrival of the drifting electrons. In the $x - y$ plane, the position of an electron typically is measured
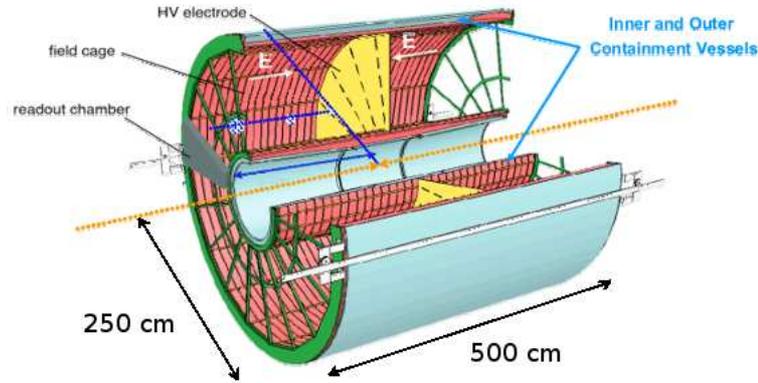
Figure 2.6:  *The ALICE TPC layout.*

with a precision of $\sigma \sim 200$ $\mu$m. The $z$ position can be known with a precision of $\sim 1$ mm by measuring the electron drift time (the maximum drift time for a free electron that start to drift from the TPC center is typically of the order of several hundred $\mu s$). Despite the long drift path, the transverse diffusion is moderate since the axial magnetic field, parallel to the drift direction, reduces the lateral diffusion by a factor of $\sim \omega\tau$ ($\frac{D_T(\omega)}{D_T(0)} = \frac{1}{1+\omega^2\tau^2}$), where $\omega = e\mathbf{B}/m$ is the cyclotron frequency.

A TPC typically can measure $\sim 100$ points on the projected track reaching a high resolution on $p_T$ and allowing for a good particle identification capabilities by measuring $dE/dx$. The TPC designed for the ALICE experiment, at LHC, can reach values of $\sigma(1/p_T) \gtrsim 5 \times 10^{-4}$ GeV/c.

The limiting factors of a TPC are represented by:

- long drifting time which implies an integration over many interactions and, therefore, a complex pattern recognition;

- large amount of material:

  - grid for sweeping off the positive ions in the amplification region;

- electrodes at $z = 0$;

- external devices for amplification;

- heavy gas.

- distortions of the E-filed at high rates, due to the positive ions which are liberated in the ionization process and which take a very large time to reach the central negative electrode.

## 2.5 Drift Chambers

In this section we give only a brief description of the principal aspects of a single-wire-cell central Drift Chamber. An in-depth description of our proposed Drift Chamber will be given in the next chapters.

Such chamber is a gaseous tracking system that can be assimilated to a system of proportional wire detectors in a wide cylindrical volume, filled with a gas mixture. The sense wires are strung axially (or para-axially) to the chamber and are surrounded by a number of cathode wires in an electrostatic configuration similar to the elementary cell of a proportional counter. A particle crossing these cells leaves a signal enabling the track reconstruction in space. The free electrons and ions, produced by the ionizing particle, drift respectively to the anode and to the cathode wires under the action of the applied electrical field, producing a signal that is read and used to measure the distance of the track from the anode wire: the impact parameter. In a typical Drift Chamber the impact parameter is measured with an accuracy of $\sim 120~\mu$m.

The layout of the cells and the electrical potential applied are optimized according to the experiment requirements.

A Drift Chamber with a Helium gas mixture and with $\sim 100$ layers of cells

reaches, at low momenta, a momentum resolution better than a TPC, because of the smaller contribution due to the multiple Coulomb scattering and to the lower diffusion, given the shorter drift distances.

A limiting factor of a Drift Chamber is the scarce resolution on $z$. This can be overcome by inserting layers of wires tilted with respect to the $z$. These are called stereo layers and resolutions, as low as a few hundred of microns can be reached, for stereo angles of the order of a few hundred milliradians.

## 2.6    Systems for Particle Identification

Particle identification is of crucial importance in most experiments. The requirements can range from charged $\pi/K$ identification in B-physics channels like $B^0 \rightarrow D_s^\mp K^\pm$ against a background from $B^0 \rightarrow D_s^- \pi^+$ which is $\sim 15$ times more abundant, to $e/\pi$ separation at the level of $10^{-2}$ for momenta 1GeV/c. This task also will be important at ILC and at SuperB for lepton tagging $(\pi/\mu)$. The main types of detector and techniques used for particle identification besides calorimeters are:

- detectors based on the measurement of the energy loss by a charged particle in matter, $dE/dx$ (affected by landau fluctuations) or based on the number of ionization acts, $dN/dx$ (affected by Poisson fluctuations only);

- detectors based on the Cherenkov effect;

- detectors able to measure the time of flight of the particles;

- Transition Radiation Detectors.

## 2.7 PID by $dE/dx$ and $dN/dx$

The simultaneous measurement of the momentum of the particle and its mean energy loss, $dE/dx$ or number of ionization acts, $dN/dx$, can be used to estimate the mass of the particle. Because of the large Landau fluctuations in the measurement of $dE/dx$, many measurements are needed and a truncated mean of these measurements is used as an estimate.

In Fig. 2.7 the results obtained by the ALEPH TPC [28] in particle identification, using a truncated mean at 60%, are reported.

### 2.7.1 CLUster COUnting technique to measure $dN/dx$ and correlation between $dE/dx$ and $dN/dx$

A particle crossing the sensitive volume of a gaseous detector creates a number of electron-ion pairs along its path. At each interaction in the ionization act, the particle can liberate one or more electron-ion pairs, which we call one cluster, depending on the energy released. The distance between two consecutive clusters follows an exponential distribution of mean $\lambda$, which represents the mean free path of the particle between two consecutive interactions and the value of which depends on the medium and on the external field. As a consequence, the number of clusters follows Poisson statistics:

$$P(n, k) = \frac{n^k}{k!} e^{-n} \ , \quad n = \frac{L}{\lambda}$$

where $L$ is thickness of the crossed medium. Clearly $k$ is correlated to the energy lost by the crossing particle but it is not affected by the long tails in the $dE/dx$ distribution (landau fluctuations), being these absorbed in the fluctuations in the number of electron-ion pairs created in each ionization act.
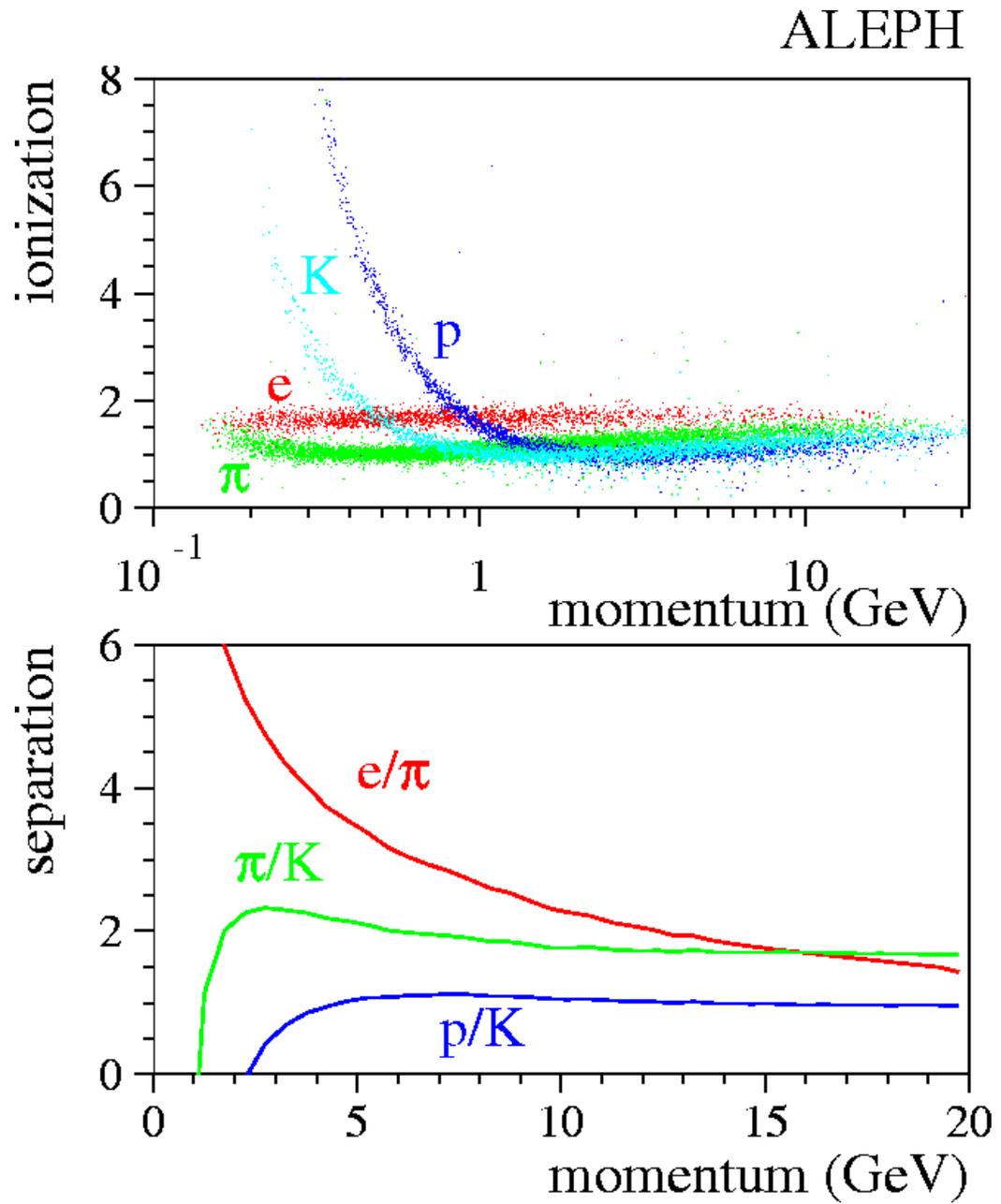
Figure 2.7: *PID performances of the ALEPH TPC.*

The method of the cluster counting consists in singling out, from every cell in a Drift Chamber, the isolated structures related to the arrival on the anode wire of the electrons belonging to single ionization acts. In order to achieve this goal, special experimental conditions must be met: pulses from electrons belonging to different clusters must have a small chance of overlapping in time and, at the same time, the time distance between pulses generated by electrons coming from the same cluster must be small, with respect to the time between two consecutive clusters, in order to prevent overcounting. The fulfilment of both these requirements involves incompatible time resolutions: it appears that the optimal counting condition can be reached only as a result of the equilibrium between the fluctuations of those processes which forbid a full cluster detection efficiency and of the ones enhancing the time separation among different ionization events.

A quality parameter, which allows to discriminate a primary ionization counting from a total energy loss measurement, can be defined as the ratio between the dispersion of the mean number of clusters and its square root: $\delta = \frac{\sigma}{\sqrt{<N>}}$. For an ideal counting, Poisson statistics imposes $\delta = 1$.

# Chapter 3

# Monte Carlo Studies for the CLUCOU Drift Cell

## 3.1  A Garfield based simulation

In this chapter the possibility to use the cluster counting technique on a drift chamber is investigated and algorithms are tested on simulated signals. To this aim, a MonteCarlo framework has been put up to simulate events from the ionization process to the signal generation, which is based on the computer codes Garfield [29], Magboltz [30] and HEED [31]. HEED simulates the interaction of the crossing particles with the gas mixture and computes the released energy. Magboltz solves the Boltzmann transport equations and computes the electron transport parameters. Garfield computes the electromagnetic field maps, electron and ion drift trajectories and arrival times on the anode and produces the signals. It runs a complete simulation, given the geometrical, electrical and physical parameters together with the gas mixture, the electrodes configuration and the high voltage. C++ programs and classes analyze the Garfield simulation results and test the algorithms by

using ROOT framework for data analysis [32].

### 3.1.1 Drift cell geometry and electrical characteristics

Drift tubes are selected for extensive study because of their favorable geometrical constraints and case of test against real experimental setup. In particular the performance of hexagonal cells for a central drift camber tracker are also examined. The hexagonal shape is the optimal arrangement in order to have a small amount of matter inside the drift chamber active volume and an electrostatic configuration which approximates at best that of a circular cell, Fig. 3.1. The diameter of the anode sense wire used in the simulation is 25 $\mu$m and the tube diameter 4 cm. For such a configuration the characteristic electrical parameters are, following the conventional notation of coaxial transmission line:

- capacitance per unit length   $\mathcal{C} = \frac{2\pi\epsilon_o}{ln(R_{tube}/R_{wire})} \simeq 7.5$ pF/m

- inductance per unit length   $\mathcal{L} = \frac{\mu_o}{2\pi}ln(R_{tube}/R_{wire}) \simeq 1.5$ $\mu$H/m

- impedance   $Z_0 = \sqrt{\frac{\mathcal{L}}{\mathcal{C}}} \simeq 440$ $\Omega$.

### 3.1.2 Choice of the Gas Mixture for the cluster counting application

The most typical gas mixture for gaseous detectors in high energy physics experiments is based on Argon, because of its low ionization potential, high drift velocity and low diffusion. The ionization potential (as low as 15.8 eV) guarantees that charges are easily and efficiently produced along the particle's trajectory, so that the output signal is large enough to be efficiently readout. The drift velocity, typically in the range of $\sim 3 - 7$ cm/$\mu$s, ensures
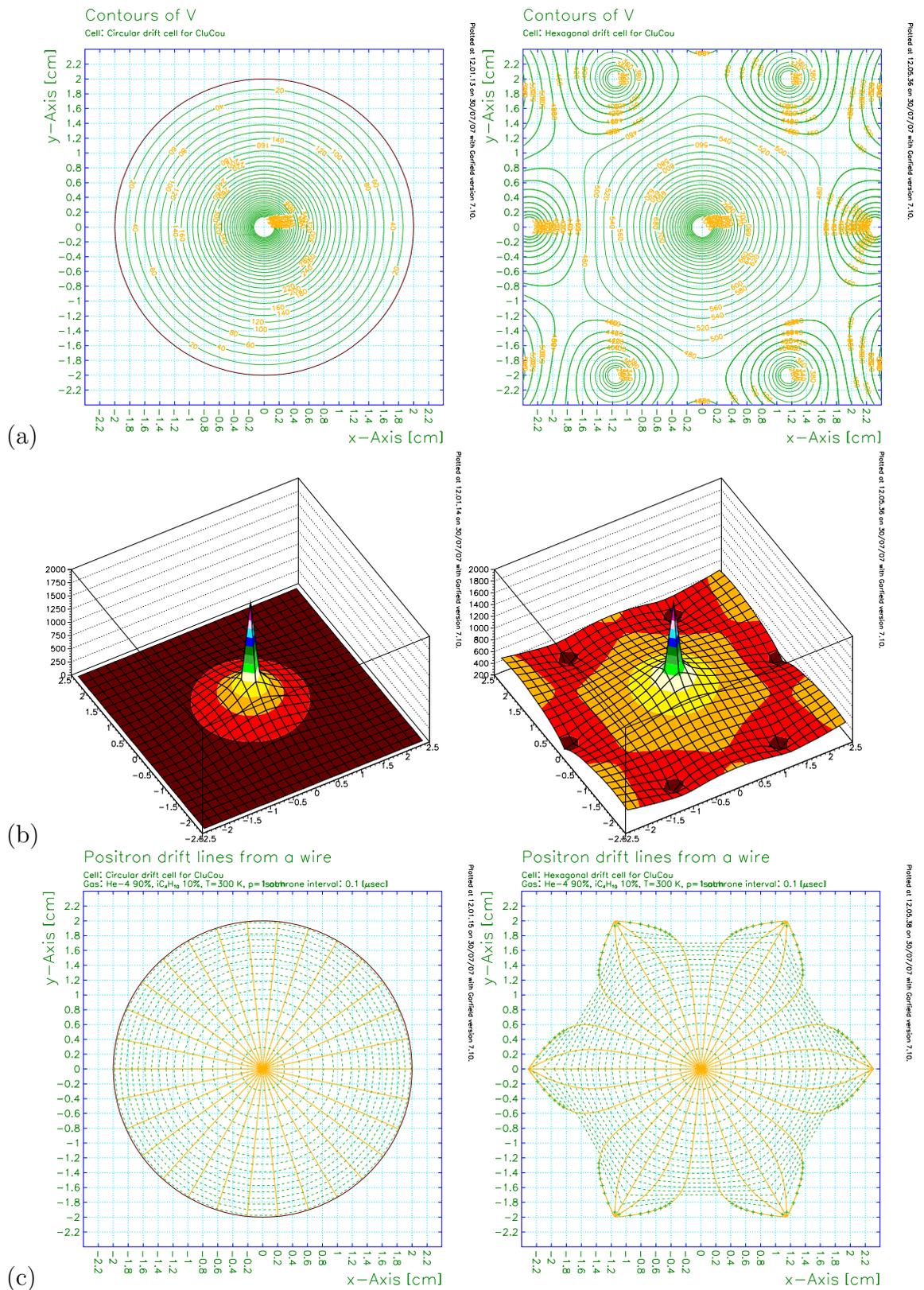
Figure 3.1: (a) *Equipotential lines,* (b) *Electrical potential configuration,* (c) *Isochrones for both circular (left) and hexagonal (right) drift cell.*
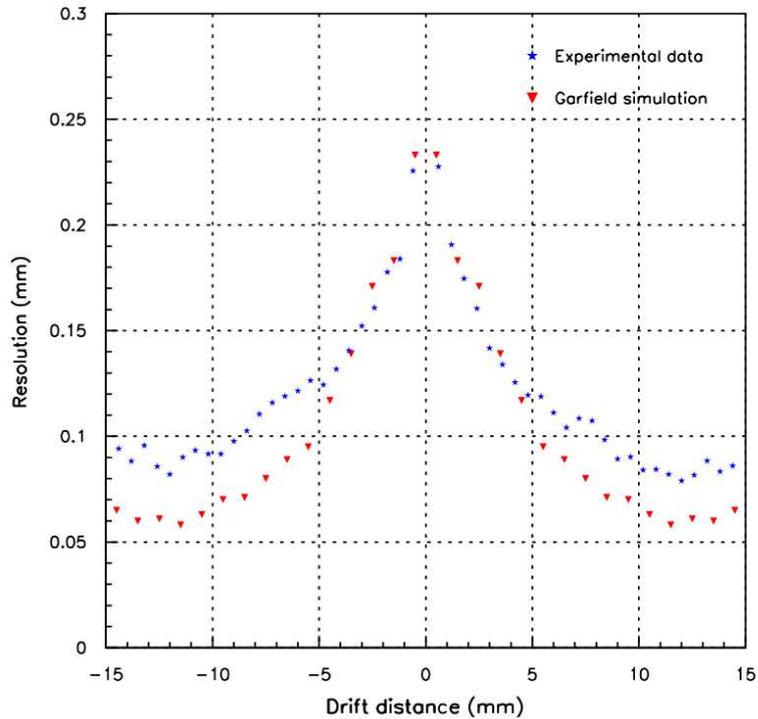
Figure 3.2: *Single ATLAS MDT tube resolution (mm) vs. impact parameter (mm) [33].*

a fast signal response. Diffusion, of $\sim$ 100-250 $\mu$m for a 1 cm drift path, does not affect spatial resolution dramatically. Up to-date Argon based gaseous detectors, like the ATLAS MDTs, reach a spatial resolution of 70 $\mu$m (Fig. 3.2) with a gas mixture of 93% Ar and 7% $CO_2$ at 3 bar [33]. A drawback, the short radiation length of Ar ($X_0 \simeq 115$ m at atmospheric pressure) makes the multiple scattering effect relevant for the track reconstruction precision. A drift chamber for central tracking, filled with Argon gas mixture would not be suitable for the future linear collider experiments. Moreover, the cluster counting technique would not be applicable, since, given copious ionization produced in Ar, the time between two consecutive clusters is too short to be resolved with the state of the art front-end electronics. The choice of
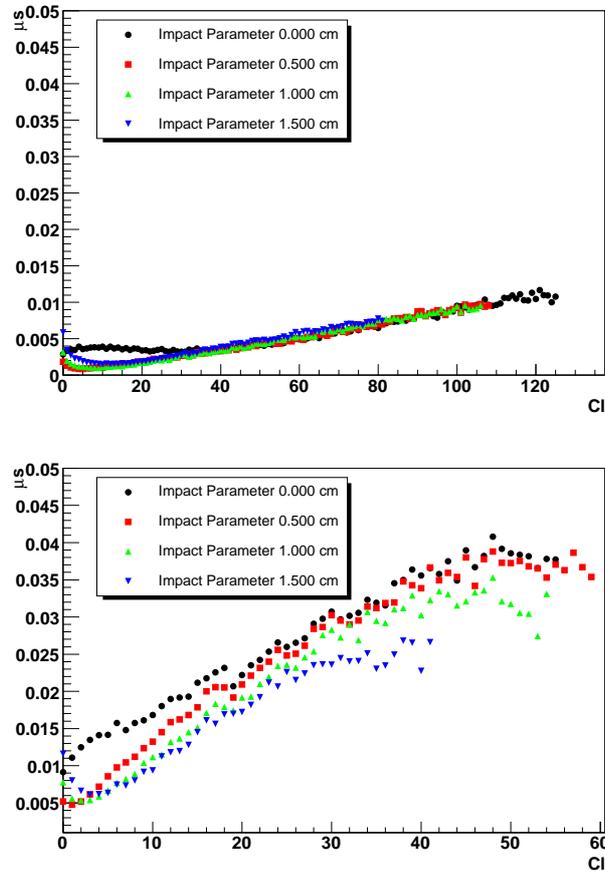
Figure 3.3: *(Garfield Simulated average delay between consecutive clusters, at different impact parameters, for a drift tube with radius = 2 cm, Wire Diameter = 25 μm, HV = 2000V. Up for the gas mixture Ar 93 %, $CO_2$ 7 % at 1 atm. Down for He 90 %, $C_4H_{10}$ 10 %.*
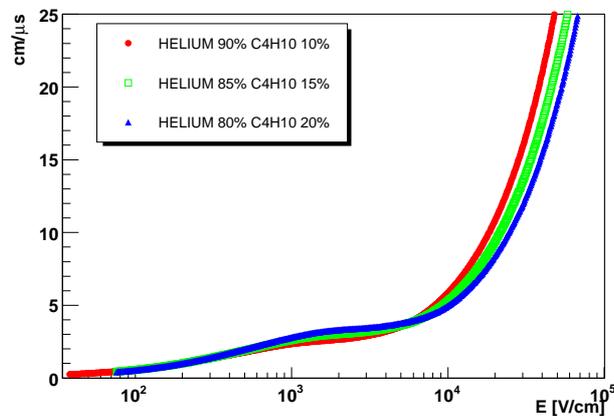


Figure 3.4: *Drift velocity as a function of the E-field for He-Isobutane mixtures as obtained by Magboltz.*
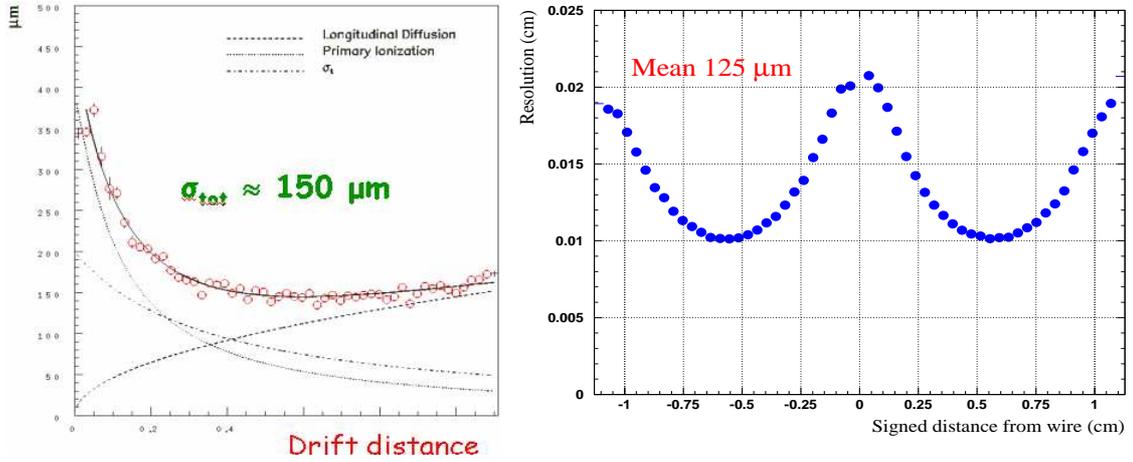
Figure 3.5: *Single cell resolution vs impact parameter, Left KLOE, Right BaBar.*

Helium is very advantageous, because of its large radiation length ($X_0 \sim$ 5500 m), which ensures a a much smaller contribution in terms of multiple scattering. In addition, its high ionization potential, 24.6 eV, is such that a crossing particle produces a small number of primary ions ($\sim$/cm). This, together with the lower value of drift velocity ($\sim$ 2 cm/$\mu$s) with respect to Ar, considerably helps the time separation between clusters (Fig. 3.3). A small amount of quencher gas (isobutane or DME) is necessary to avoid self-sustained discharge. 10% i-$C_4H_{10}$ is sufficient even though it raises the primary ionization to $\sim$ 13/cm and lowers the mixture $X_0$ to $\sim$ 1300 m. The fairly constant values of drift velocity in Helium based gas mixtures in a wide range of electric field (Fig. 3.4) assures a linear time-distance relation, up to a very close distances to the sense wire. Despite the higher electron diffusion in these gas mixtures, there are many examples of central Drift Chamber, like KLOE [34] and BaBar [35], that exhibit an average single cell resolution of the order of 120-150 $\mu$m (Fig. 3.5). Given for granted such spatial res-

olutions, which are obtained by timing only the first drifting electrons, one can aim at improving it by using the cluster counting technique by timing all arriving ionization clusters and, thus, reconstructing their distribution along the ionization track.

As a by-product of this technique, we'll be able to estimate also $dN/dx$ which, as we have seen in chapter 2, can give indication on the mass of the ionizing particle.

### 3.1.3 Gas mixture properties

In order to state our degree of control of the gas properties, all relevant parameters have been first evaluated by simulation.

Electron drift velocity, diffusion and multiplication coefficients have been calculated with the code Magboltz [30]. Magboltz theoretical computation of the drift velocity for the mixtures He-isobutane 90%-10%, 85%-15%, are consistent with experimental evidence [36] in the E/p range from 0 to 2.5 $Vcm^{-1}torr^{-1}$. However, this is only part of the reduced field range in our setup, which goes up to $\sim 300$ $Vcm^{-1}torr^{-1}$, on the sense wire surface, eventhough it represents the most relevant part of the range since the large contribution to the drift time comes from these low Electric field regions (Fig. 3.4).

The calculated values of diffusion are consistent with measurements from [37]. In this case at low Electric fields, the diffusion is larger than at high fields and, therefore, for a charge drifting large dinstances from the sense wire, the effect of the diffusion is correctly evaluated. From Magboltz (Fig. 3.6) one can calculate the diffusion as a function of the drift distance (Fig.
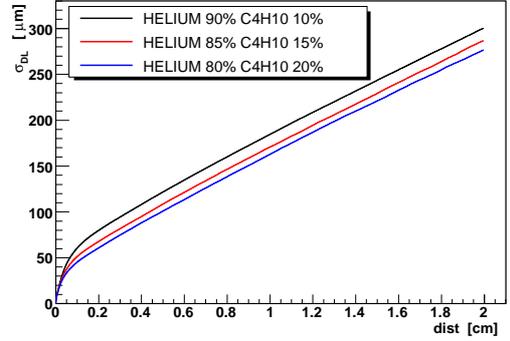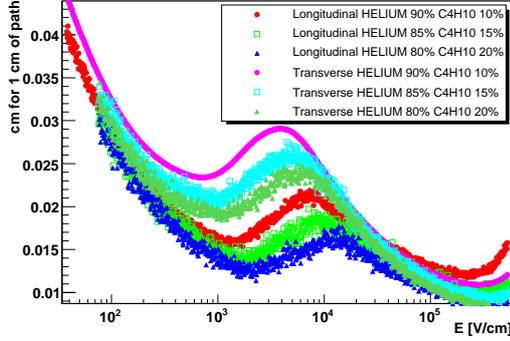
Figure 3.6: *Values of transverse and longitudinal diffusion coefficients calculated by Magboltz.*

Figure 3.7: $\sigma_{DL}$ *as a function of the drift distance from the sense wire.*

3.7) to the sense wire through an integration over the drift path:

$$\sigma_{DL}^2(r) = \sum_i \sigma_{DLi}^2 \ , \qquad \sigma_{DLi} = d(E_i) \cdot \Delta r_i$$

where $\Delta r_i$ is the elementary path over which the electric field $E_i$ is assumed to be constant. Fig. 3.7 shows the longitudinal diffusion as a function of the drift distance for all the examined gas mixtures.

By using Magboltz, the charge amplification as a function of $E$ can be calculated, through the estimate of the first Townsend ($\alpha$) and the attachment ($\eta$) coefficients. These two parameters define the amplification gain [38]:

$$G = \frac{n}{n_0} = e^{\int (\alpha(x) - \eta(x)) dx} \tag{3.1}$$

where $n$ is the number of electrons collected on the sense wire and $n_0$ is the number of primary electrons generating the multiplication process. The first Townsend coefficient $\alpha$ represents the number of ionization acts per unit length whereas the attachment coefficient $\eta$ is the number of electrons
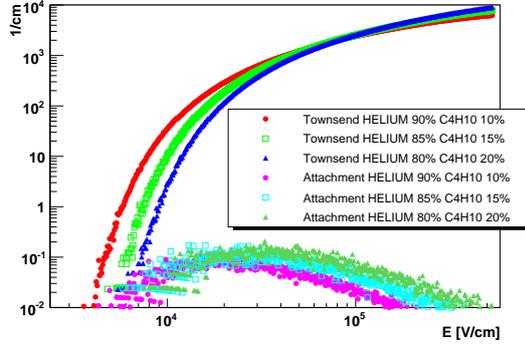
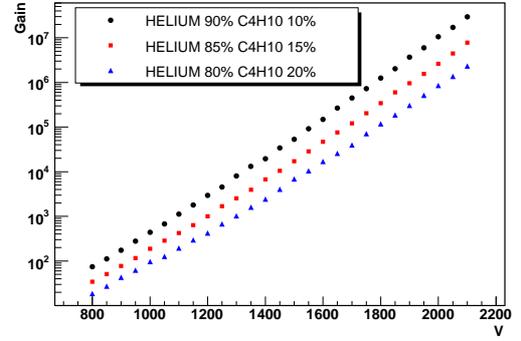Figure 3.8: *First Townsend and attachment coefficients computed by Magboltz.*

Figure 3.9: *Gain computed by Garfield for a drift tube (outer radius 2 cm, wire diameter 25 μm, at NTP) as a function of the sense wire voltage.*

which recombine with the gas positive ions per unit length. Results of the simulation of $\alpha$ and $\eta$ for several mixtures are displayed in Fig. 3.8. Gain calculations as a function of bias voltage of the drift tube under examination are shown in Fig. 3.9 for different gas mixtures. In order to check the consistency of the simulations with the experimental results, one can rely on semi-empirical formulae tested over a wide range of gas mixtures in literature [39, 38, 40]. Following [40] one can expand the Townsend coefficient in the form:

$$\frac{\alpha}{N} = \frac{eD}{\varepsilon_i} S \; e^{-\left(\frac{s_0}{S}\right)^{1+m}} \;, \quad S = \frac{E}{N} \tag{3.2}$$

where $\varepsilon_i$ is the first ionization potential, $D$, $S_0$ and $m$ are empirical constants related to the gas mixture. $N$ is the number density of atoms or molecules of the gas, defined in terms of the density $\rho(p, T)$ and the molar mass $P_{mole}$:

$$N = \rho_{mix}(p, T)\frac{N_A}{P_{mole}} \quad or \quad N = N_0\frac{p}{760}\frac{273}{T}$$

$N_A$ is the Avogadro number and $N_0$ is the Loschmidt number. $S$ is conveniently expressed in units of Td (1 Td=$10^{-17}$Vcm$^2$).

If recombination effects can be neglected, Eq. 3.2 plugged into Eq. 3.1 gives the gas gain for a proportional counter:

$$\frac{Ln(G)}{NaS_a} \simeq K \left\{ (1+m)Ln\left(\frac{S_a}{S_0}\right) + \frac{1}{1.1!}\left(\frac{S_0}{S_a}\right)^{1+m} - \frac{1}{2.2!}\left(\frac{S_0}{S_a}\right)^{2(1+m)} + \right. \\ \left. + \frac{1}{3.3!}\left(\frac{S_0}{S_a}\right)^{3(1+m)} \right\} - L \tag{3.3}$$

where $S_a$ is the reduced electric field on the wire surface and $K$ and $L$ are gas constants. Eq. 3.3 tested in the range of $S$, 70-565 Td, on He 90% isobutane 10% gas mixture, using m = 1/3, $K$ = 0.02496 V$^{-1}$, $S_0$=140 Td and $L$ = 1.713 · $10^{-5}$ V$^{-1}$ shows a good agreement with the experimental data. Comparison of the gain from Eq. 3.3 with the one calculated by Garfield, for the mixture He 90% i-$C_4H_{10}$ 10% at 25 °C and 1 atm in a drift tube with outer radius of 2 cm and wire diameter of 25 $\mu$m is illustrated in Fig. 3.10 in a wide range of high voltage.

Gas gain is affected by statistics (Fig. 3.11) through the Polya distribution function [39]:

$$P(n) = \frac{(1+\theta)}{\overline{n}\,\theta!}\left[\frac{n}{\overline{n}}(1+\theta)\right]^\theta e^{-\frac{n}{\overline{n}}(1+\theta)} \tag{3.4}$$

where $\overline{n}$ is the mean number of multiplied electrons, $\theta$ is a parameter that for drift tubes is 0.5 [41] and the variance of $n$ is $\sigma^2 = \overline{n}^2(1+\theta)^{-1}$.

A further check of this simulation refers to the mechanism by which the ionizing particles release their energy in the active gas producing ionization clusters of different multiplicity along their path. This is accomplished by Heed which simulates the ionization deposition accounting for all physical effects as primary ionization, photon emission and reabsorption generating new ion-electron pairs (Jesse [42] or Penning [38] effect). In addition, primary electrons may become $\delta$ rays if they have sufficient energy to ionize
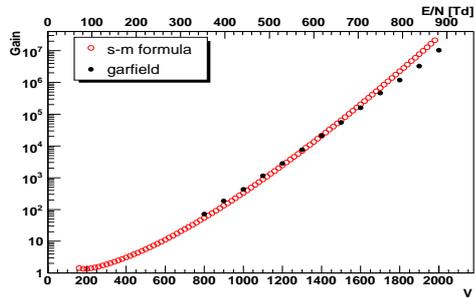
Figure 3.10: *Comparison of the gain obtained by Garfield and semi-microscopic model described in the text for the drift tube examined in this work.*
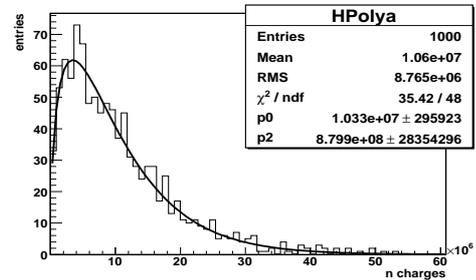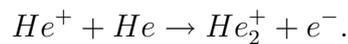
Figure 3.11: *Distribution of the single electron multiplication, simulated by Garfield, fitted with a Polya function.*

themeselves. Furthermore, an electron can be released when an ion and a neutral atom combine together in a molecule like in:

$$He^+ + He \rightarrow He_2^+ + e^-.$$

Results obtained by Heed for a 600 MeV/c muon in 90% He, 10% i-$C_4H_{10}$ gas mixtures are illustrated in Fig. 3.12 and 3.13.

Since single interactions are independent, the distribution of primary electrons is Poissonian, as shown in Fig. 3.12. The mean number of primary charges per unit length and the mean cluster population simulated by Heed are in fairly good agreement with those expected for minimum ionizing particles, as shown in Tab. 3.1. Note that the expected data are model dependent.

The positive ions drift in the gas with a much slower velocity than the electrons and their mobility, $\mu=v_{drift}/E$, depends almost linearly on the reduced field E/p. Since the mobility is not computed by Magboltz, we have
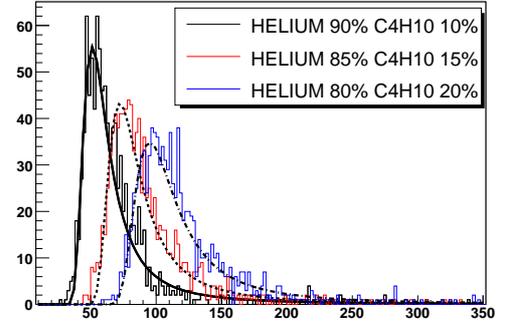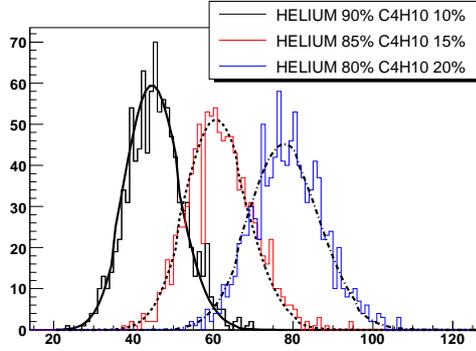
Figure 3.12: *Number of clusters as simulated in a 4cm gas layer superimposed with the Poisson distribution functions.*

Figure 3.13: *Number of total electrons as simulated in a 4cm gas layer fitted with Landau distribution functions.*

|  | 90%-10% | 85%-15% | 80%-20% |
|---|---|---|---|
| $\overline{n}_p/cm^{HEED}$ | 11.3 | 15.3 | 19.6 |
| $\overline{n}_p/cm^{exp}$ | 12.2 | 16.2 | 20.2 |
| $\overline{n}_t/\overline{n}_p^{HEED}$ | 1.60 | 1.62 | 1.62 |
| $\overline{n}_t/\overline{n}_p^{exp}$ | 2.2 | 2.2 | 2.2 |

Table 3.1: *Number of clusters and of electrons simulated by HEED and expectation values kept by [43] for HELIUM-ISOBUTANE mixtures.*

inserted its value in the simulation by using Blanc's law even though the data set available for the our gas mixtures is not complete. We have used the mobility of $He^+$ in He, $\mu_{He} = 10.4$ cm$^2$V$^{-1}$s$^{-1}$ [39, 43, 44], since it represents the upper limit for the selected mixtures and it is relevant for calculating the shape of the signal (see below) where the faster part of the signal is determined by the faster ions.

## 3.2 Development of the signal

The signal generated on the wire is induced by the motion of the free charges, electrons and ions, in the electrical field. Electrons produce a faster signal because the pulse shape depends on the velocity of the charge according to Shockley-Ramo theorem [45, 46]. However this signal is about 1% of that produced by the positive ions, for a drift tube with typical dimensions. As a consequence, the signal is mostly due to the positive ions which are produced during the avalanche process, when all of them start drifting to the wire surface [39, 43, 44]. An approximate expression for the resulting current is:

$$i(t) = -\frac{Q\mathcal{C}}{4\pi\epsilon_0}\frac{1}{t_0 + t} \quad, \quad 0 \leq t \leq t_{max} \tag{3.5}$$

where $Q$ is the ion total charge, $\mathcal{C}$ is the capacitance per unit length (as quoted in sec. 3.1.1) and:

$$t_0 = \frac{R_{wire}}{2\mu E(R_{wire})} \quad, \quad t_{max} = \int_{R_{wire}}^{R_{tube}}\frac{dr}{\mu E(r)} = \frac{R_{tube}^2 - R_{wire}^2}{2\mu V}ln\frac{R_{tube}}{R_{wire}}$$

$\mu$ is the ion mobility and the meanings of $R_{tube}$ and $R_{wire}$ are obvious. In the case under study here, with constant ion mobility assumption, we have $t_0 \simeq$ 0.3 ns and $t_{max} \simeq 700$ $\mu$s.

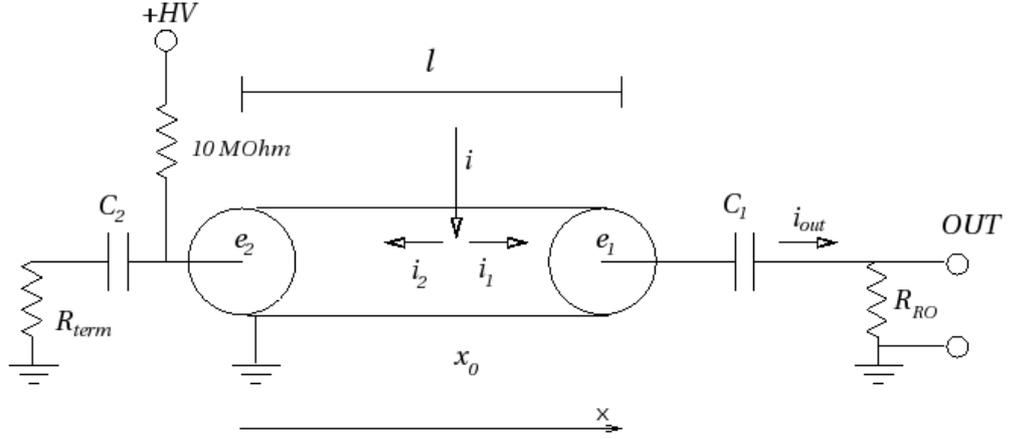In order to understand the signal read out after the propagation along the

Figure 3.14: *Schematic view of the Drift Tube instrumentation.*

drift tube, we follow the Fourier analysis approach from [47]. The drift tube propagates the signal as in a coaxial transmission line with distributed parameters like those in subsection 3.1.1 (Fig. 3.14). The impedance of this transmission line is dependent on the frequency:

$$Z_0(\omega) = \sqrt{\frac{\mathcal{L}}{\mathcal{C}} \left(1 + \frac{R(\omega)}{i\omega\mathcal{L}}\right)}$$

in which the conductance $\mathcal{G}$ of the gas is neglected, $\omega$ is the signal pulsation, $R(\omega)$ is the resistance per unit length of the sense wire and $\mathcal{L}$ is the inductance per unit length. The wire resistance is not constant (Fig. 3.15) because of the skin effect that can be modelled [47] by:

$$R(\omega) = \begin{cases} \frac{1}{\pi\sigma R_{wire}^2} + \frac{\sigma\mu_o^2 R_{wire}^2}{192\pi}\,\omega^2 & \omega < \frac{8}{R_{wire}^2 \sigma\mu_o} \\ \frac{1}{2\pi R_{wire}}\sqrt{\frac{\mu_o\,\omega}{2\sigma}} + \frac{1}{4\pi\sigma R_{wire}^2} + \frac{3}{32\pi R_{wire}^3}\sqrt{\frac{2}{\sigma^3\mu_o\omega}} & \omega \geq \frac{8}{R_{wire}^2 \sigma\mu_o} \end{cases}$$

where $\sigma$ is the conductance of the wire. The signal propagating inside a coaxial transmission line results from the super position of a direct wave, travelling from the generator to the load $R_{RO}$ (Fig. 3.14), and a reflected wave, travelling towards the generator. During the propagation, the two
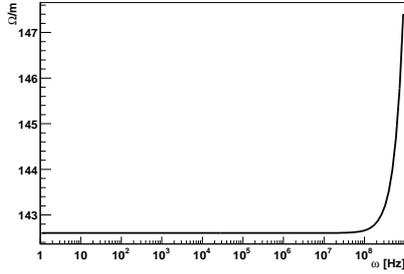
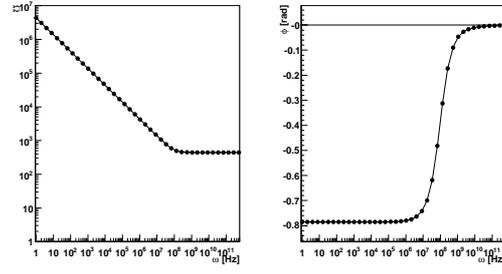Figure 3.15: *Resistance per unit length of the sense wire.*

Figure 3.16: *Modulus and phase of the drift tube impedance.*

components are modified by the propagators $T_d$ and $T_r$, respectively, which are functions of the distance traveled:

$$I(\Delta x) = I_d \ T_d(\Delta x) + I_r \ T_r(\Delta x)$$

$$T_d(\Delta x) = e^{-\gamma \Delta x} \ \ and \ \ T_r(\Delta x) = e^{\gamma \Delta x} \ \ , \ \ \ \gamma = \alpha(\omega) + ik(\omega)$$

$$\alpha(\omega) = \sqrt{\tfrac{1}{2}[\omega \mathcal{C} \sqrt{R^2(\omega) + \omega^2 \mathcal{L}^2} \ - \ \omega^2 \mathcal{L} \mathcal{C}]}$$
$$k(\omega) = \sqrt{\tfrac{1}{2}[\omega \mathcal{C} \sqrt{R^2(\omega) + \omega^2 \mathcal{L}^2} \ + \ \omega^2 \mathcal{L} \mathcal{C}]}$$

When the wave reaches the end of the line and meets a different impedance, a part is transmitted and a part is reflected back in the following ratio:

$$\rho^I = -\rho^V = \frac{Z_{line} - Z_{end}}{Z_{line} + Z_{end}} \ \ , \ \ \tau^I = 1 + \rho^I = \frac{2 Z_{line}}{Z_{line} + Z_{end}}$$

$\rho^I$ is the reflection coefficient and $\tau^I$ is the transmission coefficient for the electrical current wave, $\rho^V$ is the reflection coefficient for the voltage wave, notice that all of them are function of $\omega$.

A signal $i$ produced at $x_0$ in the drift tube of length $l$ is split in to two equal parts, ($i_1$ and $i_2$) going in opposite directions as in Fig. 3.14. When they

have reached the ends, $e_1$, $e_2$, waves are produced which move back and forth along the line. As a consequence, the signal transfer function for the $i_{out}$ portion produced by $i_1$ is:

$$\Psi'(\omega) = \tfrac{1}{2}\, \tau_1^I T_d(l - x_0) \ + \ \tfrac{1}{2}\, \tau_1^I T_d(l)\rho_2^I T_r(-l)\rho_1^I T_d(l - x_0) \ +$$
$$+ \ \tfrac{1}{2}\, \tau_1^I T_d(l)\rho_2^I T_r(-l)\rho_1^I T_d(l)\rho_2^I T_r(-l)\rho_1^I T_d(l - x_0) + ...$$

and for that produced by $i_2$ is:

$$\Psi''(\omega) = -1 \left( \tfrac{1}{2}\, \tau_1^I T_d(l)\rho_2^I T_r(-x_0) \ + \ \tfrac{1}{2}\, \tau_1^I T_d(l)\rho_2^I T_r(-l)\rho_1^I T_d(l)\rho_2^I T_r(-x_0) \ + \right.$$
$$\left. + \ \tfrac{1}{2}\, \tau_1^I T_d(l)\rho_2^I T_r(-l)\rho_1^I T_d(l)\rho_2^I T_r(-l)\rho_1^I T_d(l)\rho_2^I T_r(-x_0) + ... \right)$$

notice the minus sign since $i_2$ flows in the opposite direction as $i_1$. These functions represent infinite geometric series, which, after summing, result in the total transfer function:

$$\Psi(\omega) = \Psi'(\omega) + \Psi''(\omega) = \tfrac{1}{2}\tau_1^I \, \frac{T_d(l-x_0) \ - \ \rho_2^I T_d(l+x_0)}{1-\rho_1^I\rho_2^I T_d(2l)} =$$
$$= \tfrac{1}{2}\tau_1^I \, T_d(l - x_0)\frac{1- \ \rho_2^I T_d(2x_0)}{1-\rho_1^I\rho_2^I T_d(2l)} \tag{3.6}$$

and its modulation effects are represented in Fig. 3.17.

In the plot we can distinguish four frequency domains:

- for $\omega < 10^3$ Hz all the charge goes out in the HV resistor;

- in the range $10^3$ Hz $< \omega < 10^7$ Hz the capacitors $C_1$ and $C_2$ are the principal components and we have a plateau at $\frac{C_1}{C_1+C_2} = 0.5$;

- between $10^7$ Hz and $10^{10}$ Hz the resistors $R_{RO}$ and $R_{term}$ are the principal components, there is a plateau at $\sim \ 1-\frac{R_1}{R_2} = 0.89$ with distortions due to the dependence of the termination resistance on the frequency;

- frequencies $\omega > 10^{10}$ Hz are strongly attenuated.

The shape of the phase for $\omega > 10^9$ Hz is oscillating because the drift tube becomes a resonant cavity for the waves with $\omega = n\frac{2\pi}{l}$.
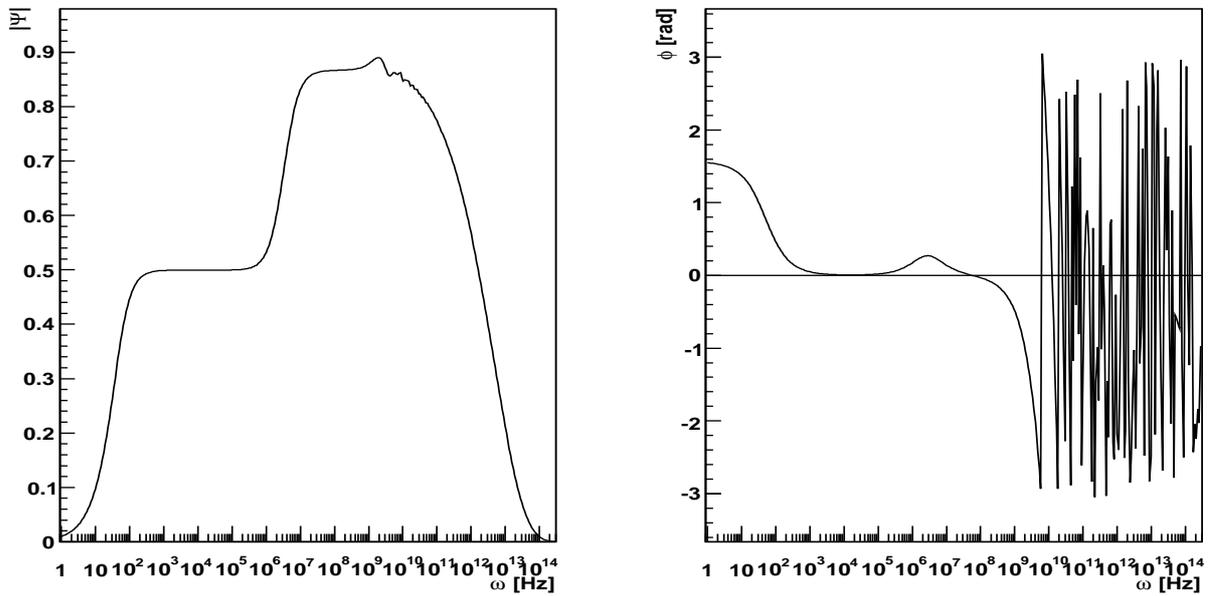
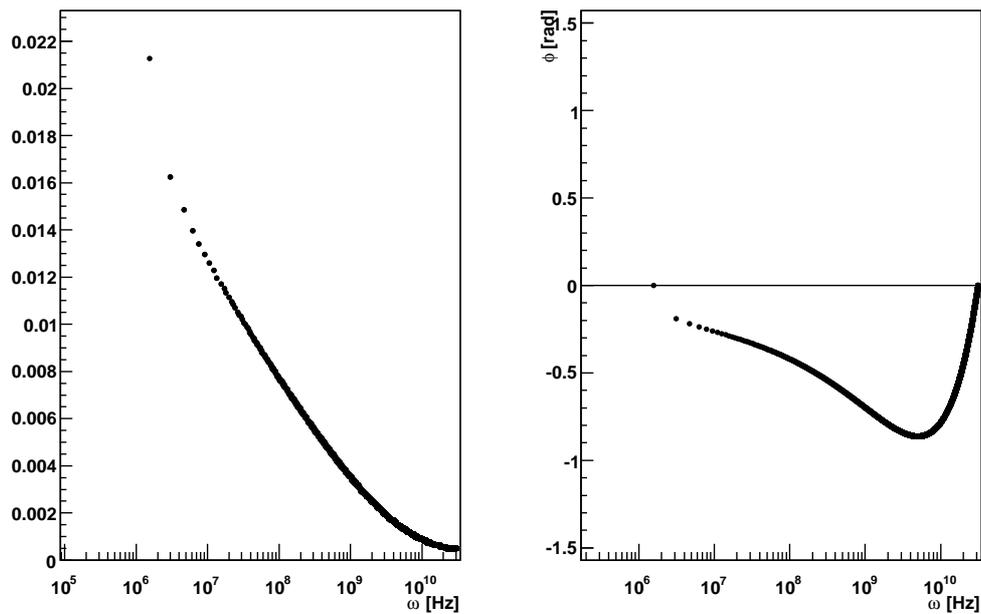Figure 3.17: *Modulus (left) and phase (right) of the current transfer function.*



Figure 3.18: *Frequency spectrum of avalanche signal.*

The readout current signal is obtained in the frequencies domain by multiplying the transfer function by the Fourier transform of the signal $i$, its frequency spectrum is reported in Fig. 3.18:

$$\tilde{i}_{out}(\omega) = \Psi(\omega)\tilde{i}(\omega) \ , \quad \tilde{i}(\omega) = \frac{1}{\sqrt{2\pi}} \int_{-\infty}^{\infty} i(t)e^{-i\omega t}dt$$

which can be inverted to obtain the readout current signal. It is important to note that the expression of the transfer function (Eq. 3.6) depends on the instrumentation setup but also on the length of the drift tube ($l$) and on the position of the pulse along it ($x_0$).

Using a discrete Fast Fourier Transformation program, FFTW [48] interfaced to Root, we have evaluated the drift tube propagation shaping for a pulse induced by $10^7$ charges and generated in the middle of a 30 cm long drift tube. In Fig. 3.19 we show the shaping effect with $C_1 = C_2 = 1$ nF, $R_{RO} = 50$ $\Omega$, $R_{term} = \sqrt{\mathcal{L}/\mathcal{C}}$ and we can see how the read-out pulse peak is shifted 0.5 ns and its height is $\sim 86\%$ of the generated one.

By means of the Fourier analysis the read out signal evaluation can be completed by including also the transfer function of the front-end electronics (preamplifier, shaper).

Let us focus on the case of an oscilloscope probe which can be represented by an RC circuit with R = 20 K$\Omega$ and C = 0.85 pF, thus getting the output signal of Fig. 3.21. In this case the mean signal peak height is of $\sim$ -13 mV and its time shift is $\sim$ 0.6 ns.

In order to estimate the minimum readable signal and to tune the electronics noise as best as possible we must account for the fluctuations of the Polya distribution of the gain. The integral of such a distribution, from the threshold $n_{threshold}$ to $+\infty$ gives the probability of having a signal larger than the threshold. By using the numerical values reported in Fig. 3.11 we get the following table, which, besides this probability, quotes also the values of cur-
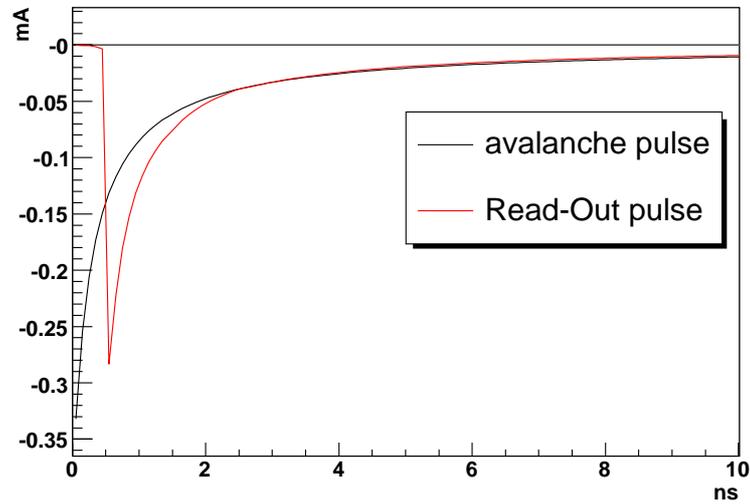
Figure 3.19: *Avalanche signal as generated and after propagation to the read-out pin.*
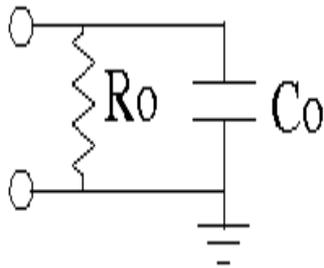




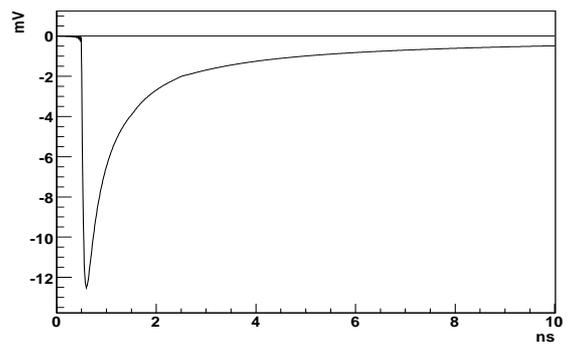Figure 3.20: *Simple scheme of an oscilloscope probe.*

Figure 3.21: *Avalanche Signal seen by $C_0$.*

Table 3.2:

| $n_{threshold}$ | prob. % | time bin 400ps | |
| --- | --- | --- | --- |
| | | $\sim$ mA | $\sim$ mV |
| $10^5$ | 99.8 | -0.0016 | -0.081 |
| $2.5 \cdot 10^5$ | 99.4 | -0.0041 | -0.202 |
| $5 \cdot 10^5$ | 98.5 | -0.0082 | -0.404 |
| $7.5 \cdot 10^5$ | 97.4 | -0.0123 | -0.607 |
| $10^6$ | 96.1 | -0.0164 | -0.809 |
| $2.5 \cdot 10^6$ | 86.6 | -0.0410 | -2.022 |

rent and pulse height for each threshold, for a signal sampling rate of 2.5 GSa/s.

The electronic convolution algorithm has been tested using the PSpice program [49, 50], a general-purpose circuit simulation program for nonlinear dc, nonlinear transient, and linear ac analysis. The simulation of the signal generated at $x_0$ distance from one end of the tube has been done by propagating the current to both sides of the wire as through two transmission lines (Fig. 3.22). Fig. 3.23 shows the excellent agreement between the simulation of a single peak signal made by the convolution algorithm just described and its PSpice treatment, in the case in which the termination resistance $R_{term}$ ( = 100 $\Omega$) is different from the drift tube impedance ($\sim$ 440 $\Omega$). Small discrepancies between the two simulations are due to the fact that in the case of PSpice the skin depth effect is neglected, whereas for the convolution simulation it is taken into account.
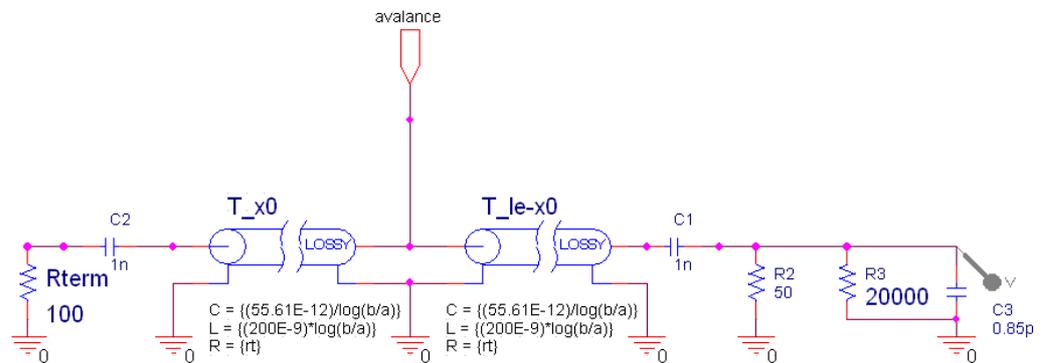
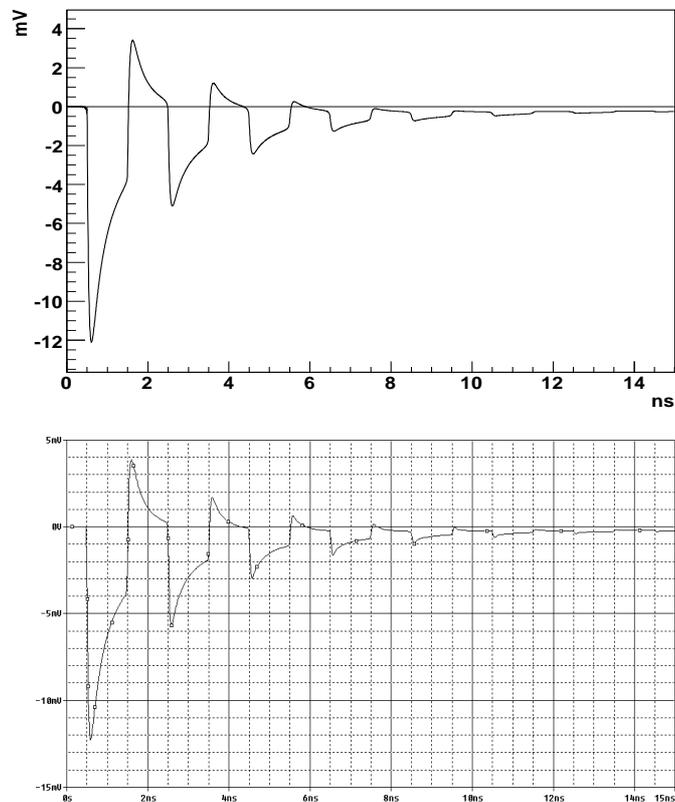Figure 3.22: *Schematic of the circuit for the PSpice simulation.*



Figure 3.23: *Single peak signal as simulated by: (up) the convolution algorithm, (down) PSpice program.*

## 3.3 The algorithm to count ionization clusters

Applying the convolution algorithm described in the previous paragraph on the whole sequence of clusters generated by a crossing particle in the drift tube, we can reproduce the expected signal. From Fig. 3.24 it is clear that the identification of every single structure produced in the signal by the drifting electrons is not a simple task. To reach this goal, we have to elaborated a peak finding algorithm based on the following statements:

- the rise and falling time of an elementary pulse are constant and depend only an the experimental set up. They need to be measured;

- the variance of the Gaussian noise, $\sigma_{noise}$, again function of the experimental set up can be measured in absence of signal, i.e. by using the digitized bins of the signal just before the trigger;

- a set of bins is a candidate peak if, over an interval equivalent to the rise time, it presents a rising pulse height larger than $6\sigma_{noise}$ with respect to the previous set of bins;

- a candidate peak is promoted if, over an interval equivalent to the falling time, it presents a falling pulse height larger than $6\sigma_{noise}$ with respect to the following set of bins.

- a set of peaks is grouped into a cluster if their relative delays are consistent with the spread in the electron diffusion for their average drift distance;

- sets of peaks are separated in different clusters if their average distance is consistent with the mean cluster separation for that particular impact
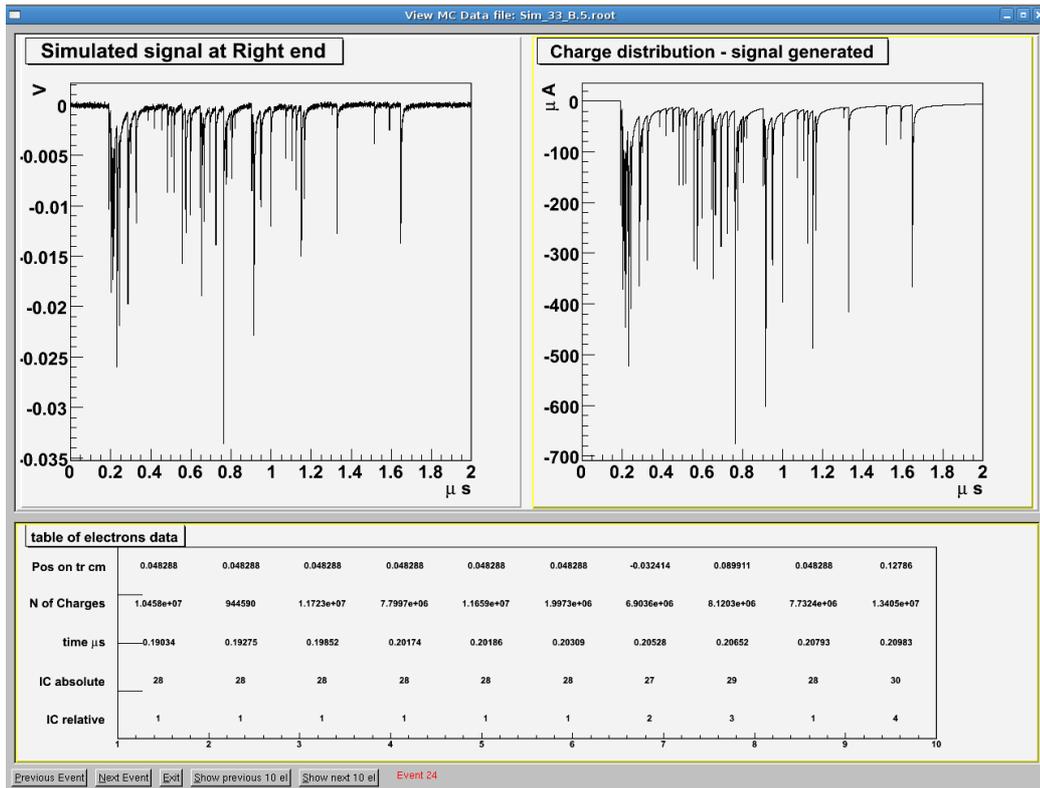
Figure 3.24: *Simulated signal. (left up) convoluted with noise; (right up) before the convolution; (down) ordered time sequence of the drifting electrons with the indication of the cluster position (**Pos on tr**) and ordering number (**IC absolute**) along the track and according to the arrival time (**time**) on the sense wire (**IC relative**). The amplification factor (**N of Charges**) in term of electrons is also indicated*

parameter and their average drift distance.

The results obtained by applying this algorithm to the signal of Fig. 3.24 are shown in Fig. 3.25, where a detail of the signal is reported. It is important to notice that a peak can hide more than a single electron if two or more electrons reach the wire with a time spread shorter than the electronics time resolution. In Fig. 3.26 we report the counting efficiency obtained in case of noiseless signals and for a Gaussian noise of $\sigma_{noise} = 0.14$ mV. For the first case we have almost full efficiency which decreases to 94% when the described noise is present. The inefficiency is consistent with the probability, due to the Polya fluctuations, that the single electron pulse height be lower that $6\sigma_{noise}$.

This makes the number of peaks smaller than the number of drifting electrons, eventhough it is larger than the number of clusters, as shown by the plot in Fig. 3.27. This can be corrected by applying the final steps of the algorithm as described.

## 3.4 The algorithm to increase the spatial resolution

As a result of the application of the cluster counting algorithm just described, or get, for each signal the ordered sequence of the electron arrival times $\{t_j\}$ (drift distances $\{d_j\}$ through the $x - t$ relation) $(j = 1, N_{ele})$ and that of the associated clusters $\{t_i\}$ (and $\{d_i\}$) $(i = 1, N_{cl})$, where $N_{cl}$ is the number of clusters. A better spatial resolution on the impact parameter can be reached by using an analysis based on the following statements:

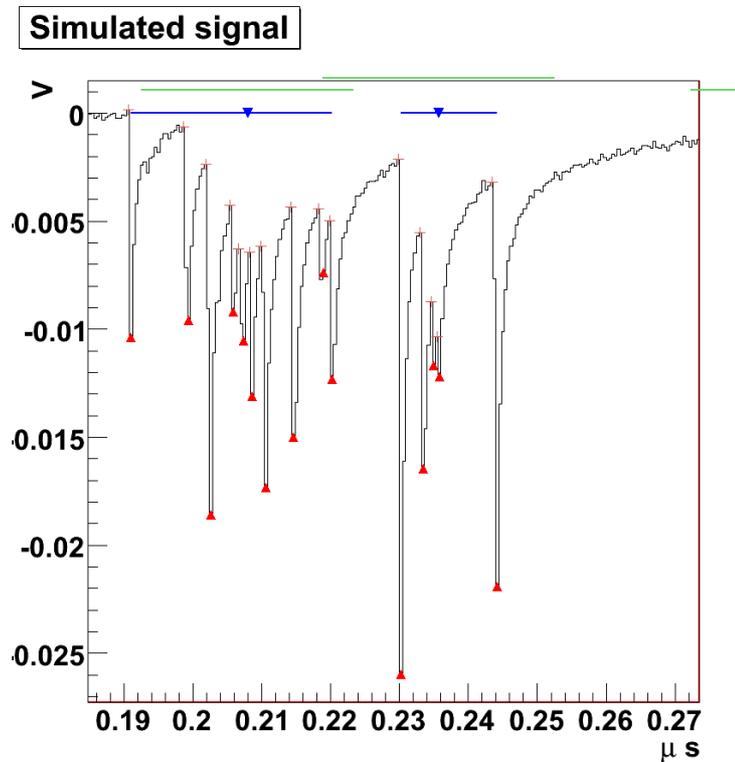- using simple geometrical consideration, see Fig. 3.28, each cluster can

Figure 3.25: *Detail of the region of high peak density at the onset of the simulated signal of Fig. 3.24. The triangular and the cross-shaped red markers represent, respectively, the peak positions and the start of the rise time, as found by the peak finding algorithm. The triangular blue markers and the blue bars indicate the cluster positions and the range over which the peaks are arranged into a cluster by the algorithm. The green lines extend over $6\sigma$ times the time diffusion of the identified clusters.*
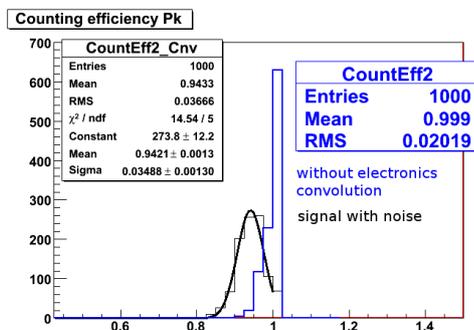


Figure 3.26: *Efficiency of the peak finding algorithm for noiseless signals, blue, and for signal with Gaussian noise ($\sigma_{noise} = 0.14$ mV), black.*
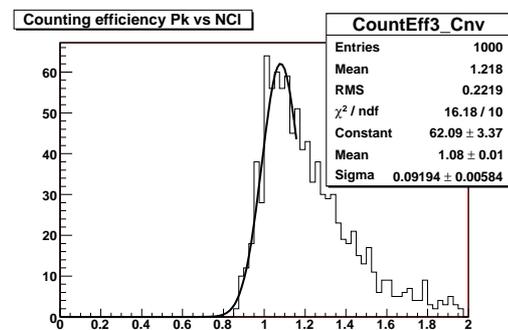
Figure 3.27: *Ratio between the number of counted peaks and the number of clusters.*
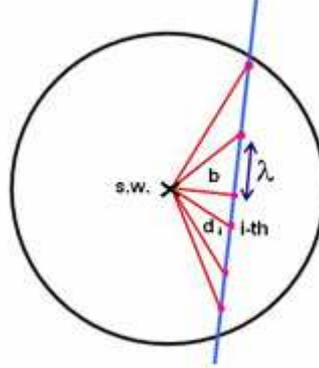
Figure 3.28: *Schematic view of the clusters distribution along a ionizing track. b is the impact parameter, $\lambda$ is the average clusters distance and $d_i$ is the single cluster distance from the sense wire.*

give an independent estimate of the impact parameter $b_i$ by:

$$b_i = \sqrt{d_i^2 - (i\lambda)^2}.$$

A weighted average can thus be calculated;

- one can assign a probability $P_i^{N_{cl}}(x)$ to the $i - th$ cluster to be located at position $x$ along the track. Following [44], the space distribution function of the clusters created along a track can be written as:

$$D_i^{N_{cl}}(x) = \frac{N_{cl}!}{(N_{cl} - i)!(i - 1)!}(1 - x)^{N_{cl}-i}x^{i-1}$$

where $N_{cl}$ is the total number of clusters in the event, $i$ is the generic cluster and $x$ is its position along the track normalized between 0 and 1. The probability that the $i - th$ cluster is produced at the distance $x_i$ is obtained by integration:

$$P_i^{N_{cl}}(x_i) = \int_{x_i-3\sigma_i}^{x_i+3\sigma_i} D_i^{N_{cl}}(x)dx$$

Here $x_i$ is a function of the impact parameter $b$, if expressed through the drift distance $d_i$ and the drift cell radius $R$, $x_i = \frac{\sqrt{d_i^2 - b^2}}{\sqrt{R^2 - b^2}}$); $\sigma_i$ depends on the cluster diffusion and on the time resolution. The best estimate for the impact parameter is then obtained by maximizing the likelihood function $\mathcal{L}(b) = \prod_{i=1}^{N_{cl}} P_i^{N_{cl}}(x_i)$, thus minimizing the statistical uncertainty on the position resolution.

## 3.5  PID performance

The number of clusters produced in the gas depends on the ionizing particle and on its energy, and fluctuates according to Poisson statistics how we have seen in section 2.7.1. Particle discrimination can therefore be achieved by counting the number of clusters [51, 52]. The uncertainty on this discrimination can be quoted as $\frac{\sigma(dN/dx)}{dN/dx} = \frac{\sqrt{N}}{N}$. In a drift chamber with a radius of $\sim 1.5$ m filled with helium based gas mixtures a particle can produce $\sim 2000$ clusters along the track, thus yielding a resolution $\frac{\sigma(dN/dx)}{dN/dx} \approx 2.2\%$.

# Chapter 4

# Experimental Studies for the CLUCOU Drift Tube

## 4.1 The experimental setup

We have built an experimental setup to study the characteristics of drift tubes against the Montecarlo simulations discussed in the previous chapter and to analyze the requirements for a front-end electronics to be used for cluster counting applications.

A description of the experimental setup follows:

- the trigger system. A set of three scintillators equipped with Hamamatsu H1949 photomultiplier tubes is used to define the timing of a passing cosmic ray. The first two scintillators, 1 cm thick, placed immediately before and after the Si telescope (see below), at the center of which the test drift tube is inserted, are optimized for time measurement whereas, the third one, 2.5 cm thick, is used for amplitude measurements, in order to select cosmic rays of different energies.

  Between the second and third scintillators, an iron absorber, of variable

thickness (up to 50 cm) can be used to cut low momentum cosmic rays which suffer from a large multiple Coulomb scattering contribution to the uncertainty in their extrapolation to the drift tube (Fig. 4.1);

- the tracking telescope. A telescope for a precise 3d track reconstruction, made of six planes of silicon detector, three upstream and three downstream of the drift tube is placed between the first two trigger scintillators (Fig. 4.1). The mechanical support of each silicon detector plane can rotate in steps of $1.2°$ azimuthally. The telescope can be easily upgraded by inserting more planes to achieve a better tracking resolution. These detectors have not been used in the measurements described below because of the long and complex procedure needed for their calibration which is still in progress;

- the gas system. Up to four different gas lines equipped with dedicated mass flow meters (MKS 1179A[1]) monitored by a digital controller (MKS Multi Gas Controller 647B) can be mixed together to supply several drift tubes. The temperature of the gas mixture is monitored with a pt100 thermoresistance.

- the ambient parameters monitor. The ambient temperature, the relative (input to the drift tube minus output) and the absolute pressure are continuously monitored with two TEKKAL SAT 750 and a MKS BARATRON 122A and a temperature sensor inserted in the National Instruments SCB-100 box connection.

- the HV system. The drift tube sense wires are kept at positive high voltage with respect to the tube wall by a CAEN SY127 HV power

---

[1]Each mass flow meter is accurately calibrated for a particular gas, although correction factors for any other gas can be applied directly by the digital controller.
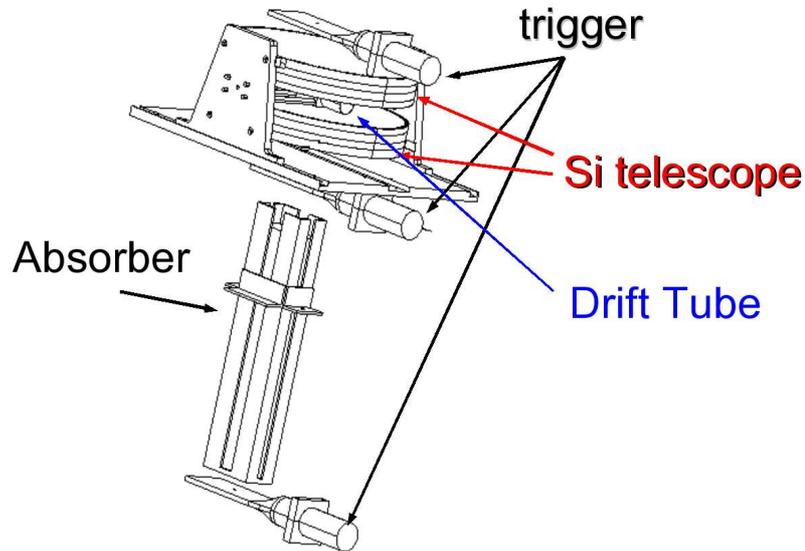
Figure 4.1:  *Scheme of the setup with a silicon telescope.*

supply.

- the read-out system. The drift tube signals, after a preamplifier, are read out by a digital oscilloscope (Tektronix TDS7404) with bandwidth of 4 GHz [2] and maximum acquisition rate of 20 GSa/s.

### 4.1.1   The Drift Tube prototypes

Two different drift tube have been studied. Both are 30 cm long with gold plated tungsten sense wires, 25 $\mu$m diameter. They are made of 1 mm thick copper of 2 cm and 1.4 cm radius. The first one is connected through a CR circuit (C = 1 nF, R = 50 $\Omega$) to the oscilloscope with an active probe (Tektronix P7240). For the second tube we have used a fast preamplifier,

---

[2]This bandwith limit is enough to see the almost part of a drift tube signal how can be seen from Fig. 3.17.
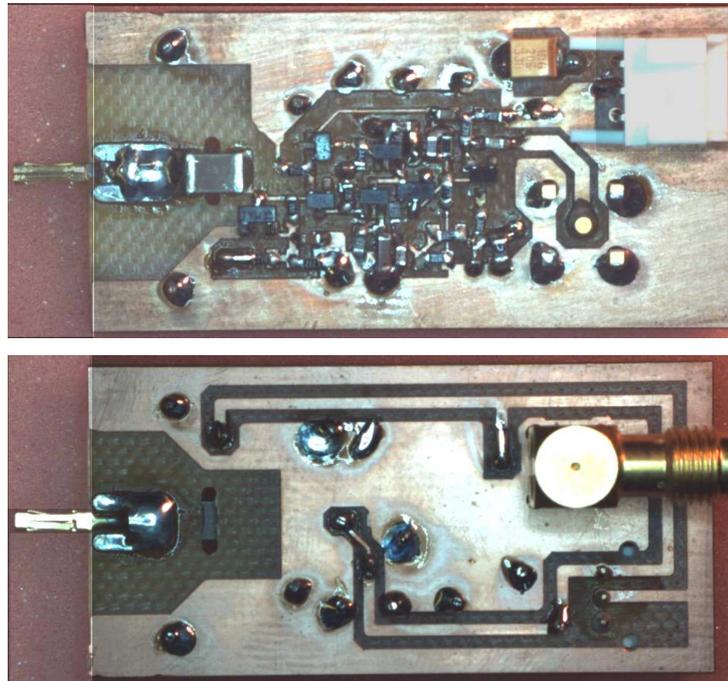
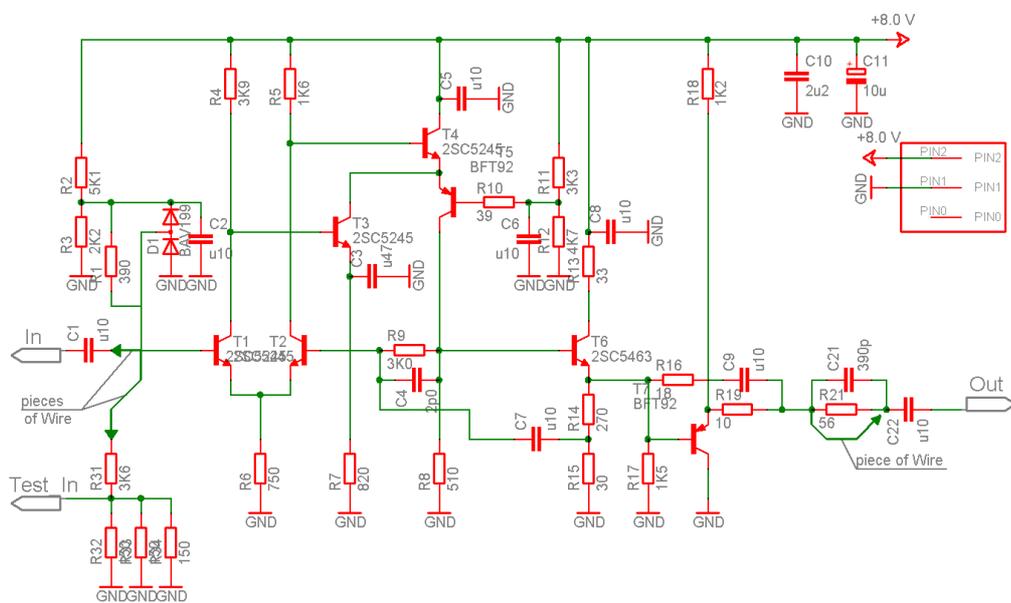Figure 4.2: *Pictures of both sides of the fast amplifier used for the drift tube with radius of 1.4 cm.*



Figure 4.3: *Schematic of the fast amplifier used for the drift tube with radius of 1.4 cm.*

designed by the Lecce INFN electronics laboratory, with 500 MHz bandwith and a gain of $\sim 7$, connected to the oscilloscope by a SMA transmission line and equipped with a tail cancellation circuit (Fig. 4.2, 4.3). The other ends of the tubes are connected to ground through their characteristic impedance. To prevent radiofrequency pick up, the readout circuits are enclosed in a Faraday cage. The sense wire voltage was set at 2000 V for the larger tube and 1750 V for the smaller one.

### 4.1.2   A silicon telescope

The silicon detectors are the CDF prototype designed for the Run IIb upgrade at the Fermilab Tevatron [53]. Each module covers a surface of 4x18 $cm^2$ and contains two silicon micro strip detectors with a thickness of 320 $\mu$m and a readout pitch of 75 $\mu$m. With this telescope we expect to be able to measure the impact parameter of the crossing cosmic ray within the drift tube with a precision of $\sigma \sim \frac{75}{\sqrt{12}} \cdot \frac{1}{\sqrt{4}} \sim 10$ $\mu$m.

### 4.1.3   The DCS and the DAQ systems

The Detector Control System and the Data Acquisition system have make use of a PC, with Windows OS, interfaced to the HV power supply CAEN SY127 and to the MKS Multi Gas Controller 647B by RS232 connections and to the digital oscilloscope Tektronix TDS7404 using a LAN communication. The PC is equipped with 16 channels Analog to Digital Converter (ADC) (National Instruments PCI 6033E) and 16 channels Digital to Analog Converter (DAC) (National Instruments PCI 6704). The ADC and the DAC board are equipped with connection boards, respectively, a SCB-100 and a SCB-68. The DAC is used to supply the power for the pt100 and to generate

a TTL kill signal to the HV in case of a problem in the gas mixture. The ADC is used to read out the signals of the temperature and pressure sensors. On the PC, three different software programs, written with the graphic language programming tool National Instruments Labview (v. 6.1), run continuously.

The first programs allows for an easy setting of the desired gas mixture and continuously monitor the real gases flow rates. It is responsible for generating a kill signal for the HV system if a monitored gas parameter exits from the selected range.

The second program reads the ambient temperature and pressure, the gas temperature and communicates with the HV power supply. For each HV channel used, to supply the drift tubes and the trigger scintillators, it reads the instantaneous values of voltage and current. This program communicates also with the DAQ and during a run every 100 events writes all the monitored parameters in a MySQL database.

The DAQ program is dedicated to read from the oscilloscope the events data and to write output files. In addition, it stores in a MySQL database a complete series of relevant parameters for a run.

## 4.2 Results

The described setup has been used to check the predictions made with the Montecarlo presented in the previous chapter.

The drift tubes signals have been sampled at 2.5 GSa/s in a time window of 4 $\mu$s. The time window is larger than the maximum drift time expected because the trigger signal has a time delay, due to the electronics, with respect to a signal of a drift tube generated by a crossing particle with impact parameter

close to 0. To avoid signal loss the trigger signal has been shifted in time by 1.6 $\mu$s.

The signals of the drift tubes (Fig. 4.4) can be directly compared with those simulated (Fig.3.24):

- the pulse height and the shape of a single electron for the 2.0 cm tube is very similar to the one obtained by the simulation. This implies that the gain factor computed by Garfield, the ion mobility and the convolution algorithm used are well under control. Any discrepancy between the two shapes may be due to the fact that the simulation takes into account the mobility of the ions in the gas and assumes a constant value, independent of the E-field, whereas, the real pulse gets a contribution from the mobility of the i-$C_4H_{10}$ ions in the gas, which has a value dependent on the E-field;

- using the peak finding algorithm, we have, from Fig. 4.5, that the maximum drift time for this tube is $\sim 1.7$ $\mu$s, in agreement with the one simulated of 1.62 $\mu$s (the variance due to the diffusion is 30 ns).

This signal shows that the electronics noise, in this case, is too high to measure efficiently each single electron peak. As a consequence, a fast preamplifier and a filter are necessary to increase the signal to noise ratio.

Let us, now, discuss the impact of the limited bandwith of the fast preamplifier on the possibility to measure the single electron peaks. In a first approximation, the transfer function of the preamplifier has been assumed equal to a step function so that all the signal component frequencies larger 500 MHz are cut. Using this transfer function in the convolution process based on Fourier analysis and including the gain factor effect, we have obtained the convoluted simulated signal shown in the left upper picture of Fig.
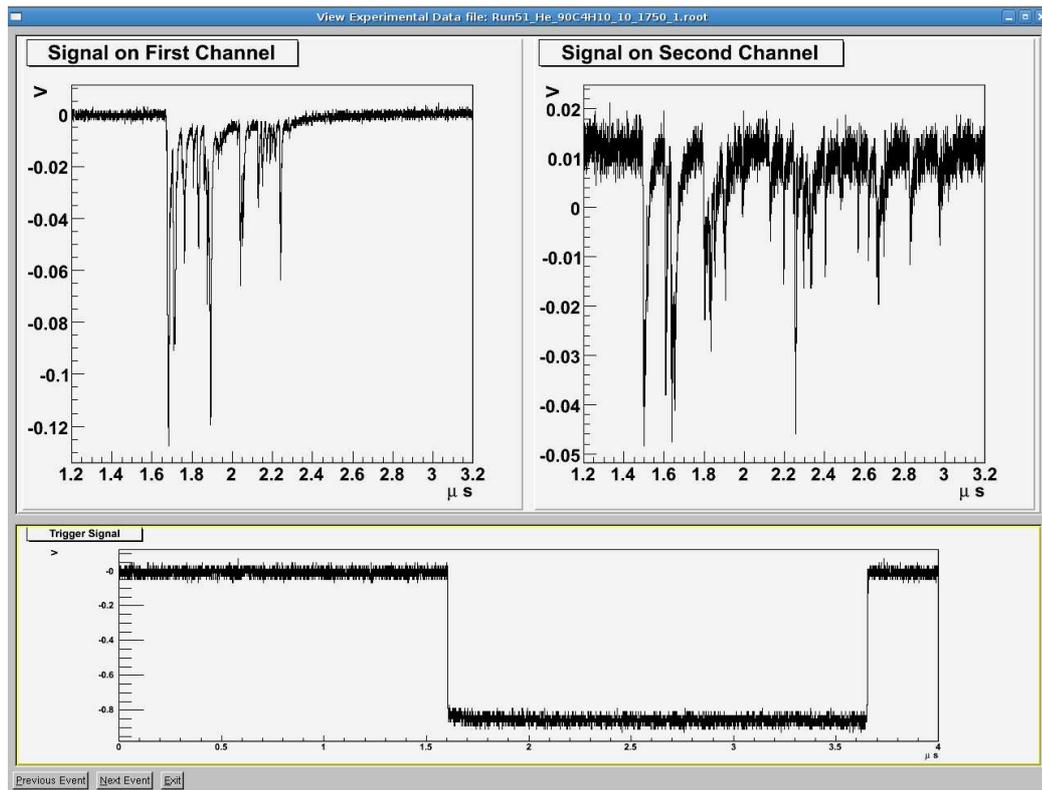
Figure 4.4: *Experimental drift tube signals. (left up) the signal of the drift tube with radius of 1.4 cm; (right up) the signal of the drift tube with radius of 2.0 cm. (bottom) the trigger signal.*
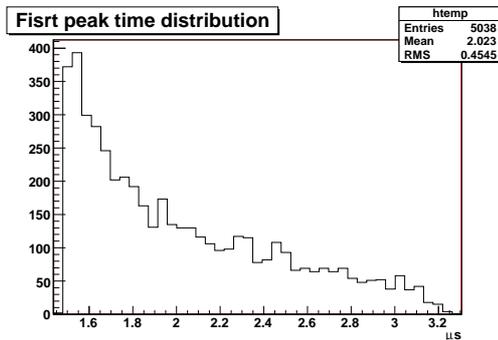
Figure 4.5: *Time distribution of first arrived peak for the drift tube with radius of 2 cm.*
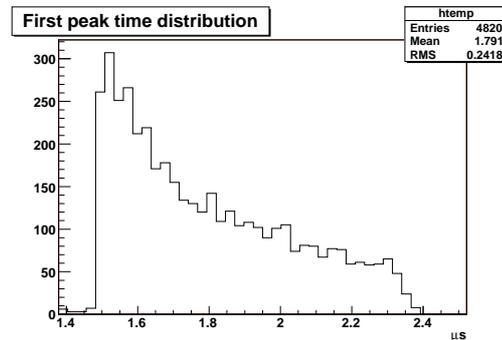
Figure 4.6: *Time distribution of first arrived peak for the drift tube with radius of 1.4 cm.*

4.7. Comparing it with the right upper picture of Fig. 4.7 we can see the effect of the integration over the fastest structures. A semi-quantitative analysis suggests that, with this bandwith limitation, not all the single electron peaks can be measured but all the clusters can be measured. A quantitative analysis of the net loss of the single electron peaks cannot be made by using the described method because, the approximated transfer function used, introduces oscillations in the signal tails that complicate the peak finding task. This problem will be solved by using the correct transfer function of the preamplifier.

The signal from 1.4 cm tube (shown in the left upper picture of Fig. 4.4) shows a more favorable signal to noise ratio with respect to the 2.0 cm tube. The preamplifier used, in fact, gives the possibility to work at a lower gas gain ($10^6$ instead of $10^7$ as in the 2.0 cm tube). This is a relevant aspect for a drift chamber, which ensures a greater stability of the working conditions. Applying the peak finding algorithm to the signals of this tube we have:
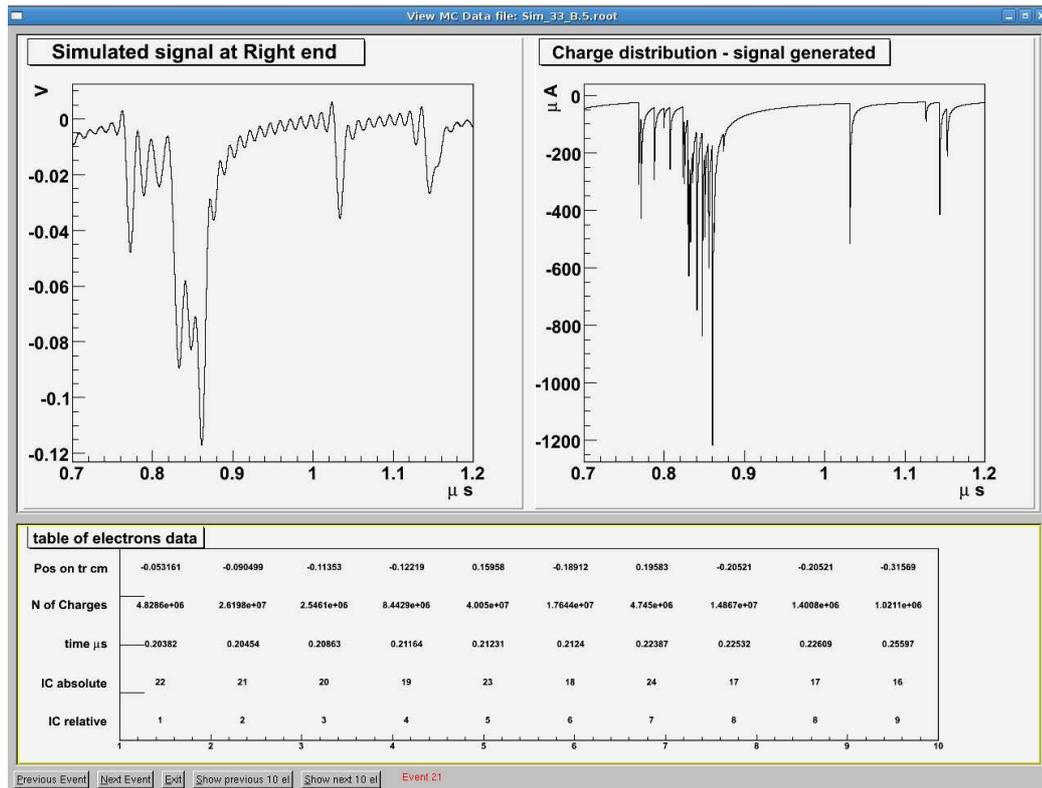
Figure 4.7: *(left up) detail of convoluted simulated signal in which the effect of the limited bandwidth of the preaplifier is included; (right up) signal generated by the drifting electrons in the drift tube; (down) ordered time sequence of the drifting electrons.*
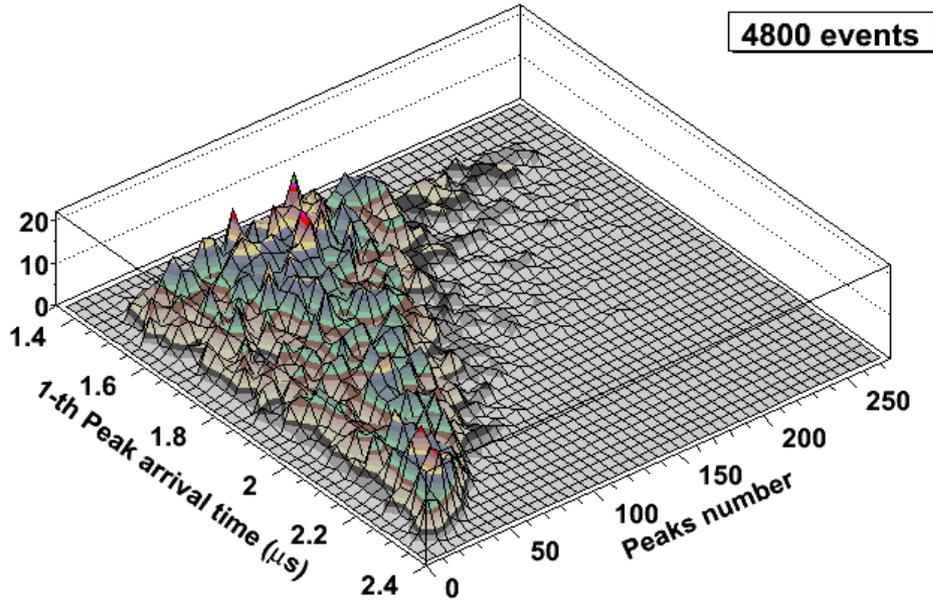
Figure 4.8: *Number of peaks counted vs the first peak arrival time for the drift tube with radius of 1.4 cm. The plot is referred to $\sim$ 5000 acquired events.*

- from the first peak arrival time distribution (Fig. 4.6) we measure a maximum drift time, of $\sim$ 900 ns in agreement with the one simulated of 940 ns (the variance due to the diffusion is 20 ns);

- the distribution of the number of the peaks counted as a function of the first peak arrival time (Fig. 4.8), which is directly correlated to the tracks impact parameters, shows how the number of peaks decreases with impact parameter for geometrical reasons. Unfortunately, since at this time the Si tracking telescope is not operative yet, we cannot measure the number of peaks produced per unit length. Our trigger system, infact, integrates all tracks with different impact parameter

within its polar angle acceptance. We can only conclude that the average number of peaks found is consistent with the average length of the chord subtended by the crossing track, given the angular acceptance of our scintillator trigger.

## 4.3   The Front End Electronics chip

The application of the cluster counting technique on a central tracking drift chamber is a complex endeavour because it requires sophisticated and up-to-date electronics. We have, therefore, started a project for the design of a read out electronics chip [54] with the function of a "fast ADC". 0.13 $\mu$m CMOS technology has been selected for the realization of this chip. With this technology we aim at reaching the following goals: sampling rate of 1 GSa/s, with 6 bit ADC and 1 GHz bandwidth. Moreover, the chip power consumption has to be limited to about 45 mW per channel, given the large number of channels of the proposed drift chamber.

### 4.3.1   The Lay-out

The chip is based on a fast amplifier directly connected to a fast ADC [54]. The schematic of the preamplifier is reported in Fig. 4.9. This scheme uses a closed-loop structure. However, due to the relatively small loop gain, it features large bandwidth and medium linearity (in excess of the ADC 6 bit performance), as required by the application. The main aim of the amplifier is to adjust the input signal level to the following ADC input range in order to exploit all its resolution capability. Therefore, the DC gain ($A_v$) must be programmable. The DC gain is calculated as follows:

$$A_v = 1 + R_0/R_i$$

Figure 4.9: *Schematic of the chip preamplifier.*

The programmability is obtained by using a resistors array to define $R_i$. The DC gain levels are in the range 0-20 dB. This operation has to be done without changing the shape of the input waveform. This means that for any gain level, a large bandwidth has to be guaranteed. Finally, due to the high input impedance of this stage, the R-C off-chip network does not affect the preamplifier DC gain and frequency response.

The noise performance of the readout channel is dominated by the noise contribution of the amplifier. The amplifier noise has been evaluated and the main source of it is represented by the thermal noise of transistor M6.
For the demanding 6 bit 1 GSa/s ADC, a two-steps architecture, has been used in which the signal quantization is accomplished by two quantizers, a 3 bit first stage with 1 bit of redundancy (i.e. 1 3.5b stage), and a 3 bit second stage. Both quantizers are implemented in a flash architecture. Consequently, only 21 comparators are required instead of 63 needed for a pure 6 bit flash ADC.
Details of the chip can be found in [54].

At the time of writing the first version of the chip has been built and a phase of check is starting.

# Chapter 5

# The CLUCOU Drift Chamber

## 5.1  The 4-th Concept at the ILC collider

In order to fullfill the physics programs at ILC, the experiments will have to satisfy the following constraints:

- jet energy resolution of $\sigma(E_j)/E_j = 30\%/\sqrt{E_j(GeV)}$;

- changed tracks transverse momentum resolution of $\sigma(1/pt) = 5 \times 10^{-5}$ $(\text{GeV/c})^{-1}$;

- solid angle as large as possible.

At this time three different conceptual experiments are proposed with similar general layouts, which are different only in the choice of technologies. They are: the International Large Detector (ILD), the Silicon Detector (SiD) and the 4-th Concept [55].

The 4-th Concept is the only one which does not rely on the algorithm of Particle Flow Analysis (PFA) [56] for event reconstruction. It proposes a calorimeter, DREAM, based on the recently tested idea of dual readout

[57]: by reading independently both the scintillation light, and the Čerenkov light, signals generated in a hadronic shower, in fact, one can reach almost full compensation between the hadronic and the e.m. complements of the shower. A large improvement on energy resolution is thus obtained.

The 4-th Concept is made of the following subdetectors. Starting from the interaction region to outside, Fig. 5.1:

- The vertex detector. It is based on the design of the SiD concept. It consists of 5 layers for the barrel part and 4 layers for each endcap; it makes use of $20 \times 20 \mu m$ pixel in order to reach a resolution on the impact parameter of $\sigma \approx 5 \mu m \bigoplus 10 \mu m / (p(\sin \theta)^{3/2})$;

- The central tracking system. It is a cylindrical, paraxial Drift Chamber made of small hexagonal cells in a Helium based gas and read out with the Cluster Counting technique. The DCH is the aim of this chapter and will be fully described later.

- The EM Calorimeter (ECAL). Dual Readout is being considered to increase the resolution on the electromagnetic fraction, which in HCAl, is limited by photoelectron statistics. Two possible solutions are being consider:

  1. a projective tower structure with alternating tiles of plastic scintillator and lead glass. In this case, the individual readout of each tile type provides the two components of the shower along its longitudinal profile;

  2. single crystals of lead tungstate. In this case, the two components are separated by the different physical properties of the Čerenkov and Scintillation light production mechanisms;
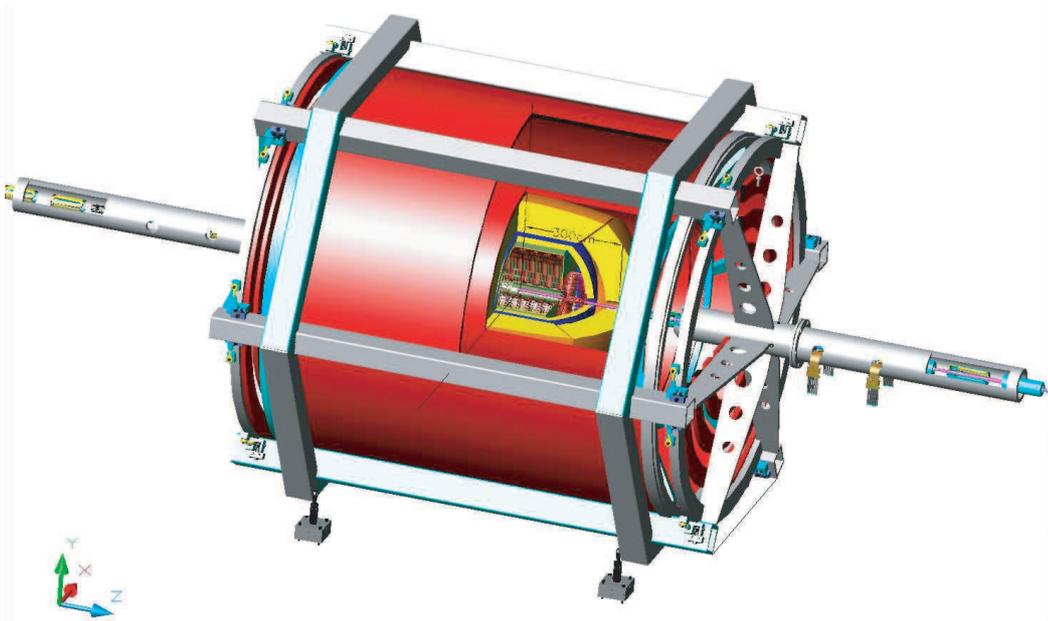
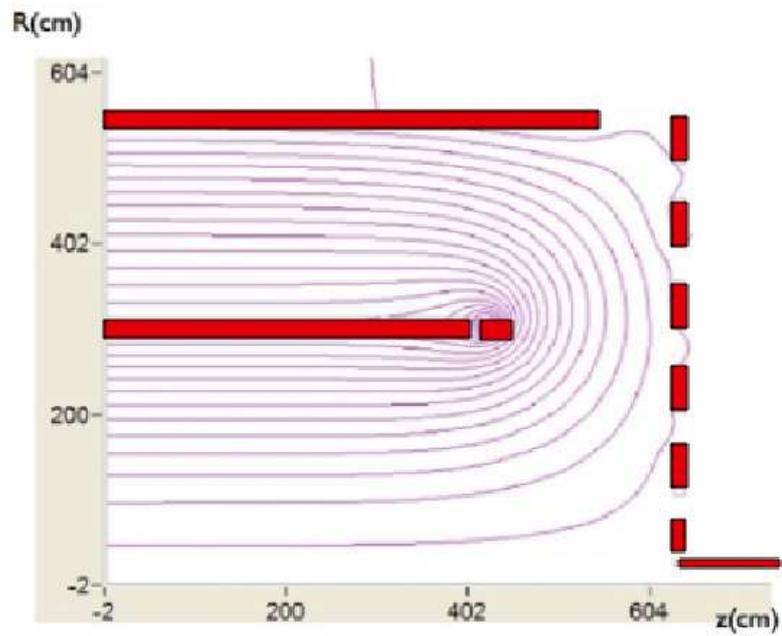Figure 5.1: *4-th Concept detector.*



Figure 5.2: *4-th Concept dual solenoid.*

- The Hadron Calorimeter (HCAL). It uses a fully projective layout. The basic element is made of copper and is loaded with both scintillating and quartz, or Čerenkov fibers oriented along the direction of the shower. The electromagnetic fraction of a shower is measured with an expected resolution of $\sigma(E)/E = 20\%/\sqrt{E(GeV)}$;

- The magnetic field. The tracking chamber and the calorimeters are placed inside a 3.5 T axial field provided by a superconductive solenoid. A second outer solenoid, with its field opposite to the inner one, will provide the flux return. An endcap wall of coils confines the flux of the two solenoids in $z$, and eliminates the need for massive iron flux return system, see Fig. 5.2;

- The Muon Spectrometer (MUON). Is made of three sections: a barrel section between the inner and outer solenoid and two endcaps. The basic element of the Muon Spectrometer is an aluminum proportional tube with a diameter of 4.6 cm. The barrel part consists of 3 staves, each containing 20 layers of tube planes of 4 meter length. Each stave contains 10500 tubes. The total length of the barrel is 12 meters, covering the range of $\pm 45°$ and the total number of tubes is 31500. The chambers are mounted into 12 trapezoidal sectors all made of only two building blocks, Fig. 5.3. The endcaps have a polygonal shape with twelve sides, perfectly matching the front shape of the barrel. Each endcap is made of three planar each made of 20 parallel tubes in depth sectors rotated by 120° with respect to each other, Fig. 5.4. The total number of tubes in each sector is 1440. Therefore, total number of tubes in each endcap is 4320. The total number of tubes in the Muon Spectrometer is 40140.
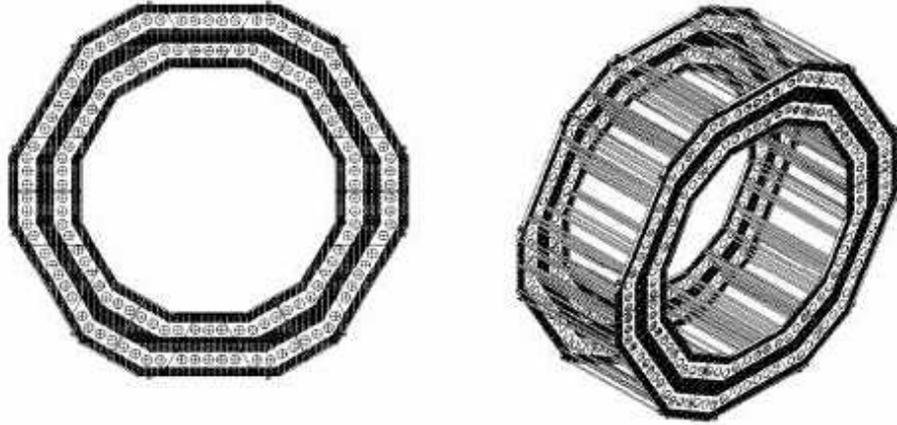
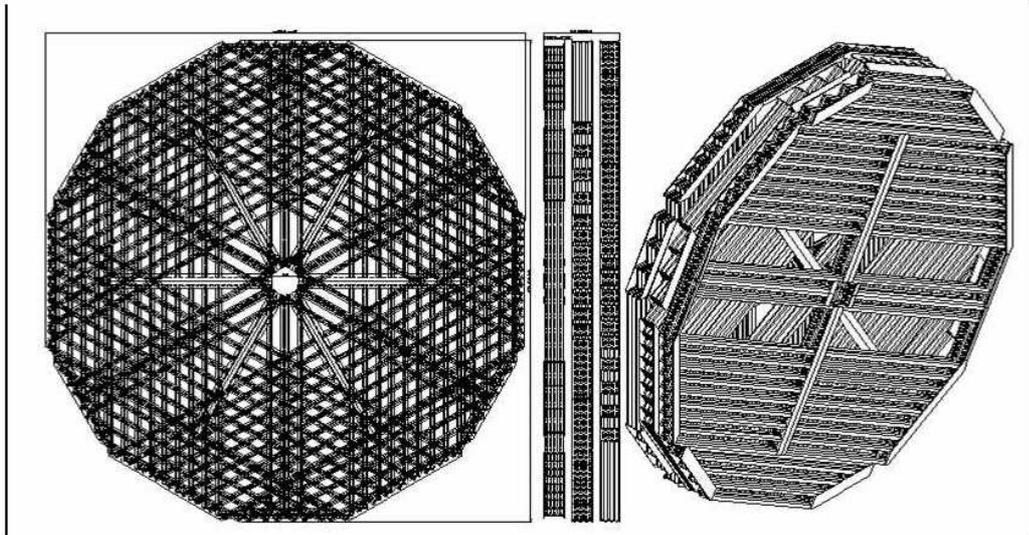Figure 5.3:  *One stave of the Muon Spectrometer Barrel.*



Figure 5.4:  *The Muon Spectrometer Endcap.*

## 5.2 The CLUCOU DCH layout

The proposed central tracking system is a fully stereo Drift Chamber for a precise reconstruction of tracks in space. A Helium based gas mixture and a light carbon fiber structure are chosen to minimize the multiple scattering contribution to the momentum measurement particularly for momenta below 20 GeV/c. Moreover, the use of the cluster counting technique guarantees good particle identification, of the order of $\sim 3\%$ (in sense of $\sigma(dN/dx)/(dN/dx)$), better spatial resolution and, therefore, good momentum resolution also for high momenta. Parameters like cell dimension, electric field and gas mixture can be tuned to ensure a maximum drift time shorter than the beam crossing interval, 337 ns, to prevent pileup of events.

### 5.2.1 Mechanical structure

The chamber volume is a cylinder of 22.5 cm inner radius, 150 cm outer radius with 300 cm $z$ length. The inner wall is made of a thin (0.2 mm) carbon fiber foil covered by a 30 $\mu$m Aluminum layer for electrostatic continuity (equivalent to 0.001 $\mathbf{X}_0$). The outer wall (equivalent to 0.020 $\mathbf{X}_0$) is made of six carbon fiber aluminum hexcell sandwich panels held by 6 structural staves made of unidimensional carbon fibers, Fig. 5.5. The end caps are made by carbon fiber aluminum hexcell sandwich plates, in analogy to the outer wall, with a total thickness of $\sim 3$ cm and equivalent carbon fiber thickness of $\sim$ 8 mm (equivalent to 0.040 $\mathbf{X}_0$), to close the gas volume and to hold in place, at the right tension, all the wires. To balance the total wire tension, equivalent to $\sim 15$ ton, the end plates are going to be pre-stressed before the wiring.
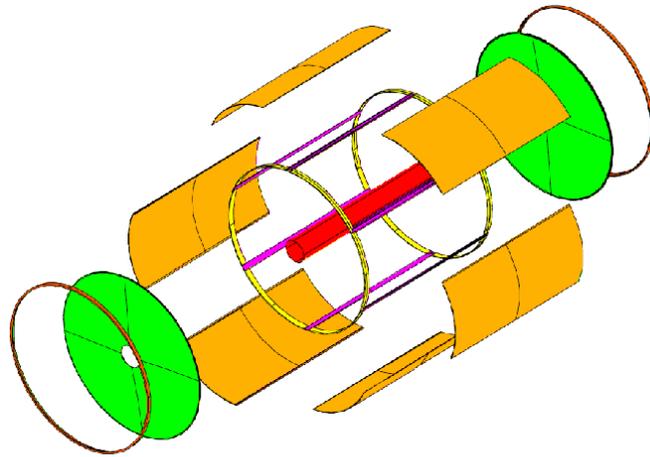
Figure 5.5:   *CLOCOU DCH mechanical structure sketch.*

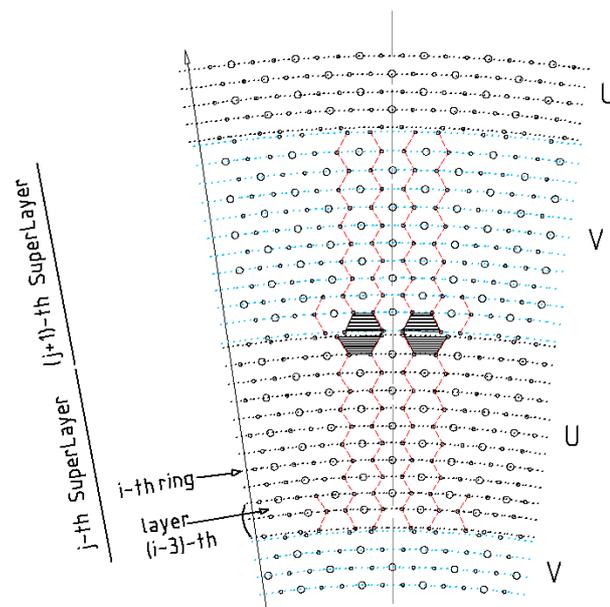

Figure 5.6:   *Small radial and azimuthal portion of the CLOCOU drift chamber at z=0, showing the cell, layer and superlayer layout and the stereo configuration.*

## 5.2.2 Layer and Superlayer structures

We define the generic "ring" of the $i$-th "layer" within the $j$-th "superlayer", as the circumference of radius $r_{ij}$ in the $x - y$ plane at $z = 0$ having $n_j^w$ wires with $n_j^w = 3n_j^{sw} = 3/2n_j^{fw}$, where $n_j^{sw}$ and $n_j^{fw}$ are, respectively, the number of sense wires and the number of field wires($n^w = n^{sw} + n^{fw}$), which are costant, in every ring of the superlayer. The spacing between wires is $b_{ij} = r_{ij}\theta_j$ where $\theta_j = 2\pi/n_j^w$. The spacing between two consecutive rings is defined by $r_{i+1,j} - r_{i,j} = \sqrt{3}/2\,b_{ij}$ and the order of the sequence of field and sense wires is rotated by $3/2\,b_{ij}$ in going from the $i$-th ring to the next $(i+1)$-th one. This means that in any three consecutive rings $(r_{i-1,j}, r_{i,j}, r_{i+1,j})$, defining the $i$-th layer of a generic superlayer $j$, we can build $n_j^{sw}$ (almost) perfect hexagonal cells with 6 field wires at the vertices and a sense wire at the center. In general, the radial cell asymmetry in the drift cell, with respect a perfect hexagon is:

$$A_r^j = 1 - \frac{b_{i,j}}{b_{i-1,j}} = 1 - \frac{r_{i,j}}{r_{i-1,j}} = \frac{\sqrt{3}\pi}{n_j^w}$$

whereas the azimuthal asymmetry is:

$$A_\phi^j = 1 - \frac{b_{i+1,j}}{b_{i-1,j}} = 1 - \frac{r_{i+1,j}}{r_{i-1,j}} = 1 - \left(1 + \frac{\sqrt{3}\pi}{n_j^w}\right)^2.$$

As it is shown in Fig. 5.6, a superlayer is made of $l + 2$ consecutive rings, where $l$ is the number of layers, the first $(r_{0,j})$ and the last $(r_{l+1,j})$ rings being shared with the preceding $(j - 1)$ and following $(j + 1)$ superlayers. respectively. Since at the boundaries between consecutive superlayers one must have equipotential surfaces, one half of the regions between $r_{0,j}$ and $r_{1,j}$ and between $r_{l,j}$ and $r_{l+1,j}$ cannot be used for charge collection of the drifting electrons, as shown in Fig. 5.6, leading to a loss of coverage in the active volume of $1/(l + 1)$.

For the drift chamber configuration at ILC, we have chosen $l = 10$ layers in each superlayers for a total of 20 superlayers starting $r_{0,1} = 25.0$ cm (at $z = \pm\frac{L}{2}$) up to $r_{11,20} \sim 150$ cm. This configuration calls for $n_1^{sw} = 60$ cells per layer at the innermost superlayer, up to $n_{20}^{sw} = 440$. In order to keep the cell size as constant as possible throughout the 20 superlayers, the generic $j$-th superlayer will the have $40+20\cdot j$ cells per layer.

The total number of sense wires, $N^{sw}$, and field wires, $N^{fw}$, will be:

$$N^{sw} = \sum_{1,j}^{20} l(40 + 20j) = 50.000$$
$$N^{fw} = \sum_{1,j}^{20} 2(l + 1)(40 + 20j) = 110.000 \tag{5.1}$$

arranged in hexagonal cells of $\sim 0.7$ cm side, in such a way that a radially outgoing track of infinite momentum will cross on average 134 cells. In this case, the radial and azimuthal asymmetries go from minimum values of 0.004 and 0.008 respectively, at the outermost superlayer, to 0.03 and 0.06 at the innermost superlayer. And the loss of coverage in the active volume amounts to $\sim 9$ %.

As far as the wire orientation in space is concerned, of the several different possible arrangements, we have chosen the one which preserves the shape of the cell throughout the length of the chamber. Referring to Fig. 5.7, this is reached by keeping the "drop" $\delta$ constant as a function of the radius $r_{i,j}$ of the ring.

The stereo angle $\epsilon_{i,j}$ will then be defined by:

$$\varepsilon_{i,j} = \arctan \frac{\delta}{L_{i,j}/2} \sqrt{\frac{2r_{i,j}}{\delta} - 1}$$

where $L_{i,j}$ is the length of the wire at radius $r_{i,j}$ (constant for a cylindrical chamber with planar end plates). For a drop $\delta = 2$ cm, the stereo angles range from $\epsilon_{i,j} \sim 70$ mrad, at the innermost ring, to $\epsilon_{i,j} \sim 180$ mrad at the outermost ring. For a chamber with hemispherical end plates, the stereo
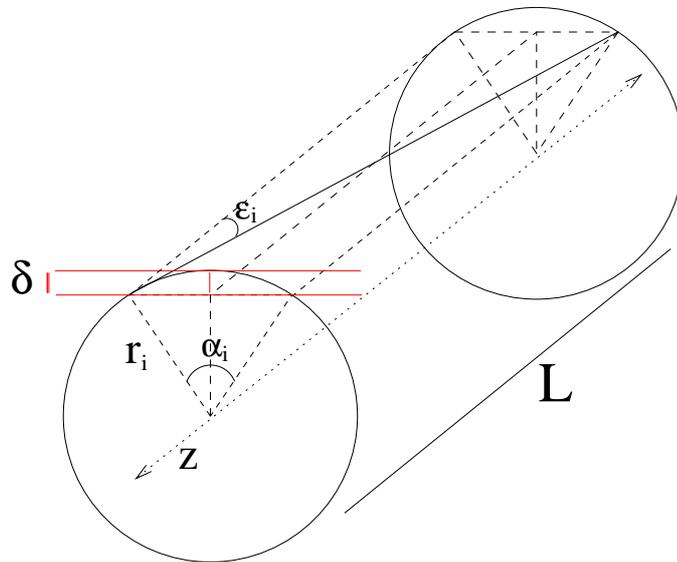
Figure 5.7:  *Geometrical configuration of a stereo wire. δ is the drop, $\varepsilon_i$ is the stereo angle for the i-th ring.*
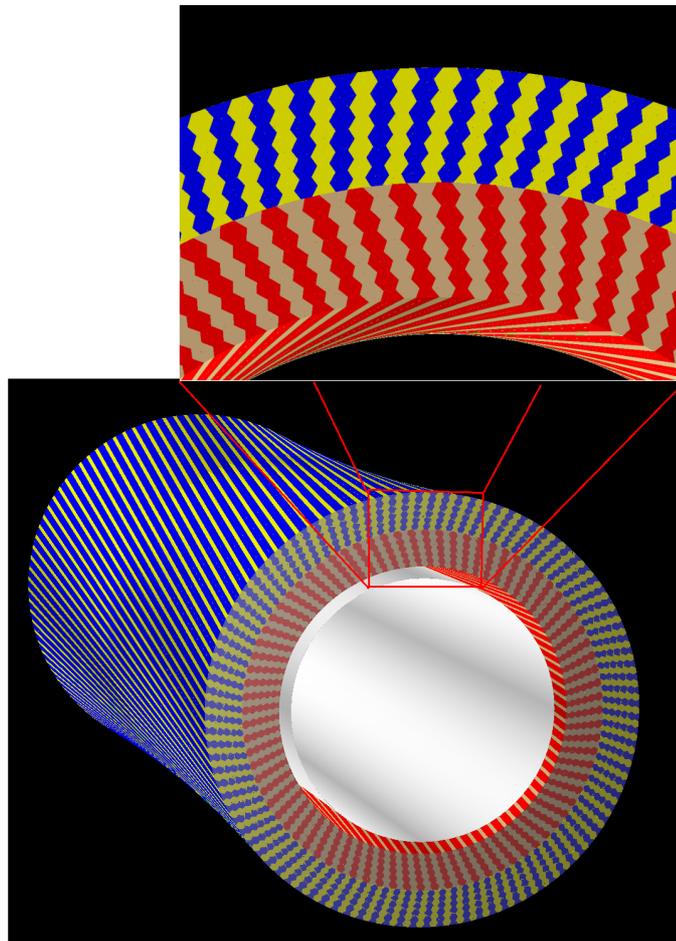


Figure 5.8:  *Cells envelope rendering view of the first two SuperLayers of the CLOCOU DCH.*

angles will be almost independent of the ring radius.

In Fig. 5.8 is shown a view of the two layers of the chamber where we can see the envelope of the cells after the stereo angle rotation.

### 5.2.3    Cell width, drift velocity and Gas and gain choice

The average cell dimension just described is $\sim 0.7$ cm. With a gas mixture of 90% He and 10% isobutane, the needed gas amplification gain, of the order of $10^6$, is reached with a +HV on the sense wire ($25\mu$m diameter) in the range 1450-1650 V. In this configuration and in absence of a magnetic field, the maximum drift time is expected to be $\sim 320$ ns. The variance of this value, due to diffusion, is $\sim 8$ ns. Despite the low drift velocity in the He gas mixture, that guarantees a small Lorentz angle, the presence of an intense magnetic field ($\sim 3.5$ T) will distort these values. In particular, the maximum drift time grows up to $\sim 700$ ns with a diffusion variance of 10 ns. The presence of an intense magnetic field, therefore, might introduce a problem of event pileup (the beam crossing time at ILC is 337 ns), depending on the hit multiplicity per event, but it has no considerable effect on single cell resolution. The event pileup can be reduced by tuning the drift velocity through the HV and the gas composition and by optimizing the cell size.

### 5.2.4    Cell electrostatic stability

In a drift chamber with elementary cells of small dimensions the electrostatic forces among field and sense wires may be not negligible and may displace a wire from its nominal position creating distortions in the electrical field configuration with a consequent increase of the electrostatic force among wires. Because of mechanical tolerances in the chamber construction, the wire

positions are known with an uncertainty of $\sim 50$ $\mu$m to which one must add the contribution due to the spread of the wires gravitational sagittas. The equation that describes the vertical displacement $x$, from the ideal straight trajectory of a wire as a function of the coordinate along $y$ is [39]:

$$T\frac{d^2x}{dy^2} + kx + g\rho\sigma \tag{5.2}$$

where $T$ is the mechanical tension given to the wire, $kx$ is the electrostatic force acting on it, $\rho$ is the wire density and $\sigma$ is its transverse cross section, all per unit length. Solving Eq. 5.2 for the case of no electric field, we obtain the gravitational wire sagitta:

$$s_g = \frac{L^2 g\sigma\rho}{8T} \tag{5.3}$$

where $L$ is the wire length. In presence of an electric field, the sagitta due to both the electrostatic and the gravitational forces is:

$$s = s_g\frac{2}{q^2}\left(\frac{1}{\cos q} - 1\right) \quad, \quad q^2 = \frac{k}{T}\left(\frac{L}{2}\right)^2. \tag{5.4}$$

The $\alpha = \frac{2}{q^2}\left(\frac{1}{\cos q} - 1\right)$ term represents the incremental factor of the gravitational sagitta due to the addition of the electrostatic force. The cell is electrostatically stable when $q^2 \leq 1$. An approximated expression for $q^2$ can be written:

$$q^2 = 4\pi\epsilon_0\frac{1}{[a\ln(a/r)]^2}\frac{V^2}{2T}\frac{L^2}{4} \tag{5.5}$$

where $r$ is the radius of the wire and $a$ is the typical spacing between sense and field wires.

By displacing the sense wire within a cell, we can compute $\alpha$, the ratio between the electrostatic and the gravitational sagitta.

For simplicity, we have considered the case of an array of regular hexagonal cells, 0.6 cm side with 80 $\mu$m field wires at the vertices and 25 $\mu$m sense wire
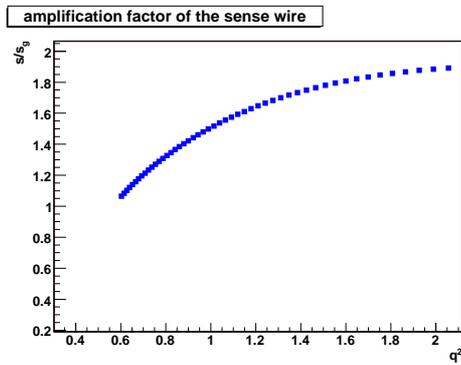
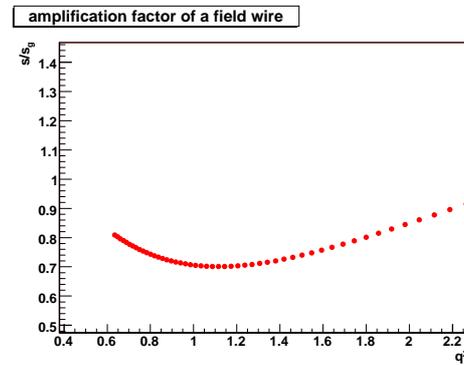Figure 5.9: $\alpha$ for the sense wire as a function of $q^2$.



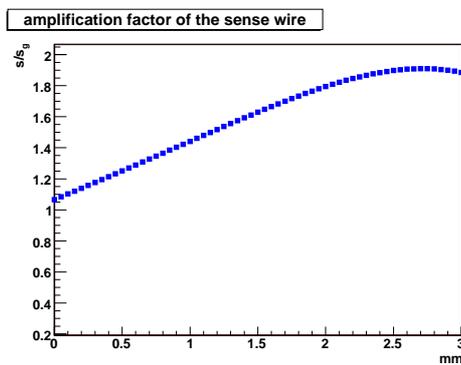Figure 5.10: $\alpha$ for the field wire as a function of $q^2$.



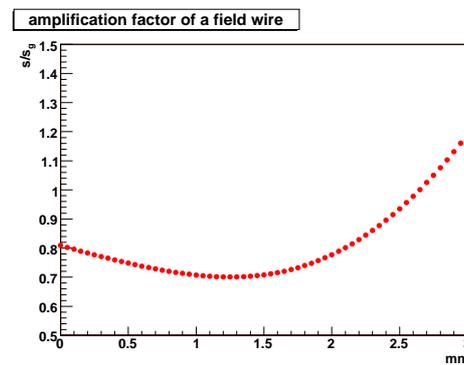Figure 5.11: $\alpha$ for the sense wire as a function of the sense wire displacement.



Figure 5.12: $\alpha$ for the field wire as a function of the sense wire displacement.

at the center and HV of 1800 V (like in Fig. 5.6). By displacing the central sense wire, we get the plots of Fig. 5.9, 5.10, 5.11 and 5.12. The cell can be considered stable for sense wire displacements up to about 1 mm, which is much larger than the tolerance on the wire position.

## 5.3 CLUCOU DCH performance

To study the drift chamber response in a close to *real* environment we have implemented its simulation within the ILCRoot framework. ILCRoot is a framework software inspired to the offline software of the ALICE experiment (AliRoot) [58], from which it inherits the architecture. This framework is flexible enough to allow for development of the code for different purposes, from the simulation to the data analysis, including the management of the detector geometry, the sub-detector response, the digitization and the reconstruction. The software suite consists of a set of C++ classes that are complied against the ROOT utility library and loaded in the ROOT framework for further data processing and/or analysis job.

In this section we show the momentum resolution for the described chamber and its performance on selected physics channels [59]. In particular, we present the chamber response in the SM Higgs-strahlung process, $e^+e^- \rightarrow ZH \rightarrow l^+l^- + X$, and on $e^+e^- \rightarrow t\bar{t} \rightarrow 6jets$. The first process is a very important benchmark channel to understand the central tracking detector performances because, by measuring only the momentum and by identifying the two leptons, it is possible to reconstruct, with high precision, the Higgs mass using the recoil mass analysis. Moreover this channel offers the possibility of measuring the suppressed $H \rightarrow \mu^+\mu^-$ decay. The second channel, used for precision SM measurement of $(g-2)_t/2 \leq 10^{-3}$ at $5\sigma$, is not a direct

benchmark for the central tracking momentum resolution but, rather, for its reconstruction efficiency and its capability to respond in a very high event multiplicity environment. It is important to notice that the trackers ability to efficiently reconstruct very low p$_T$ charged tracks and to identify very low momentum leptons, unable to reach the calorimeters or the muon detector, is fundamental to measure SUSY events like in $e^+e^- \rightarrow \tilde{l}^+\tilde{l}^- \rightarrow \tilde{\chi}_1^0\tilde{\chi}_1^0 l^+l^-$. Inside ILCRoot, the reconstruction is performed by using the Kalman filter, derived by ALICE [60], and adapted to the 4-th Concept detectors geometry. For these studies, we have implemented a simulation with the following approximations:

- a single cell is able to measure the impact parameters of up to two crossing tracks, separated in time by at least 2 ns;

- the track impact parameters are smeared using Gaussian distributions with 55 $\mu m$ sigma for the first track and with 100 $\mu m$ sigma for the second track;

- the coordinates of the impact point in a cell are reconstructed, assuming 100 % efficient pattern recognition, with the following correlation functions:

$$\sigma_{xy} = \sigma_b/\cos\varepsilon \ , \quad \sigma_z = \frac{\sigma_{xy}}{\tan\varepsilon} \ , \quad V_{xyz} = \begin{pmatrix} \sigma_{xy}^2 & \sigma_{xy}\sigma_z \\ \sigma_{xy}\sigma_z & \sigma_z^2 \end{pmatrix}$$

where $\varepsilon$ is the stereo angle, $\sigma_b$ is the impact parameter resolution and $V_{xyz}$ the coordinate correlation matrix.

## 5.3.1   Results

For single track momentum resolution studies we have simulated 500 events with 50 single muons each. We have also repeated this study with a con-

ventional single cell resolution (100 $\mu$m for the first track and 150 $\mu$m for the second one instead of 55 $\mu$m and 100 $\mu$m) to estimate the worst momentum resolution limit for the DCH proposed here. The results on momentum resolution are shown in Fig. 5.13. The blue line refers to the high (55 $\mu$m and 100 $\mu$m) resolution case, the red line to the low (100 $\mu$m and 150 $\mu$m) resolution case and the black line is the resolution of a typical TPC proposed for ILC. From the figure it is clear how the high transparency (in terms of
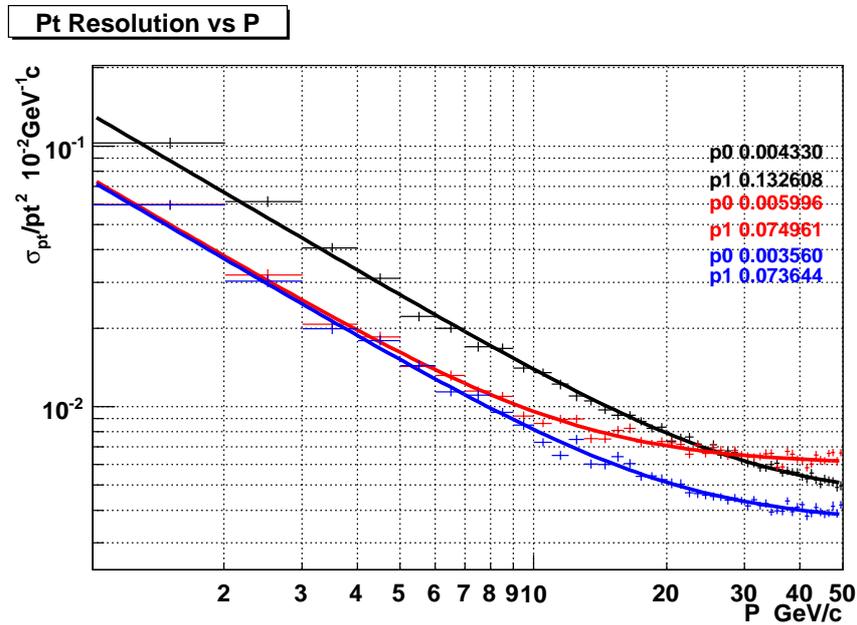


Figure 5.13:  *mometum resolution, as a function of the particle mometum, for the CLOCOU DCH with high resolution, blue line, with low resolution, red line, and for a typical TPC proposed for ILC, black line.*

material) of the CLUCOU DCH affects the momentum resolution for particles with momentum $\lesssim 20$ GeV/c. Furthermore, it is interesting to notice how the CLUCOU DCH, even with low spatial resolution, can reach a quite good momentum resolution.

The ability of this chamber to work properly in every conditions at ILC has

been further analysed, evaluating the average cell and layer occupancies for the two physics channel described above. For the case of Higgs-strahlung process, Fig. 5.14, 5.15, the cell occupancy is larger than 1 only for the innermost layers and this channel constitutes no problems. For the highest multiplicity $t\bar{t}$ events, Fig. 5.16, 5.17, the first few inner superlayers have an average occupancy of 50 % with an average 1.5 cell occupancy which may complicate the pattern recognition and the track finding capabilities. However, Fig. 5.18 shows that, once the tracks have been found, the reconstruction efficiency for these events remains high throughout the whole momentum range.

Finally, we have analysed the impact of the CLUCOU drift chamber on the SM Higgs mass measurement with the recoil mass technique in the case of the Higgs-strahlung process:



$Z^0$ *Higgs-strahlung Feynman diagram.*
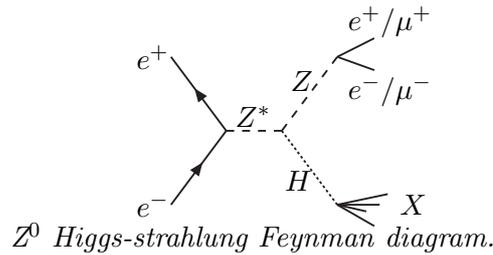
The recoil mass analysis is an unbiased strategy to measure the Higgs mass, inclusively, by identifying and measuring the momentum of the two leptons in the final state. The Higgs mass is given by:

$$M_H^2 = E_H^2 - \vec{p}_H^{\,2} = (E_{CM} - E_Z)^2 - \vec{p}_Z^{\,2} \ , $$
$$E_Z = E_{l_1} + E_{l_2} \ , \quad \vec{p}_Z = \vec{p}_{l_1} + \vec{p}_{l_2}$$

(5.6)

where $E_Z$ and $\vec{p}_Z$ are, respectively, the energy and the momentum of the $Z$ boson and $l_i$ are the leptons in the final state. At ILC the beam-beam interaction, beamstrahlung [61] and Initial State Radiation (ISR), may be not negligible so that, event by event, the CM is boosted respect to the laboratory frame and the $E_{CM}$ is spread around the nominal value ($\tilde{E}_{CM}$). To evaluate
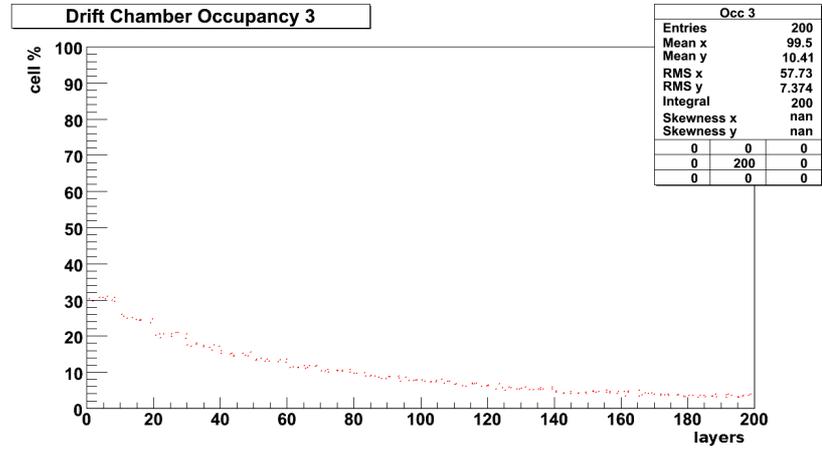
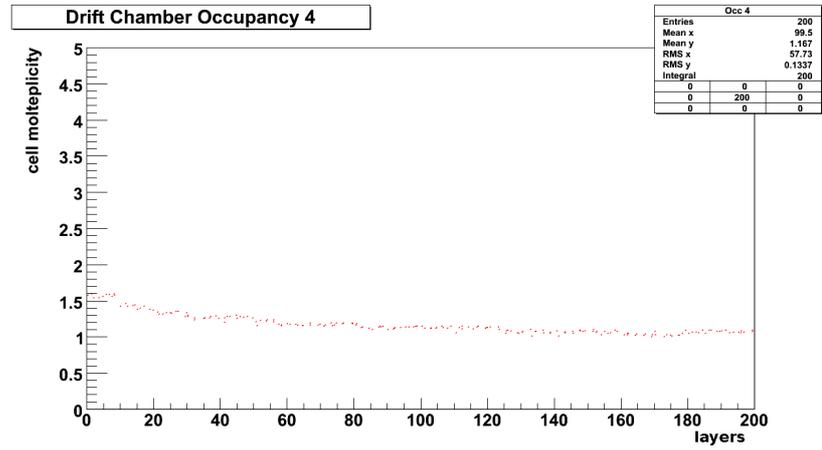Figure 5.14: *Layer occupancy for ZH events at $E_{CM}$=230 GeV.*



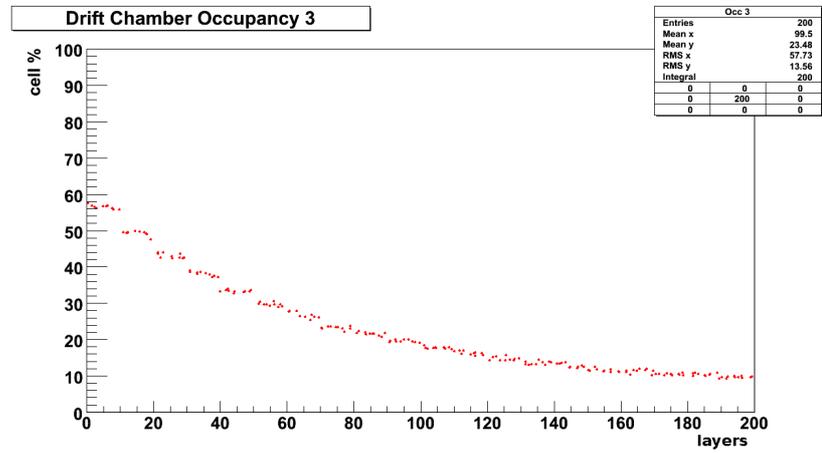Figure 5.15: *Cell occupancy for ZH events at $E_{CM}$=230 GeV.*

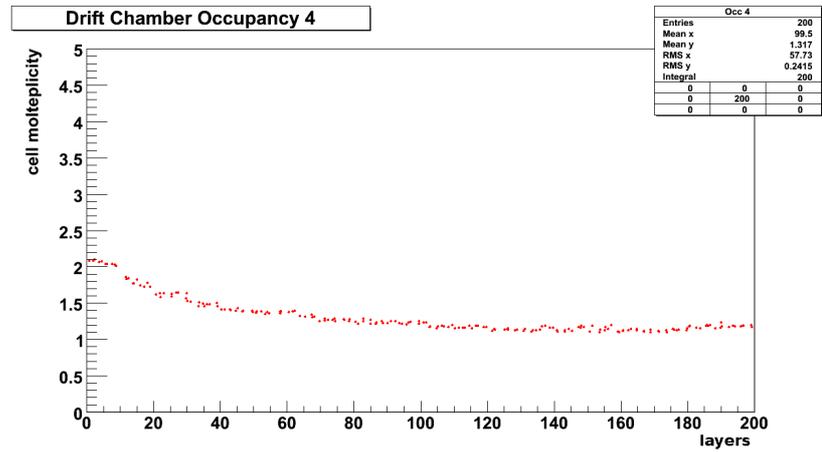Figure 5.16: *Layer occupancy for t$\bar{t}$ events at E$_{CM}$=500 GeV.*



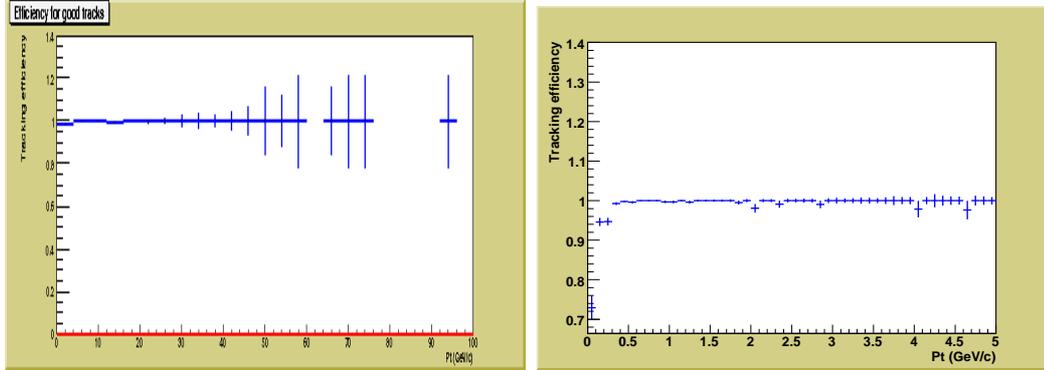Figure 5.17: *Cell occupancy for t$\bar{t}$ events at E$_{CM}$=500 GeV.*

Figure 5.18: *CLOCOU DCH track reconstruction efficiency for $t\bar{t}$ events at $E_{CM}$=500 GeV, (left) whole particle mometum range, (right) detail for slow particles.*

this effect on the Higgs mass resolution, we have simulated these processes with Pandora-Pythia [62] event generator that takes into account the ISR and the beamstrahlung. In particular, we have used the Yokoya-Chen formula [63] for the beam energy loss for beamstrahlung with parameters tuned on ILC properties with the help of Guinea Pig [64]. The resulting CM energy distribution, shown in Fig. 5.19, has a Gaussian component centered at $\tilde{E}_{CM}$ with $\sigma \simeq 100$ MeV and a long tail due to the beamstrahlung with the form of the Yokoya-Chen formula $f(E) = p_3 e^{-p_4 \cdot (\tilde{E}_{CM} - E)}/(\tilde{E}_{CM} - E)^{2/3}$.

We have simulated the case in which the $Z$ boson decays in two muons, the Higgs has a mass of 120 GeV/c$^2$, with negligible width, and CM energy near the production threshold, $\tilde{E}_{CM} = 230$ GeV, where a larger cross section for the production of $H$ with $Z$ [65] than at the $t$ quark threshold, $\tilde{E}_{CM} = 350$ GeV is expected. Applying the Eq. 5.6 directly to the Pandora Pythia events we have that at ILC, integrating 500 fb$^{-1}$ of luminosity, the limits on the Higgs mass measurement, using the recoil method in the $Z \rightarrow \mu^+\mu^-$ channel, are $\sigma \simeq 134$ MeV/c$^2$ with a systematic shift of 58 MeV/c$^2$, Fig.
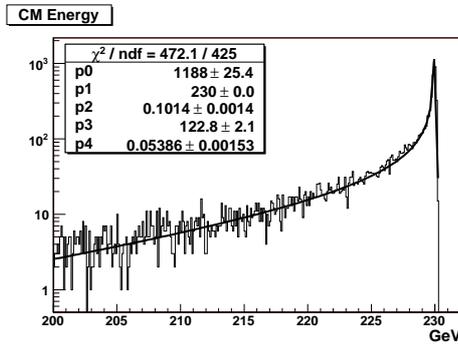
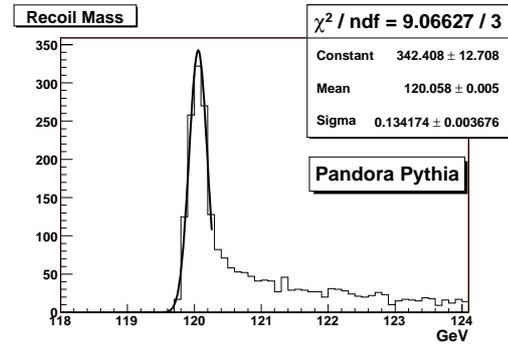Figure 5.19: *$E_{CM}$ distribution simulated with Pandora Pythia.*

Figure 5.20: *recoil Higgs mass from Pandora Pythia events.*

5.20.

To understand the impact of the lepton momentum measurement on this result, the above events have been simulated and reconstructed in the ILCRoot framework. Background has been taken into account as well. The larger contribution is given by the production of two $Z$ boson for which at least one $Z$ decays into two muons: $e^+e^- \rightarrow ZZ \rightarrow \mu^+\mu^- + X$, with an expected number of $\simeq 24000$ background over $\simeq 3400$ signal events. The reconstruction of the $Z$ boson, decaying into two muons, is done by selecting, among all the reconstructed muons, the $\mu^+ - \mu^-$ pair that gives a $Z$ invariant mass nearest to the $Z$ mass value. The correctness of this choice is confirmed by Fig. 5.21. The small muon deficit is due to the geometrical acceptance of the detector. Finally, we can see that with the momentum resolution of the CLUCOU drift chamber the $Z$ mass is reconstructed with a precision of $\lesssim 150$ MeV/c$^2$ (Fig. 5.22) as expected from the Linear Collider design, and the Higgs mass can be reconstructed with a $\sigma \simeq 330$ MeV/c$^2$ and a systematic shift of $\simeq 110$ MeV/c$^2$ (Fig. 5.23). In the case of a drift chamber with low resolution, the
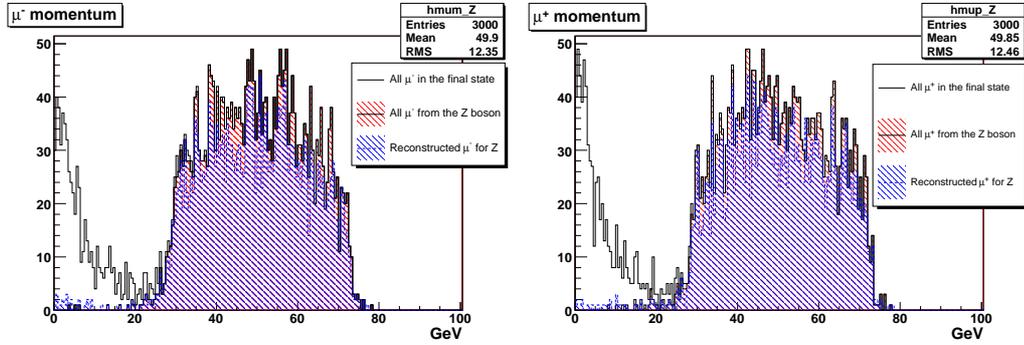
Figure 5.21: *Momentum distribution of $\mu^-$ (left) and $\mu^+$ (right) in 3000 events of $e^+e^- \to ZH \to \mu^+\mu^- + X$ for $M_H$= 120 GeV/$c^2$ and 500 fb$^{-1}$ at ILC with $E_{CM}$=230 GeV.*
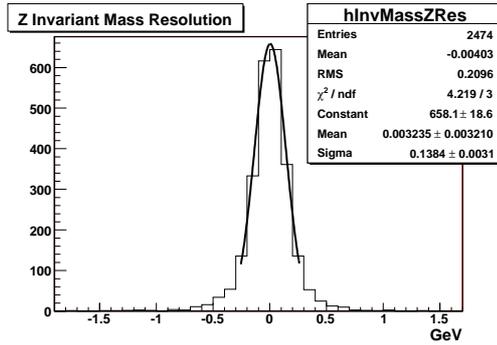


Figure 5.22: *Z boson invariant mass resolution distribution in the process $e^+e^- \to ZH \to \mu^+\mu^- + X$ for $M_H$= 120 GeV/$c^2$ and 500 fb$^{-1}$ at ILC with $E_{CM}$=230 GeV.*

Figure 5.23: *expected recoil mass distribution in the process $e^+e^- \to ZH \to \mu^+\mu^- + X$ for $M_H$= 120 GeV/$c^2$ and 500 fb$^{-1}$ at ILC with $E_{CM}$=230 GeV.*

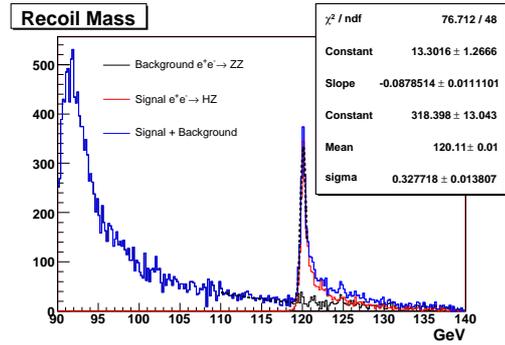$Z$ mass is reconstructed with a precision of $\lesssim 230$ MeV/c$^2$ and the Higgs mass with a $\sigma \simeq 450$ MeV/c$^2$ and a systematic shift of $\simeq 170$ MeV/c$^2$.

# Conclusions

Recently, the interest shown by the international scientific community in the possibility to build new collider experiments besides LHC has stimulated new ideas for detector R&D. Two of the proposed projects, the "International Linear Collider" (*ILC*) and the "Super B factory" (*SuperB*) will explore Physics complementary to the LHC. In particular ILC can be considered a machine for precision measurements on Standard Model Physics and beyond it; SuperB measures the CP violating b sector at the highest luminosity and can explore physics channels unmeasurable at LHC. Considering the single machine peculiarities, the potential discovery of each of these colliders can be increased by adopting a combined research strategy: the construction of the new colliders must be planned concurrently with the running of LHC.

This work is part of a R&D project for a central tracking system proposed for the future colliders experiments. We have investigated the possibility of applying the cluster conting technique to the readout of a Helium based Drift Chamber to improve the tracker performance. In particular, Monte Carlo simulations, based on Garfield, to study the properties of a single drift cell have been performed. To this aim, a Fourier analysis, describing the propagation phenomena of the signal inside a drift cell, has been shown to be fully compatible with the predictions made by PSpice. An algorithm for a highly efficient single electron counting and for the association of electrons

in clusters has been developed together with an algorithm which uses the spatial cluster distribution to reconstruct the impact parameter with high precision. An experimental setup has been built to check the consistency of the MC predictions. Several measurements have been done to monitor the performance of the cluster counting algorithm and to measure the cluster densities and other relevant quantities. A telescope, made of six planes of silicon detector, has been built and is under commissioning. It will be used to reconstruct tracks with excellent resolution ($\sim 20~\mu$m) in order to directly validate the proposed reconstruction algorithm.

We have, then, designed a Drift Chamber, based on these studies and in the last chapter, we have discussed in detail its geometry and its properties. We conclude with the studies performed within the 4-th Concept framework and with the aid of the ILCRoot software (a tool for full simulation and Physics analysis of the ILC 4-th Concept experiment). Preliminary results confirm that the proposed Drift Chamber will be able to reach the tracking performance goal, proposed for ILC, of $\sigma(1/p_T) = 5 \times 10^{-5}(GeV/c)^{-1}$ at high $p_T$ and, given the negligible contribution to $p_T$ due to multiple Coulomb scattering, an excellent resolution also at low $p_T$.

# Bibliography

[1] for reviews, see:

E.S. Abers, B.W. Lee: Phys. Rev. **9** (1973) 1;

M.A.B. Beg, A. Sirlin: Phys. Rep. **88** (1982) 1;

P. Langacker: Phys. Rep. **72** (1981) 185;

P. Langacker, J. Erler: Phys. Rev. **D50** (1994) 1304.

[2] R.D. Field: *Perturbative QCD*: Addison–Wesley, Redwood City (1989);

F.J. Yndurain: *The Theory of Quark and Gluon Interactions*: Springer–Verlag, Berlin (1993).

[3] S.L. Glashow: Nucl. Phys. **22** (1961) 579;

S. Weinberg: Phys. Rev. Lett. **19** (1967) 1264.

[4] F. Halzen, A.D. Martin: *Quarks and leptons An Introductory Course in Modern Particle Physics*: *John Wiley & Sons* New York (1984).

[5] H. Weyl: Z. Phys. **56** (1929) 330;

C.N. Yang, R. Mills: Phys. Rev. **96** (1954) 191.

[6] N. Cabibbo: Phys. Rev. Lett. **10** (1963) 531.

[7] M. Kobayashi, T. Maskawa: Prog. Theor. Phys. **49** (1973) 652.

[8] L. Wolfeinstein: Phys. Rev. Lett. **51** (1983) 1945.

[9] M. Gronau, D. Wyler: Phys. Lett. B **265** (1991) 172.

[10] B. Aubert et al.: Phys. Rev. Lett. **89** (2002) 201802.

[11] K. Abe et al.: Belle-CONF-0353, LP'03 (2003).

[12] Atlas Technical Proposal: http://atlas.web.cern.ch/Atlas/TP.

[13] *Zeroth-Order Design Report for the Next Linear Collider*: SLAC Report 474, LBNL-PUB-5424, May 1996.

[14] I. Watanabe et al.: *JLC Design Study*: KEK Report 97-17 April 1997.

[15] R. Brinkmann et al.: *Conceptual Design of a 500 GeV Electron Positron Linear Collider with Integrated X-Ray Laser Facility DESY 97-048, ECFA-97-182*: Nuclear Instruments and Methods in Physics Research **A406** (1998) 13.

[16] V. Telnov: *High-energy photon colliders*: Nuclear Instruments and Methods in Physics Research **A455** (2000) 63-69.

[17] *PEP-II Conceptual Design Report*: SLAC-372, LBL-PUB-5303, CALT-68-1715, UCRL-ID-106426, UC-IIRPA-91-01 (1991);
J. Seeman et al.: Contributed to European Particle Accelerator Conference (EPAC 06), Edinburgh, Scotland, 26-30 Jun 2006: SLAC-PUB-12023.

[18] S. Kurokawa, E. Kikutani: Nuclear Instruments and Methods in Physics Research **A499** (2000) and other papers in that volume.

[19] B. Aubert et al.: *The BABAR detector*: Nuclear Instruments and Methods in Physics Research **A479** (2002) 1-116.

[20] A. Abashian et al.: *The Belle detector*: Nuclear Instruments and Methods in Physics Research **A479** (2002) 117-232.

[21] O. Schneider: *Overview of the LHCb experiment*: Nuclear Instruments and Methods in Physics Research **A446** (2000) 213-221.

[22] Particle Data Group: *Review of Particle Physics*: Physics Letters **B 592** (2004) 1-1109.

[23] L.D. Landau: J. Exp. Phys. (USSR) **8** (1944) 201.

[24] A. Khanov: *The CMS tracker performance*: Nuclear Instruments and Methods in Physics Research **A446** (2000) 338-345.

[25] G. Charpak: *Electronic imaging of ionizing radiation with limited avalanches in gases*: Nobel Lecture, December 8, 1992.
Rev. Mod. Phys. **65** (1993) 591-598.

[26] F. Sauli: *GEM: A new concept for electron amplification in gas detectors*: Nuclear Instruments and Methods in Physics Research **A386** (1997) 531-534.

[27] G. Charpak et al.: *Micromegas, a multipurpose gaseous detector*: Nuclear Instruments and Methods in Physics Research **A478** (2002) 26-36.

[28] D. Decamp et al.: *ALEPH: A detector for electron-positron annihilations at LEP*: Nuclear Instruments and Methods in Physics Research **A294** (1990) 121-178.

[29] http::://garfield.web.cern.ch/garfield (version 9.00)

[30] S.F. Biagi: Nuclear Instruments and Methods in Physics Research **A421** (1999) 234-240.

http://consult.cern.ch/writeup/magboltz (version 7.0)

[31] I.B. Smirnov: Nuclear Instruments and Methods in Physics Research **A554** (2005) 474-493.

http://consult.cern.ch/writeup/heed (version 1.01)

[32] http://root.cern.ch (version 5.12.00f)

[33] D. Sampsonidis et Al.: *Study ofthe response ofthe ATLAS Monitored Drift Tubes to heavily ionizing particles and of their performance with cosmic rays*: Nuclear Instruments and Methods in Physics Research **A535** (2004) 260-264.

[34] A. Ferrari: *The KLOE drift chamber*: Nuclear Instruments and Methods in Physics Research **A494** (2002) 163-172.

[35] M.H. Kelsey: *Performance and aging of the BaBar Drift Chamber*: Nuclear Instruments and Methods in Physics Research **A535** (2004) 206-211.

[36] P. Bernardini et al.: *Precise measurements of drift velocities in helium gas mixtures*: Nuclear Instruments and Methods in Physics Research **A355** (1995) 428-433.

[37] V. Golovatyuk, F. Grancagnolo, M. Primavera: *Single-electorn longitudinal diffusion in helium-isobutane gas mixtures*: Nuclear Instruments and Methods in Physics Research **A394** (1997) 97-102.

[38] W.R. Leo: *Techniques for Nuclear and Particle Physics Experiments*: Springer-Verlag (1987)

[39] W. Blum, L. Rolandi: *Particle Detection with Drift Chambers*: Springer-Verlag (1994)

[40] D. Mazed, M. Baaliouamer : *A semi-microscopic derivation of gas gain formula for proportional counters*: Nuclear Instruments and Methods in Physics Research **A437** (1999) 381-392.

[41] G.D. Alkhazov: Nuclear Instruments and Methods in Physics Research **A89** (1970) 155.

[42] W.P. Jesse, J. Sadauskis: *Ionization by Alpha Particles in Mixtures of Gases*: Physical Review **100, number 6** (1955) 1755-1762.

[43] A. Sharma: *Properties of some gas mixtures used in tracking detectors*: SLAC-JOURNAL-ICFA-16-3.

[44] F. Sauli: *Principles of Operation of Multiwire Proportional and Drift Chambers*: CERN **77-09** (1977).

[45] W. Shockley: *Currents to Conductors Induced by a oving Point Charge*: Journal Of Applied Physics **9** (1938) 635-636.

[46] S. Ramo: *Currents induced in electron motion*: Proc. IRE 27 (1939) 584.

[47] M. Deile, J. Dubbert, N.P. Hessey: *Charge Division and Intrinsic Pulse Shaping in Drift Tubes*: ATLAS Internal Note **MUON-NO-105** (1995)

[48] http://www.fftw.org (version 3.1.2)

[49] http://www.cadence.com/products/orcad/pspice_a_d/index.aspx

[50] http://bwrc.eecs.berkeley.edu/Classes/IcBook/SPICE/

[51] G. Cataldi, F. Grancagnolo, S. Spagnolo: *Cluster counting in helium based mixture*: Nuclear Instruments and Methods in Physics Research **A386** (1997) 458-469.

[52] G. Cataldi, F. Grancagnolo, S. Spagnolo: *Cluster counting in helium based mixture*: INFN/AE-96/07 (Mar. 1996).

[53] Rong-Shyang Lu: *CDF run IIb silicon: stave design and testing*: Nuclear Science Symposium Conference Record, 2003 IEEE Vol.2 1123-1127

[54] A. Baschirotto et al.: *A CMOS high-speed front-end for cluster counting techniques in ionization detectors*: Poceeding of IWASI 2007 1-5

[55] *ILC Reference Design Report 2007*: http://www.desy.de/∼behnke/dcr/Detector/DCR.pdf

[56] J. Repond: *Calorimetry at the International Linear Collider*: Nuclear Instruments and Methods in Physics Research **A572** (2007) 211-214.

[57] N. Akchurin et al.: *Separation of scintillation and Čherenkov light in an optical calorimeter*: Nuclear Instruments and Methods in Physics Research **A550** (2005) 185-200.

[58] http://aliweb.cern.ch/Offline

[59] M. Battaglia et al.: *Physics Benchmarks for the ILC Detectors*: SLAC-PUB-11877, arXiv:hep-ex/0603010v1 March 2006.

[60] M. Ivanov et al.: *Track reconstruction in high density environment*: Nuclear Instruments and Methods in Physics Research **A566** (2006) 70-74.

[61] D. V. Schroeder: *Beamstrahlung and QED backgrounds at future linear colliders*: SLAC-R-371 October 1990.

[62] M.E. Peskin: *Pandora: an Object-Oriented Event Generator for Linear Collider Physics*: SLAC-PUB 8290 October 1999.

[63] P. Chen, K. Yokoya: *Beam-beam phenomena in Linear Colliders*: Lecture at 1990 US-CERN School on Particle Accelerators, Nov.7-14, 1990, Hilton Head Island, So. Carolina, USA.
Frontiers of Particle Beams: Springer Verlag Berlin and Heidelberg GmbH & Co. K, pp. 415-445.

[64] D. Schulte: *Beam-Beam Simulations with GUINEA-PIG*: Proceedings of International Computational Accelerator Physics Conference (ICAP 98), Monterey, California, 14-18 Sep 1998, eConf C980914,
http://flc-mdi.lal.in2p3.fr/spip.php?article60

[65] F. Richard, P. Bambade: *Strategy to measure the Higgs mass, width and invisible decays at ILC*: arXiv:hep-ph/0703173v1 January 2007